Bridge Deck Non-Destructive Evaluation Testing- Advanced Technology for Bridge Asset Management

FINAL REPORT
June 11, 2024

By: Farhad Kooban
Aleksandra Radlińska
Andrea P. Argüelles

The Pennsylvania State University
The Thomas D. Larson Pennsylvania Transportation Institute

COMMONWEALTH OF PENNSYLVANIA
DEPARTMENT OF TRANSPORTATION

CONTRACT #512101
WORK ORDER #003

[This page intentionally left blank]

Technical Report Documentation Page

1. Report No.	2. Government Accession No.	3. Recipient's Catalog No.
FHWA-PA-2024-006-PSU WO 003		

4. Title and Subtitle	5. Report Date
D11-0 Bridge Deck Non-Destructive Evaluation Testing - Advanced Technology for Bridge Asset Management	June 2024
	6. Performing Organization Code

7. Author(s)	8. Performing Organization Report No.
Kooban, F., Radlińska, A., Argüelles, A. P.	

9. Performing Organization Name and Address	10. Work Unit No. (TRAIS)
The Pennsylvania State University The Thomas D. Larson Pennsylvania Transportation Institute	11. Contract or Grant No. 512101

12. Sponsoring Agency Name and Address	13. Type of Report and Period Covered
The Pennsylvania Department of Transportation Bureau of Planning and Research Commonwealth Keystone Building 400 North Street, 6th Floor Harrisburg, PA 17120-0064	Final Report (7/22/22 – 6/30/24)
	14. Sponsoring Agency Code

15. Supplementary Notes

PennDOT Technical Advisor: Shane Szalankiewicz, P.E.
sszalankie@pa.gov

16. Abstract

This report presents the findings from the comprehensive study on Bridge Deck Non-Destructive Evaluation (NDE) Testing conducted by The Pennsylvania State University under the sponsorship of the Pennsylvania Department of Transportation (PennDOT). The study focuses on the application of advanced non-destructive technologies to assess the condition of concrete bridge decks without causing damage to the infrastructure. Key technologies employed include ground-penetrating radar (GPR), infrared thermography (IRT), and digital imaging techniques. The objective of the research was to evaluate the effectiveness of these technologies in detecting common defects such as delamination, rebar corrosion, and surface deterioration. The study provides insights into the capabilities and limitations of each method, offering a comparative analysis that assists in understanding their practical applications in bridge asset management. The findings aim to support PennDOT in enhancing their maintenance strategies by integrating these advanced NDE methods, ultimately improving the longevity and safety of bridge structures across the state.

17. Key Words	18. Distribution Statement
non-destructive evaluation; bridge decks; delamination; ground-penetrating radar; infrared thermography; surface imaging; delamination; void	No restrictions. This document is available from the National Technical Information Service, Springfield, VA 22161

19. Security Classif. (of this report)	20. Security Classif. (of this page)	21. No. of Pages	22. Price
Unclassified	Unclassified	140	$301,109.94

Disclaimer

The contents of this report reflect the views of the authors, who are responsible for the facts and the accuracy of the data presented herein. The contents do not necessarily reflect the official views or policies of the US Department of Transportation, Federal Highway Administration, or the Commonwealth of Pennsylvania at the time of publication. This report does not constitute a standard, specification, or regulation.

Credit

This work was sponsored by the Pennsylvania Department of Transportation.

Executive Summary

The Bridge Deck Non-Destructive Evaluation Testing project, conducted under contract with the Pennsylvania Department of Transportation, presents a comprehensive analysis and summary of the findings regarding the condition of bridge decks. This research project aimed to categorize existing defects based on the extent of deterioration to help strategize maintenance efforts effectively. Key methods such as ground-penetrating radar (GPR), infrared thermography (RIT), and surface digital imaging (DI) techniques were utilized to assess the conditions thoroughly. This report presents four case studies on evaluating bridge decks using various non-destructive test methods.

The research, facilitated by The Pennsylvania State University and the Thomas D. Larson Pennsylvania Transportation Institute, highlights significant advancements in non-destructive evaluation technologies that enhance bridge asset management. These technologies allow for deeper insights into common issues such as delamination, rebar corrosion, and other structural weaknesses without requiring invasive procedures.

This research project, started in July 2022, it aims to provide a comprehensive assessment of existing NDT technologies for evaluating bridge deck conditions, enabling data-driven decisions by the district for bridge asset management. The project was completed in 7 tasks, including literature and existing technology review, demonstration scans, field data analysis, laboratory tests, comparison of laboratory and field data and model development, draft final report, and final report. Report Task 1, "Literature and Existing Technology Review," was submitted in October 2022. The report included a review of common defects in bridge decks, existing technologies, and a summary of previous studies. Report Task 2, "Demonstration Scans," was submitted in June 2023. It provided information on four bridges identified by PennDOT and the technologies employed, showcasing the scans conducted by two subcontractors: Infratek Solutions Inc. and NEXCO-West USA. Report Task 3, "Field Data Analysis," was submitted in October 2023. It delved into interpreting the empirical observations of four bridges selected by PennDOT. Report Task 4, "Laboratory Tests," was submitted in December 2023. It aimed to deepen the understanding of the field data collected during inspections. Task 5 was a "Comparison of Laboratory and Field Data and Model Development" report. It delved into the nuanced analysis of laboratory and field data, juxtaposing these findings to find the gap between different techniques. Obtained results from field studies of subcontractors and PennDOT's (deck-sounding results) were compared with the findings from the Penn State research laboratory study. In

the model development part, the Penn State team created a model using machine learning and computer vision to automate the detection, classification, and quantification of defects in bridge decks through advanced NDT methods, significantly enhancing inspection efficiency and accuracy by employing the Trainable Weka Segmentation tool in an open-source platform for image segmentation and analysis. Report Task 6, "Draft Final Report," categorized existing defects based on the extent of deterioration for maintenance strategy purposes. It provided a summary of all findings for PennDOT to review.

This document, as Report Task 7, "Final Report," is provided based on the approved final revisions to the draft final report, which includes:

Chapter 1, "Research Significance," elaborates on the critical significance of the research for bridge asset management. It explains how NDE technologies can revolutionize bridge evaluations by enabling early detection of defects like delamination and rebar corrosion. The chapter emphasizes the empirical data and comparative analyses provided by the study, which aid in optimizing maintenance strategies and influencing local and national standards in bridge deck evaluation. The practical implementation of this research is expected to result in cost savings, reduced bridge failures, and enhanced public safety.

Chapter 2 (Task 1), "Existing Technology and Literature Review," is a comprehensive review that includes two sections. "Common Defects in Bridge Decks" details the various forms of deterioration that affect bridge decks, including concrete deterioration, rebar corrosion, delamination, spalling, cracking, scaling, and voids. Each defect type is explained in terms of its causes, impact on structural integrity, and detection challenges. "Existing NDT Technologies" reviews the state-of-the-art NDE technologies used in bridge deck evaluations. It covers digital imaging, electromagnetic testing (including GPR), thermal methods (IRT), electrochemical methods, and acoustic methods. Each technology is analyzed for its principles, capabilities, and limitations in detecting various types of bridge deck defects.

Chapters 3 and 4 (Task 2) are about "Benchmark Bridges" and "Demonstration of Field Non-Destructive Testing." Chapter 3 provides detailed information about the four bridges in Pennsylvania selected for field tests. It includes descriptions of their structures, locations, and existing conditions. The chapter sets the context for the application of NDE methods on these benchmark bridges, providing a basis for evaluating the effectiveness of the technologies in real-world scenarios. Chapter 4 documents the field-testing procedures and results for the four benchmark bridges. It includes

detailed analyses of the data collected using digital imaging, GPR, IRT, and acoustic methods. The results highlight the capabilities and limitations of each NDE technology in assessing the bridge deck conditions. The chapter provides empirical evidence supporting the practical applications of these technologies in bridge asset management.

Chapter 5 (Task 3), "Field Data Analysis," focuses on the analysis of the field data collected from the four benchmark bridges. It presents surface image analysis, infrared thermography image analysis, and GPR data analysis. The findings are compared to evaluate the accuracy and reliability of each NDE method. The chapter provides insights into the strengths and weaknesses of the technologies in detecting different types of defects.

Chapter 6 (Tasks 4 and 5), "Comparison of Laboratory and Field Data," compares the results obtained from laboratory tests with the field data. It discusses the effectiveness of IRT and GPR in both controlled and real-world environments. The chapter highlights the discrepancies and correlations between the laboratory and field results, providing a comprehensive understanding of the performance of NDE technologies under different conditions.

Chapter 7 (Task 5), "Model Development," describes the development of a model using machine learning and computer vision to automate the detection, classification, and quantification of defects in bridge decks. The model aims to enhance inspection efficiency and accuracy by integrating advanced NDE methods. The chapter details the technical aspects of the model development and its potential applications in bridge asset management.

Chapter 8, "Conclusion," summarizes the findings of the study, emphasizing the importance of integrating advanced NDE methods into bridge maintenance strategies. It highlights the benefits of using technologies like GPR, IRT, and digital imaging for early defect detection and preventive maintenance. The chapter concludes with recommendations for future research and the potential for further advancements in NDE technologies.

Keywords: non-destructive evaluation; bridge decks; delamination; ground-penetrating radar; infrared thermography; surface imaging; delamination; void

TABLE OF CONTENTS

LIST OF FIGURES

LIST OF TABALS

1 Research Significance

The research conducted in this project is critically significant for bridge asset management, particularly in the evaluation and maintenance of bridge decks. Aging infrastructure and frequent exposure to harsh environmental conditions make bridge decks susceptible to various forms of deterioration, compromising their structural integrity and safety. Traditional methods of bridge inspection are often invasive, time-consuming, and sometimes fail to detect subsurface anomalies until they become visible, which can be too late for simple interventions. The introduction and validation of advanced non-destructive evaluation (NDE) techniques such as ground-penetrating radar, infrared thermography, and digital imaging offer a paradigm shift in bridge evaluations. These technologies enable the early detection of potential issues such as delamination, rebar corrosion, and other structural weaknesses, allowing for timely preventative measures. This extends the lifespan of bridge structures and ensures safety.

Moreover, this research contributes significantly to the body of knowledge by providing empirical data and comparative analyses of various NDE techniques (including digital imaging, electromagnetic, thermal, and acoustic methods), aiding in the optimization of maintenance strategies. The findings from this project have the potential to influence local maintenance practices and set benchmarks for national and global standards in bridge deck evaluation. The practical implementation of this research is expected to result in significant cost savings, reduced bridge failures, and enhanced public safety, thus having a broad and impactful significance in the field of civil engineering.

2 Existing Technology and Literature Review

2.1 Common Defects in Bridge Decks

Bridge decks experience a loss of integrity over time due to factors such as poor initial quality, damage from deicing salts, overloading, high temperatures, freeze-thaw cycle-induced stresses, fatigue, carbonation, alkali-silica reaction, and rebar corrosion. The deterioration of concrete decks can result from the corrosion of steel or degradation of concrete, significantly reducing their load-carrying capacity. Among the various deterioration phenomena, the following mechanisms are of the highest concern to inspectors [1], [2]:

- Concrete deterioration
- Rebar Corrosion
- Delamination
- Concrete Spalling
- Vertical Cracking
- Subsidence Cracking
- Scaling
- Pop-out
- Honeycomb and Voids

2.1.1 Concrete Deterioration

Concrete bridge deck deterioration can be caused by cracking, scaling, spalling, delamination, alkali-aggregate reaction, sulfate attack, corrosion, and freezing and thawing. Additionally, harsh weather conditions and traffic can contribute to the degradation of bridges. Figure 1 shows a bridge deck with severe deterioration. This damage can eventually lead to irreparable degeneration of the deck as well as damage to the girders and substructure [1], [3].

Figure 1 Significant Deterioration in a Concrete Bridge Deck [3]

2.1.2 Rebar Corrosion

Reinforcing steel embedded in concrete is generally protected against corrosion by an adequately thick concrete cover, a passive layer formed in alkaline cement-based materials (pH ≈ 13.3). High alkalinity can cause a protective film formation on the rebar's surface. This passive layer can be destroyed in the presence of chlorides or due to the decrease of the pH value caused by the carbonation of the concrete. After the breakdown of the passive layer, oxide film will be destroyed then corrosion at the reinforcement can begin, which can cause severe deterioration of the steel and the concrete [4].

The extent of corrosion depends on several factors, including the composition of the metal, humidity, temperature, water pH, and exposure to pollution and salts. Chloride diffusion, mainly due to the application of roadway deicing salts, is a significant cause of corrosion. Corrosion of steel rebars in a bridge deck can directly reduce the deck's structural capacity. Additionally, the corrosion process can cause internal stresses, cracking, delamination, and ultimately spalling of the concrete at or slightly above the level of the rebars.

In the initial phase of corrosion, no visible damage can be detected on the concrete surface (Figure 2). Only later, when cracks develop or spalling of the concrete coatings occurs, can the damage be assessed through visual inspection. Consequently, repair actions at this stage are likely to be more costly and time-consuming than if addressed early on. Repair costs increase exponentially as the extent of damage increases [1], [5].

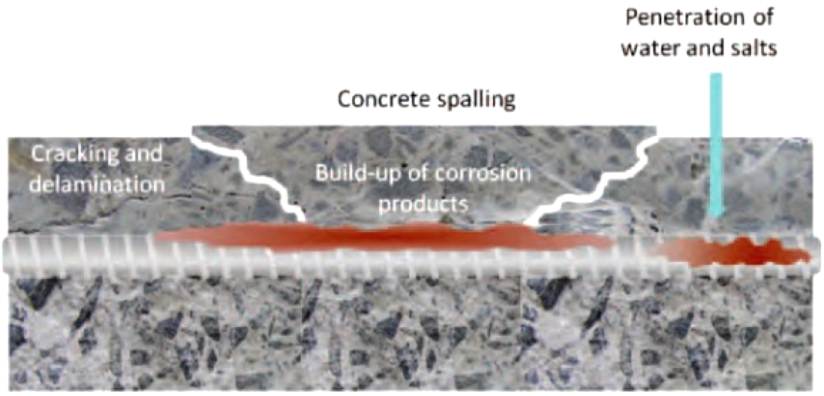

Figure 2 Corrosion Process [1]

2.1.3 Deck Delamination

Horizontal cracking due to the expansion of corroded rebars is known as delamination, a serious deterioration issue in concrete bridge decks. This expansion can create subsurface cracks within the concrete, which may be confined to a small area or extend over a larger region. Delamination is typically not visible on the concrete surface. If timely repairs are not undertaken, corrosion will persist, causing the delamination to progress into open spalls, ultimately compromising the structural integrity of the deck.

Figure 3 A slab with Naturally Occurring Delamination [6], [7], [8]

Figure 3 depicts concrete slabs with naturally occurring delamination, showing different views of the damage. The top left image displays exposed reinforcing steel bars (rebar) due to delamination

and cracks. The top right image provides a close-up of a concrete cross-section with rust stains from corroded rebar, indicating internal damage. The bottom image highlights a concrete beam with visible cracks and delamination, where delamination is evident and pointed out by an arrow.

2.1.4 Concrete Spalling

Concrete spalling refers to the deterioration of concrete through natural weathering or chemical reactions, leading to sections of cement chipping away from the main structure. This often results in fractured and weakened concrete, commonly seen on exposed concrete edges, deck joints, or construction joints. Spalling involves the detachment of concrete fragments from the surface, either violently or non-violently, resembling pitted acne scarring and breaking off in flecks that can expose rebar. Several factors can cause spalling, including poor-quality concrete, improper curing or finishing techniques, bond failure in two-course construction, electrochemical reactions (such as those caused by de-icing salts), corrosion or oxidation of reinforcing rebar due to water exposure, and the wear and tear from the freeze-thaw cycle [9], [10], [11].

2.1.5 Vertical Cracking

Vertical cracks in bridge decks can result from various factors, including rebar corrosion, plastic shrinkage, heat of hydration, ambient temperature, geometric constraints during concrete curing, traffic load, and cycles of freezing and thawing. These cracks can grow wider as the metal bars continue to rust (Figure 4).

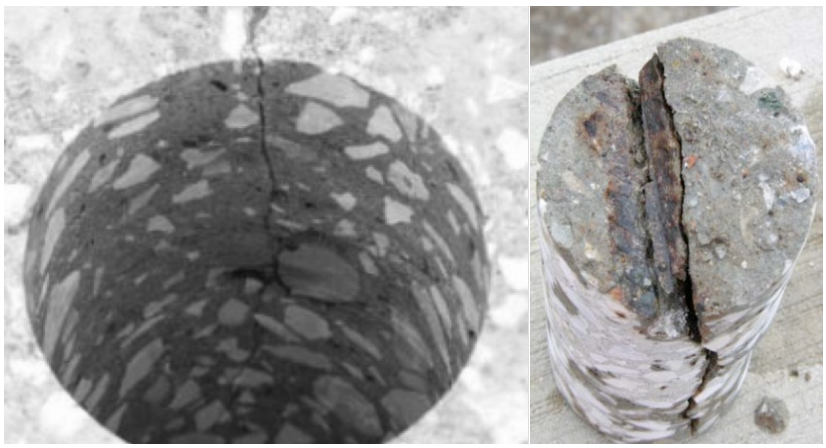

Figure 4 Vertical Cracking [6]

2.1.6 Subsidence Cracking

Exposure to salt, whether from de-icing salts on roads or seawater, can accelerate the decline of

concrete bridge decks. This happens because salt allows chlorides to seep into the concrete and corrode the steel bars used for reinforcement (rebar). This corrosion causes the steel to expand, which in turn cracks the surrounding concrete. This type of cracking, called subsidence cracking, weakens the bridge deck and can lead to premature deterioration [12]. Figure 5 shows subsidence cracking at the location of reinforcing steel and a large aggregate.

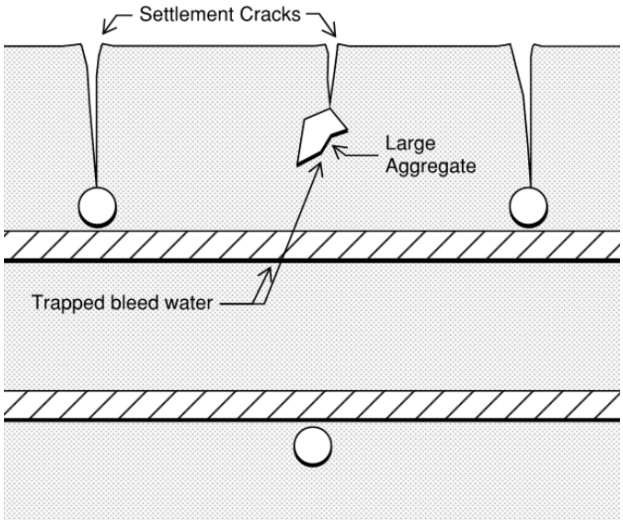

Figure 5 Subsidence Cracking [13]

2.1.7 Scaling

Concrete can develop unsightly patches of flaking called scaling. This can be caused by several factors, such as excess water rising to the surface during setting (bleeding), the concrete shrinking too quickly as it hardens (plastic shrinkage), repeated freezing and thawing cycles, air bubbles trapped near the surface due to poor placement, a lack of tiny air bubbles intentionally added for freeze protection (air entrainment), or damage from salt, such as deicing salts or seawater [11].

2.1.8 Pop-Out

Pop-out is a small crater that appears on the concrete surface when a near-surface piece of aggregate breaks away. This can happen because certain types of aggregate can swell or expand due to internal pressure. This pressure can be caused by the aggregate itself reacting with the concrete (reactive aggregate), water freezing inside very absorbent aggregate particles (frost action), or the way the aggregate particles are naturally weak along certain planes (cleavage planes). [11]

2.1.9 Honeycomb and Voids

Honeycomb and voids are essentially air pockets that form in concrete when the cement paste does not fill the entire mold (formwork) or the spaces between the coarse aggregates in the mixture. Concrete with heavy reinforcement, large cavities, or deep placements are more prone to this. These defects can be caused by poor handling of the concrete at any stage, from mixing to placement, or by an improper mixture design itself. In short, anything from using too little cement to improper vibration of the concrete can lead to honeycomb and voids, and unlike some other surface issues, these voids almost always require repair as they weaken the concrete structure.

2.2 Existing NDT Technologies

Existing technologies for diagnosing defects in reinforced concrete are generally categorized into destructive, semi-destructive, and non-destructive testing (NDT) methods. Destructive and semi-destructive methods are used to test samples and structural members and can also be applied to entire structures. Destructive methods primarily test strength and monitor its changes over time, typically by testing samples taken from the structure or entire components such as bridge decks. Load tests, though rarely used on buildings, are more frequently applied to bridges and roads and fall into this category. The difference between semi-destructive and non-destructive (NDT) methods is that in the case of the former, the material is usually locally and superficially damaged when tested. No such damage occurs in the case of non-destructive methods. This is one of the reasons why they are suitable for testing large surfaces down to a considerable depth, and in general construction. Moreover, in the case of NDT methods, measurements can be repeated, whereby the test results can be verified and validated [14]. This report focuses on existing NDT technologies. A classification of the common NDT methods for bridge decks as shown in Figure 6 [2].

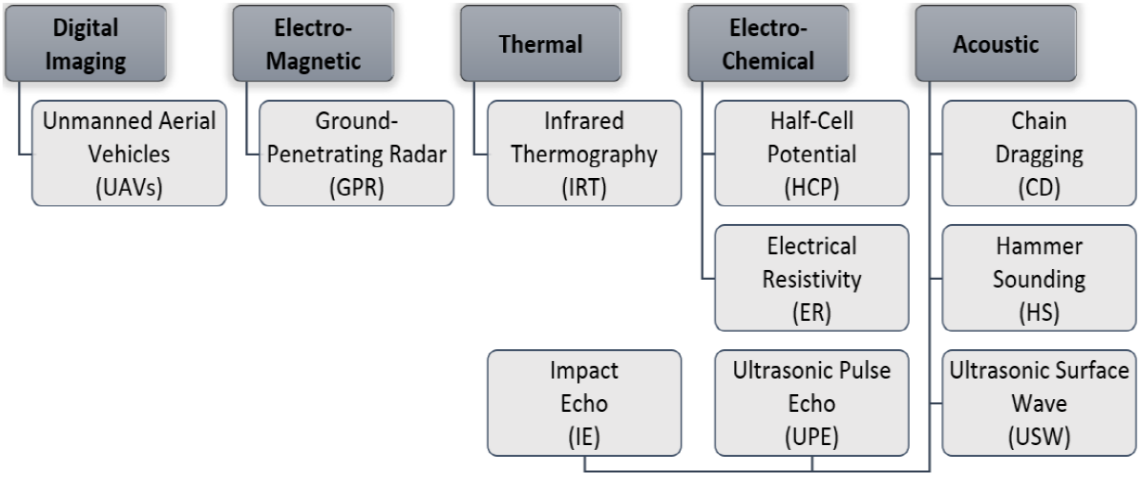

Figure 6 Common NDE Methods for Bridge Decks [2]

Each NDT method has unique capabilities and limitations [15]. For example, Visual Inspection (VI) can be considered a quick and inexpensive method of investigation. The application and capabilities of VI are identifying surface defects (e.g., spalling and cracking). It is simple but it has many limitations such as being subjective, tedious, and biased. It cannot detect interior flaws and is hazardous to personnel [2].

2.2.1 Digital Imaging (DI)

Digital Imaging (DI) refers to the process of capturing, processing, and analyzing images using digital technology. In the context of infrastructure inspection, DI involves using digital cameras, sensors, and computer algorithms to acquire detailed visual information about the condition of various structures. These digital images can be enhanced, processed, and analyzed using software to detect, measure, and document defects and anomalies. DI provides high-resolution images that allow for precise assessment and monitoring of infrastructure elements, enabling engineers to make informed decisions about maintenance and repairs.

The application of DI in infrastructure inspection is widespread and includes the use of CCTV robots and Unmanned Aerial Vehicles (UAVs) to capture images of hard-to-reach areas such as bridges, tunnels, and high-rise buildings. These images can be analyzed to identify surface defects like cracks, spalling, and corrosion. Additionally, DI techniques can be integrated with other technologies, such as 3D modeling and computer vision algorithms, to automate the detection and measurement of defects, track changes over time, and create detailed visual records for asset management systems. This approach enhances the efficiency, accuracy, and safety of infrastructure inspections, reducing the need for manual labor and minimizing disruptions to service [2].

The limitations of this method are subjective, tedious, and biased, and it cannot detect interior flaws. For civil infrastructure inspection, various vision-based tasks have been investigated, including automated detection and dimension measurement of concrete cracks, spalling as well as other surface defects, recognition of damage pattern changes and 3D visualization of cracks.

Applications and capabilities of DI, the following can be mentioned:

- DI provides detailed images for identifying surface defects, enhancing the accuracy of inspections.
- It serves as an effective alternative to traditional visual inspections, offering a more reliable and consistent method.
- DI allows for rapid inspection processes, significantly reducing the time required for assessments.
- The technique causes less disruption to services, making it ideal for busy infrastructures.
- DI is automated and less subjective, reducing human error and providing more consistent results.
- DI can be easily incorporated into a Bridge Management System (BMS), streamlining the management and maintenance of infrastructure.

As limitations of DI, the following can be mentioned:

- DI is unable to detect subsurface defects, limiting its effectiveness for comprehensive assessments.
- Image quality can be affected by ambient environmental conditions such as lighting and weather.
- Effective use of DI requires advanced edge detection algorithms to accurately identify and analyze defects.
- Noisy images can complicate image processing, making it more challenging to obtain accurate results [2].

2.2.2 Electromagnetic Testing (ET)

In recent years using electromagnetic testing (ET) has yielded good results for the inspection of concrete structures [16]. Electromagnetic methods are based on the propagation of electromagnetic waves in dielectric materials (i.e., concrete); the wave propagation depends on the dielectric

permittivity of concrete, which can be influenced by various parameters, such as water presence, chloride content, rebar configuration, and pore structure. A radar system usually consists of a control unit, a radar antenna, and a display unit. The control unit generates a radar pulse (in the microwave spectrum) and sends it over a cable to the antenna. The antenna transmits pulses to the surface. When this energy encounters the interface between two materials with different dielectric properties, such as rebar, air, moisture, or a base layer material, some of the energy is reflected in the radar antenna. The received pulse is returned to the control block for processing or storage. The display unit (video or chart recorder) displays the data. The reflected energy is received by the transducer, amplified and recorded. The electromagnetic pulse repeats rapidly, and the resulting radar data stream creates a continuous record of the surface. The radar system generates a linear profile of the materials under the antenna's path.

One of the most widely used electromagnetic techniques is ground penetrating radar (GPR), a recognized non-destructive evaluation technique with many applications. Figure 7 shows GPR image of a concrete bridge deck [17]. GPR provides an electromagnetic wave-reflection survey to assess in-depth characteristics of subsurface layers, including damages, voids, cracks, and corrosion, as well as steel rebar location [18] [19].

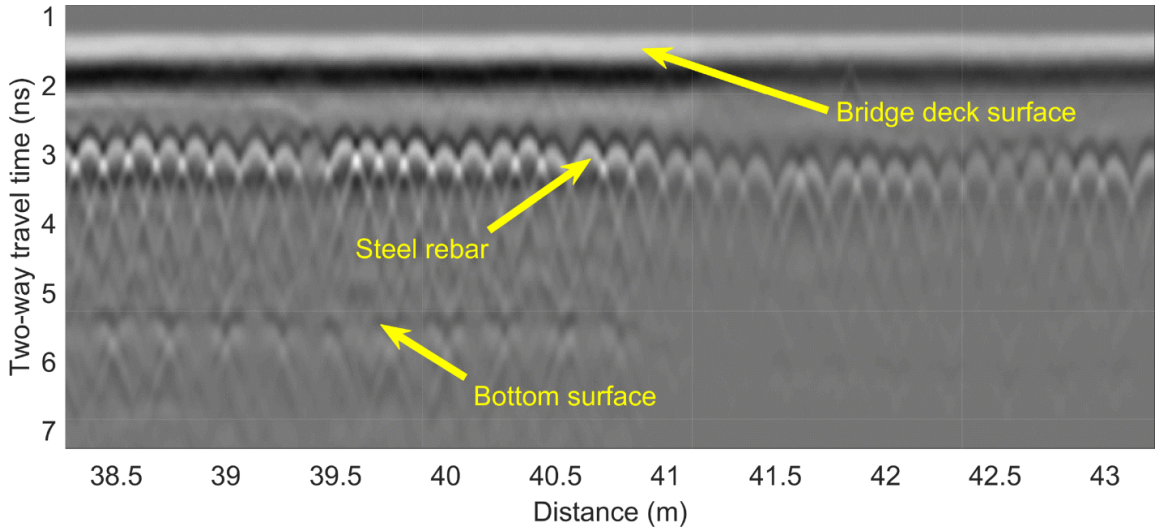

Figure 7 GPR Image of a Concrete Bridge Deck [20]

GPR has been commercially available in the United States and Canada since the early 1970s as one of the most successful NDE methods for evaluating concrete bridge decks [21], [22]. Most commonly used on concrete bridge decks with overlay finishes. This allows inspection of concrete deck surfaces that are obscured by the finish course. If the concrete deck is uncovered, GPR is not as

accurate or as fast as infrared thermography. Ground Penetrating Radar (GPR) identifies areas of a concrete deck with different dielectric properties or conductivity. Regardless of its function, the process of analyzing and interpreting data requires a great deal of effort. For example, some concretes, such as dry concrete with low permeability, affect the accuracy of her GPR in detecting areas of delamination. GPR is also sensitive to the presence of water and chlorides on the deck and between the overlays and base concrete, and the presence of debris on the deck surface. These conditions can greatly affect the accuracy of your data. Heavy or crowded rebar placement also affects the detection of Under Rebar Detection. GPR should also scan perpendicular to the top layer of the steel rebars. Therefore, some structural inspections require the survey to be conducted perpendicular to the flow of traffic. This would require traffic to be limited or stopped entirely while an investigation is taking place. In many cases, multiple passes must be made in the deck area, and the cost can be prohibitive [17]. Furthermore, the GPR method cannot estimate mechanical properties of concrete such as strength and modulus, nor can it quantitatively assess corrosion damage (such as corrosion rate and loss of rebar sections) [23], [24], [25].

There are three antenna array types which are shown in Figure 8. Type 1 has outstanding resolution at shallow depths, securely records 3D data, and is used at high speeds for road, pavement, and railway inspection. Type 2 features high-resolution, near-surface 3D imaging with deep penetration for shallow and deep underground mapping and object detection, deck assessment, and utility mapping. Type 3 is used for exceptional depth capabilities and 3D imaging in harsh environments for mapping and detecting objects deep underground [26].

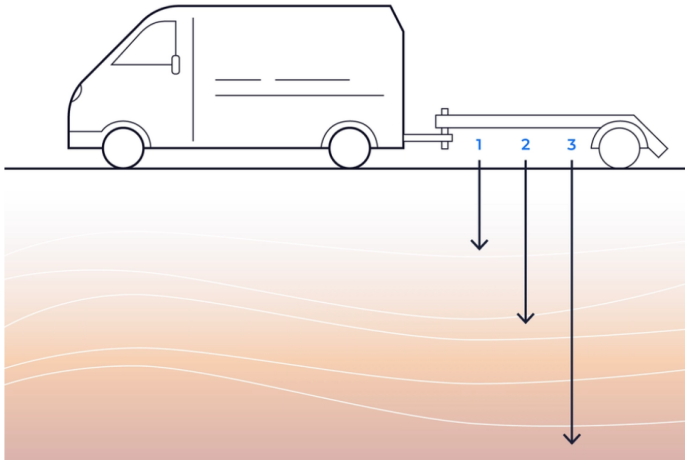

Figure 8 Three Antenna Arrays Sensor [26]

As an application and capabilities of the GPR method, the following can be mentioned:

- Ground Penetrating Radar (GPR) can identify delaminations, voids, cracks, rebar configurations, and member thickness, making it a versatile tool for structural assessment.
- GPR is the most common method for evaluating the in-depth characteristics of subsurface layers and generating contour maps of subsurface features in bridge decks.
- It reliably detects defects in various scenarios, including those without overlays and those with bonded asphalt overlays.
- Unlike some other methods, GPR's accuracy is not affected by ambient temperatures.
- GPR can quickly survey large areas with 100% coverage, making it highly efficient for extensive inspections.
- The method requires minimal lane closures, reducing traffic disruption during inspections.
- GPR allows for real-time data processing, facilitating immediate analysis and decision-making.

As limitations of GPR, the following can be mentioned:

- GPR cannot provide data on corrosion rates or rebar section loss, limiting its usefulness for certain types of assessments.
- Extremely cold weather and the presence of deicing salt can negatively impact GPR accuracy.
- Variations in pavement thickness, cover thickness, rebar spacing, and moisture content can affect the results, as moisture tends to absorb radar waves.
- Interpreting GPR data requires expert judgment to evaluate thresholds and differentiate between different conditions of concrete.
- GPR is less effective at detecting delaminations when there is no moisture present, which can limit its applicability in certain conditions. [2].

2.2.3 Thermal Method

Infrared Thermography (IRT) is an alternative technology to acoustic chain drag testing to detect thermal radiation emitted in concrete, such as coating separation and surface delamination. Infrared (IR) cameras create images of surface temperatures based on the emitted radiation and detect temperature changes by measuring the thermal radiation emitted. There are two test methods for the infrared temperature measurement method based on the heat source, active method, and passive method. The active method uses an external thermal stimulus to create the required heat flux

conditions on the concrete under test. The passive method uses natural heat sources (Figure 9) such as solar heating and ambient temperature variations.

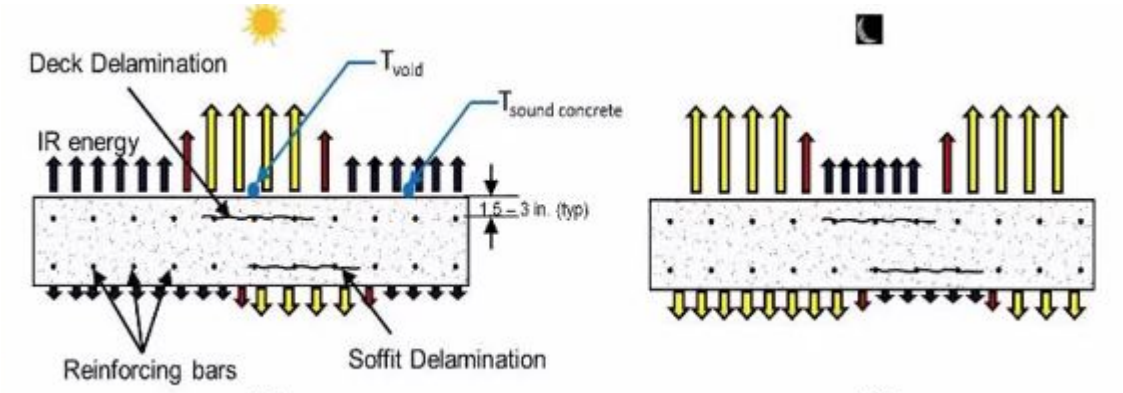

Figure 9 Passive Method Uses Natural Heat Sources [8]

The principle behind using Infrared Thermography (IRT) for evaluating concrete bridges is based on the fact that subsurface defects, like delamination, interfere with the normal heat transfer through the concrete. During the day, as the sun and ambient heat raise the temperature of the concrete, the areas above these subsurface defects heat up more quickly compared to areas where the concrete remains intact. This results in the delaminated areas appearing as hot spots on the concrete surface when viewed through an infrared camera. Conversely, during the night when the ambient temperature drops, the concrete begins to cool down (Figure 10). The surface areas above the delaminations cool down more rapidly than the intact concrete, making these areas appear as cold spots relative to the undamaged concrete. This thermal behavior allows for the identification of subsurface defects by observing the temperature variations on the surface of the concrete structure. By capturing these thermal images at different times of the day, engineers can accurately pinpoint the locations of delaminations and other defects, facilitating timely maintenance and repairs to ensure the structural integrity of the bridge [27], [2].

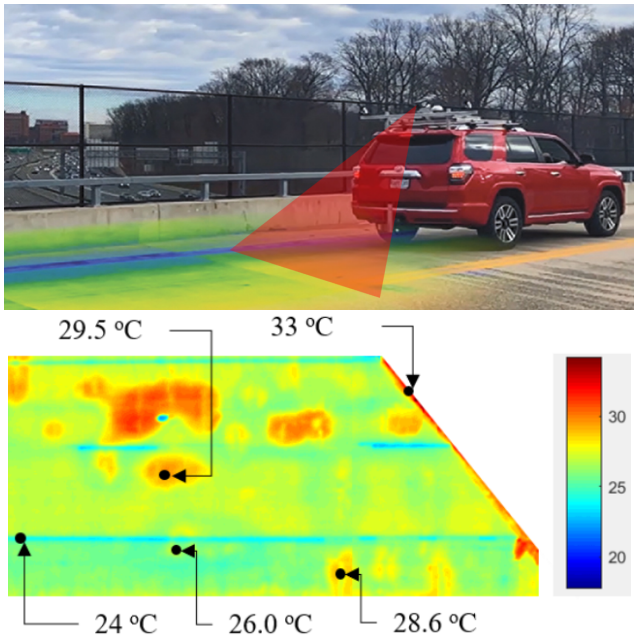

Figure 10 Infrared Thermographic Inspection of Bridge Decks [28]**,** [29]

As an application and capabilities of the IRT method, the following can be mentioned:

- IRT can identify cracks, delaminations, voids, thermal conductivity anomalies, and overlay debonding.
- It allows for the inspection of large surface areas in a short period, making it highly efficient.
- The method is safe, cost-effective, non-invasive, and non-contact, reducing risks and costs associated with traditional inspection methods.
- IRT provides real-time visualization of thermal anomalies, enabling immediate analysis and decision-making.
- The method causes minimal traffic disruption, making it suitable for use on busy infrastructure without significant impact on daily operations.

As limitations of IRT, the following can be mentioned:

- IRT captures images of the surface, thus it cannot provide information about the depth of defects.
- The accuracy of IRT can be affected by environmental conditions such as wind speed, solar radiation, moisture content, and surface emissivity.
- IRT cannot effectively detect delaminations if they are filled with water instead of air, limiting its ability to identify certain types of defects [2].

2.2.4 Electro-Chemical

There are two primary methods for electro-chemical evaluation in concrete structures: Electro-Resistivity (ER) and Half-Cell Potential (HCP) evaluation. Electro-Resistivity (ER) techniques, as illustrated in Figure 11, are utilized to detect moisture content and structural defects such as cracks. The moisture level in concrete is a critical indicator of its corrosion state, as electrical conduction within concrete predominantly occurs through electrolytic current flow via the open pore system. In regions where the concrete is damaged or cracked, increased porosity creates preferred pathways for fluid and ion movement, exacerbating corrosion processes. Thus, areas with higher electrical resistivity indicate lower corrosion currents passing between the anodic and cathodic zones of the reinforcing steel, suggesting better structural integrity and less corrosion activity [2].

Figure 11 Resistivity Test [6]

As an application and capabilities of the ER method, the following can be mentioned:

- The ER method is effective for determining the moisture content within concrete structures, which is critical for assessing the potential for corrosion and other forms of degradation.
- ER can evaluate the homogeneity of concrete and the corrosion rate of embedded rebars, providing valuable information for the maintenance and repair of infrastructure.
- It is capable of identifying regions that are susceptible to chloride penetration, which is a significant factor in the deterioration of reinforced concrete.

As limitations of ER, the following can be mentioned:

- The accuracy of the ER method is highly affected by the condition of the top surface. If the surface is too dry or too wet, it can significantly impact the results.
- Measurements taken using the ER method require corrections for temperature variations to ensure accurate results, adding complexity to the data interpretation process.

- The ER method provides raw data, which often requires extensive processing and interpretation by experienced professionals to derive meaningful conclusions.

Half-Cell Potential Evaluation (HCP) is also a widely adopted method for assessing active corrosion in reinforced concrete structures. As illustrated in Figure 12, HCP measurements can be performed at temperatures above 2°C. It is crucial that these measurements be taken on free concrete surfaces without overlays, such as asphalt, to prevent inaccurate or unfeasible results. The fundamental principle of HCP is that when a metal is immersed in an electrolyte, positive ions dissolve, leaving an excess of negative charges due to oxidation. These positive metal ions gather at the metal-liquid interface, attracting anions from the electrolyte solution, thereby forming a half-cell.

If two different metals are submerged in an electrolyte and connected electrically by a wire, a galvanic element is created. In this setup, the potential difference between the two metals can be measured. More negative HCP values indicate higher levels of corrosion activity. This method is effective in identifying areas of active corrosion, allowing for timely maintenance and repairs to reinforce the structural integrity of concrete infrastructures [2]. The standard test methods for corrosion potentials of uncoated reinforcing steel in concrete are mentioned in ASTM C 876-15 [30].

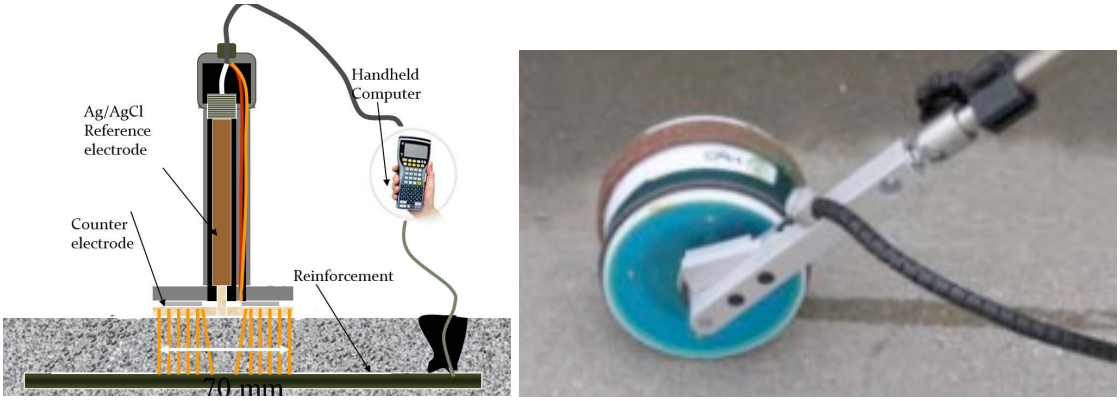

Figure 12 Half-Cell [31], [6]

As an application and capabilities of the HCP method, the following can be mentioned:

- The Half-Cell Potential (HCP) method is effective for assessing the corrosion activity of steel reinforcement within concrete structures.
- It can be applied to concrete structures regardless of the thickness of the concrete cover, as well as the size and detailing of the reinforcement.
- The HCP method can be utilized at any time and under any climatic condition, making it highly adaptable.

- The method is straightforward to execute and involves portable equipment, facilitating on-site evaluations.

As limitations of HCP the following can be mentioned:

- HCP cannot provide data on the rate of corrosion, limiting its ability to offer a comprehensive assessment of the deterioration process.
- A correction factor must be applied if the test is conducted outside the temperature range of 17-28°C to ensure accuracy.
- The results are affected by the resistivity of the concrete and the thickness of the concrete cover, which can impact the interpretation of data.
- HCP cannot be used if there are overlays or coated rebars present, as these conditions can obstruct accurate measurements [2].

2.2.5 Acoustic

Acoustic technics are classified into 5 methods, Chain Dragging (CD), Hummer Sounding (HS), Ultrasonic Surface Wave (USW), Ultrasonic Pulse Echo (UPE), and Impact Echo.

2.2.5.1 Chain Dragging (CD) and Hummer Sounding (HS)

Two major factors in concrete bridge damage are delamination and spalling. In these methods, which are the most frequent inspection procedures utilized by transportation agencies and other bridge owners for detecting delamination in concrete bridge decks, the inspector sets up the deck surfaces to grids, i.e., 5 ft by 5 ft. Then drags several lengths of heavy chain over the concrete surface of the entire bridge deck or hits it with a hammer. The sound changes from a clear ringing sound (sound deck) to a somewhat muted or hollow sound (delaminated deck), allowing for mapping the deck condition. Whenever a dull or hollow sound is heard, the area is outlined as damaged by marking this section with paint. These areas are marked and mapped for further evaluation (Figure 13). At the end of the test, the marked areas can be transferred to electronic format [32], [17].

Figure 13 Chain Dragging and Hammer Sounding Technique [6]

Even though this type of inspection involves shutting down the lane under survey, inspectors are frequently required to work alongside open traffic lanes. The traffic noise makes it difficult to distinguish sounds the chain makes as it crosses delaminated concrete. In addition, the chain drag method relies heavily on the knowledge and experience of the inspector, making it subjective and potentially inaccurate. Therefore, the chain drag method did not consistently provide accurate results [2].

ASTM D 4580-03, "Standard Practice for Measuring Delaminations in Concrete Bridge Decks by Sounding", covers three procedures for surveying concrete bridge decks by sounding to determine delamination in the concrete. The procedures described herein are not intended to be used on bridge decks covered with bituminous mixtures and only can be used on bridge decks covered with Portland cement concrete mix. The following three procedures are covered in this standard:

Procedure A, Electro-Mechanical Sounding Device, uses an electric powered tapping device, sonic receiver, and recorder mounted on a cart. The cart is pushed across the bridge deck and delamination is recorded on the recorder. Longitudinal lines are established at a predetermined distance on the bridge deck. After calibration, the sounding device is driven along the determined lines. Electrically powered tapping wheels emit vibrations into the deck that are sensed by sonic receivers. Areas of delamination are indicated by displacement on the strip chart recorder. All areas on a strip chart showing delamination drawn on a scaled map of the bridge deck. An outline is made showing the areas of delamination.

Procedure B, using Chain Drag method consists of dragging a chain over the bridge deck surface.

The detection of delamination is accomplished by the operator noting dull or hollow sounds. Tapping the bridge deck surface with a steel rod or hammer may be substituted for the chain drag. Procedure C, Rotary Percussion method, consists of rolling a dual-wheel, multi-toothed apparatus attached to an extension pole over the bridge deck surface. The percussive force caused by the tapping wheels will create either a dull or hollow sound indicating any delamination [33]. As an application and capabilities of the CD and HS method, the following can be mentioned:

- Provide contour maps regarding soundness of the surface and mark the delaminated areas on the surface of the deck.

As limitations of CD and HS the following can be mentioned:

- Subjective and tedious
- Unable to detect initial delamination and ineffective on bridge decks with overlay [2].

2.2.5.2 Ultrasonic Surface Waves (USW)

Ultrasonic testing (UT) is a family of non-destructive testing techniques based on the propagation of ultrasonic waves in the object or material tested. Ultrasonic transducers generate a sound wave by converting electrical energy to mechanical energy using a piezoelectric crystal which called transducer [34]. In general, there are two methods to measure the speed of sound in solids using a transducer system. One is a setup where two or more transducers act as transmitters, and others act as receivers. Sound speed measurements can be made by measuring the time between the signal generated at the transmitter and the recording at the receiver. Another type of setup is often called a pulse-echo system. A transducer is placed near the sample and acts as a transmitter and a receiver. When the generated pulse signal hits a boundary between two mediums with distinct acoustic impedances, some of the pulse is reflected back. This reflected pulse is subsequently detected by the receiver. Also, ultrasonic waves scatter at interfaces due to the acoustic impedance mismatch of the media due to various heterogeneities, e.g., cracks, voids, and inclusions [34], [35].

Additionally, the propagation of ultrasonic waves can be affected by material stresses. Stresses within the material can alter both the speed and the direction of wave propagation, thereby affecting the wave’s interaction with the material’s internal structures. The effect of stress on ultrasonic waves is important in assessing not only the material's integrity but also its mechanical properties under different load conditions [36].Three primary modes of ultrasonic wave propagation were considered: longitudinal waves (P-waves), transverse waves (S-waves), and surface waves.

Ultrasonic Surface Waves (USW) can detect defects at or near the part surface. P- or S-waves can detect defects deep to the surface if in line with the transducer [37]. USW is utilized to detect overlay debonding and delamination. This method is a part of spectral analysis of surface waves method used to evaluate material properties (e.g., elastic modulus) [2]. These surface waves are elastic waves with frequencies in the kHz–MHz range [38] that travel along the free surface of a medium and propagates with a velocity dependent on the elastic properties of the medium. The waves propagating in a heterogeneous medium are dispersive; waves of different wavelengths or frequencies travel with different velocities [2]. In other words, wave speed is directly influenced by the elastic properties of the medium through which the wave propagates, with a stiffer material resulting in faster speeds [38].

As a result, monitoring the phase velocity versus frequency relationship can provide information about the subsurface of the bridge deck and existence of anomalies. The presence of delamination is indicated by a change in wave velocity [2].

As an application and capabilities of the USW method, the following can be mentioned:

- The Ultrasonic Surface Wave (USW) method is effective in detecting delaminations within concrete structures.
- USW can evaluate the modulus and strength of materials, providing essential information about structural integrity.
- This method can measure the depth of vertical cracks in bridge decks, aiding in the assessment and maintenance of infrastructure.

As limitations of USW the following can be mentioned:

- The accuracy of USW requires excellent coupling between the transducer and the concrete surface to ensure reliable measurements.
- Performing USW assessments often necessitates lane closures, which can disrupt traffic and increase logistical complexity.
- The method requires very close grid spacing to achieve detailed and accurate results, making it labor-intensive.
- USW can be time-consuming, particularly for large areas, due to the detailed nature of the grid measurements.
- Problems with wave depletion can affect the accuracy and reliability of the results, necessitating careful interpretation by experienced personnel [2].

2.2.5.3 Ultrasonic Pulse Echo (UPE)

Ultrasonic waves are generated by exciting piezoelectric material with a high amplitude pulse that features high voltage and current. The physical principle underlying this method involves measuring the transit time of ultrasonic waves as they travel through a material and reflect back to the surface of the tested medium. Because the velocity of ultrasonic waves varies across different mediums, the transit time or velocity can be utilized to detect internal flaws. As the wave interacts with a flaw, a portion of the radiated energy is reflected back to the surface. Areas of concrete that exhibit deterioration or cracking will show lower wave velocity, indicating potential issues within the structure [2].

As an application and capabilities of the UPE method, the following can be mentioned [2], [6]:

- The Ultrasonic Pulse Echo (UPE) method can detect shallow and small delaminations, cracks, voids, honeycombs, and debonding of reinforcement bars. It is also used for measuring deck thickness.
- UPE provides reliable and comprehensive evaluation and imaging of voids, material changes, tendon ducts, and rebars.
- This method offers detailed information on the presence and depth of defects within the material.
- Data collection with UPE can be automated, increasing efficiency and consistency in large-scale inspections.

As limitations of UPE the following can be mentioned [2], [6]:

- UPE requires scanning mode data collection with small test point spacing, making the process slow and time-consuming.
- It is less reliable in detecting shallow defects, which can limit its effectiveness in certain applications.
- Several parameters, such as material properties and surface conditions, influence wave propagation, affecting the accuracy of the results.
- Ensuring proper probe coupling on rough surfaces can be challenging, potentially compromising data quality.
- Inspections often necessitate lane closures, leading to traffic disruptions.

- The attenuation of transmitted pulses can negatively impact the results, especially in thicker or more attenuative materials.
- The method requires well-trained and experienced personnel to operate the equipment and interpret the data accurately.

2.2.5.4 Impact Echo (IE)

The Ultrasonic Pulse Echo (UPE) method is primarily used for detecting defects in concrete, with a particular focus on delamination. This method operates on the principle of striking the surface of the tested object with a low-frequency stress wave and measuring the response at a nearby location (Figure 14). By analyzing the frequency spectrum of the deck's response to an impact, the positions of reflectors, such as voids and delaminations in the concrete, can be identified. In a sound deck, the dominant reflector is typically found at the bottom of the deck, where there is a significant contrast in acoustic impedance between the concrete and the air. However, delaminated areas are detected as shallow reflectors. Other potential reflectors include voids, tendons, and supporting structural elements. Each NDT method, including UPE, has its own capabilities, drawbacks, limitations, and associated uncertainties in measurement and costs. For instance, while UPE can provide detailed information about internal defects, it is time-consuming and requires precise probe coupling on the surface. Additionally, the accuracy of UPE can be affected by various factors such as wave attenuation and surface roughness. To enhance evaluation and interpretation, some methods can be integrated (data fusion), combining their strengths to achieve more comprehensive assessments. Therefore, these methods should be strategically deployed based on the specific requirements and conditions of the inspection task [2].

Figure 14 Impact Echo Equipment [39]

As an application and capabilities of the IE method, the following can be mentioned [2], [6]:

- The Impact Echo (IE) method has a strong potential for rapid data collection and interpretation, making it efficient for large-scale inspections.
- IE is effective in detecting delaminations, cracks, voids, and overlay debonding, even on decks with overlays.
- The method can automate the characterization of delaminations, presenting results in an intuitive and user-friendly manner.
- IE provides precise information on the depth and extent of defects, ensuring reliable assessments.
- It is one of the most reliable and accurate methods for detecting delamination in concrete structures.
- The IE method can also be used to evaluate the modulus of elasticity of concrete, contributing to a comprehensive understanding of material properties.

As limitations of IE the following can be mentioned [2], [6]:

- The size of the slab panel significantly affects the energy reflected from lateral boundaries, which can impact the accuracy of the results.
- IE is tedious and time-consuming due to the need for numerous testing points to cover an area comprehensively.

- The duration of the impact controls the size of the detectable defect, potentially limiting the method's effectiveness for smaller defects.
- The method is less reliable when used on asphalt overlays.
- If there is debonding between the overlay and the deck, IE cannot provide information about the deck's condition beneath the overlay.
- Data collection is conducted on a relatively sparse grid, making the process slow and often requiring lane closures.
- Delamination surveys cannot be conducted on decks with asphalt concrete overlays at higher ambient temperatures due to inaccuracies.
- Detection of rebar and ducts, as well as the evaluation of duct grouting conditions, is limited to relatively shallow depths.
- The evaluation can be influenced by boundary conditions, which may affect the reliability of the results.

3 Benchmark Bridges

Four bridges have been selected by PennDOT for field tests in this project. The table below provides essential information about the bridges under investigation:

Table 1 Information of Bridges

BRkey	22383	22266	22387	22451
County	Lawrence	Lawrence	Lawrence	Lawrence
Bridge_ID	37020801200058	37020801200058	37101600901622	37301000440000
OBJECTID	76057200	76090002	76054370	76087670
Location / Structure Name	PLAIN GROVE TWP O/I79 BRENT NORTH LIB RD BRIDGE	OVER SHENANGO RIVER	2.7 MI N OF PA-108 Plain Grove North Liberty Road	1/2 MI.N.E. OF TR 60
Feature Carried	BRENT NORTH LIB RD	PULASKI RD	Plain Grove N Lib	COVERT RD
Feature Intersected	I-79	SHENANGO RIVER	INTERSTATE 79	LR 1023, PA 60 N.B.
Length (ft)	179	240	235	240
Deck width (ft)	34	36	34	48
Scanned Area (sf)	6,086	8,592	6,580	11,924
# Spans	3	2	5	3
Structure Type	P/S, Box beam - (spread)	P/S, I beam	P/S, Box beam - (spread)	Steel, I-welded beams
Year Built	1986	1986	1963	1973
Latitude	41.10756	41.1133	41.0745	40.9963
Longitude	-80.14517	-80.4372	-80.1281	-80.3890
Average Daily Traffic (Year)	331 (2022) with 10% of truck traffic	2,903 (2022) with 8% of truck traffic	309 (2023) with 9% of truck traffic	2,288 (2021) with 7% of truck traffic
Year Reconstructed	2008	N/A	2008	2007
Satellite View	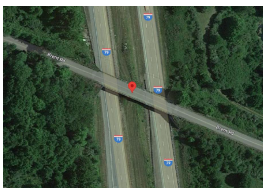			
Deck Condition (rate)	Good (7)	Satisfactory (6)	Satisfactory (6)	Satisfactory (6)
Overall Condition	Good	Fair	Fair	Fair

Figure 15 to Figure 26 show as-built plans of the bridges:

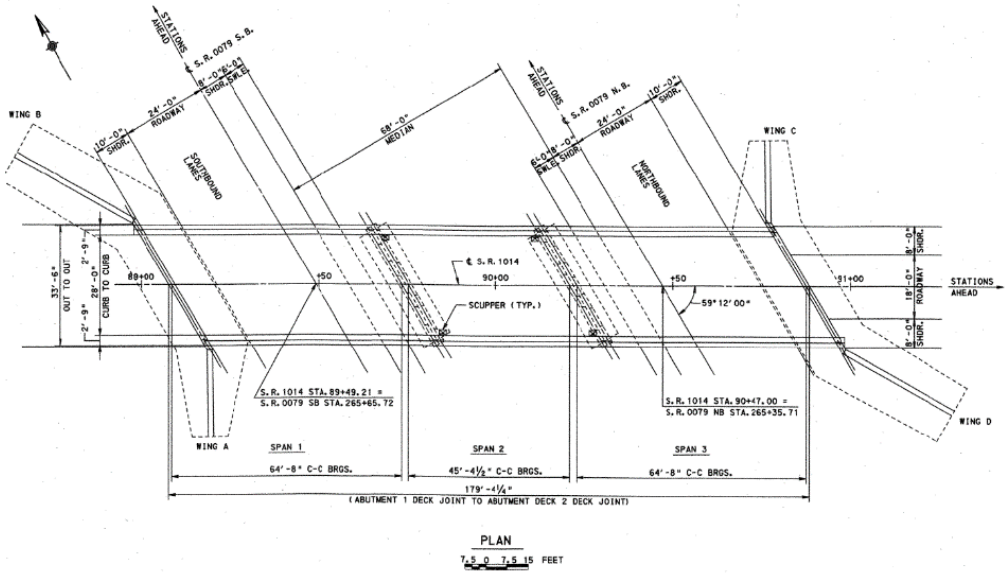

Figure 15 As-Built Plan (Plan View) Bridge No. 22383

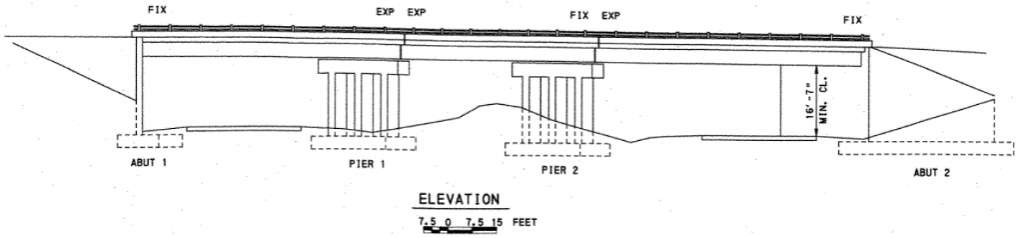

Figure 16 As-Built Plan (Elevation View) Bridge No. 22383

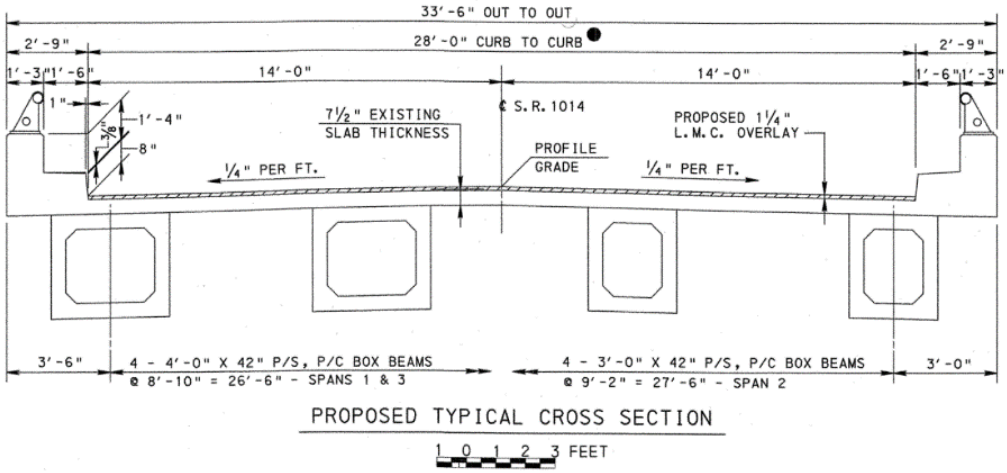

Figure 17 As-Built Plan (Typical Cross Section View) Bridge No. 22383

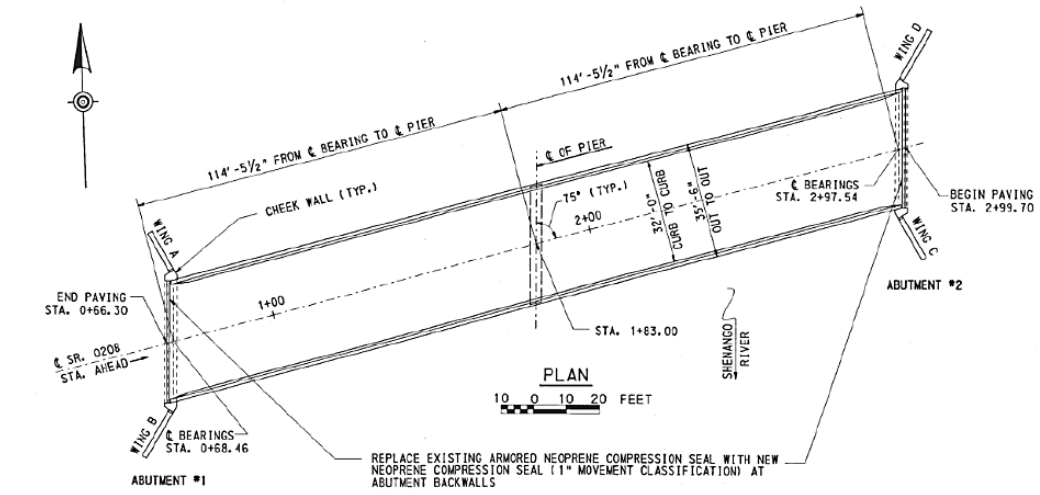

Figure 18 As-Built Plan (Plan View) Bridge No. 22266

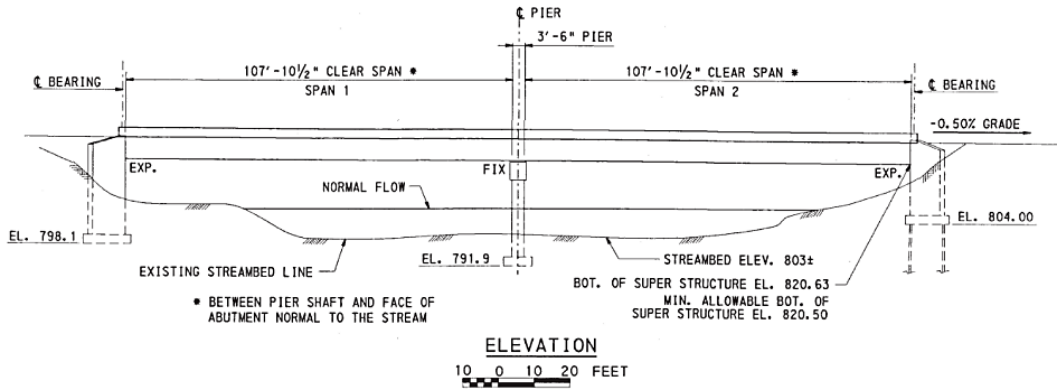

Figure 19 As-Built Plan (Elevation View) Bridge No. 22266

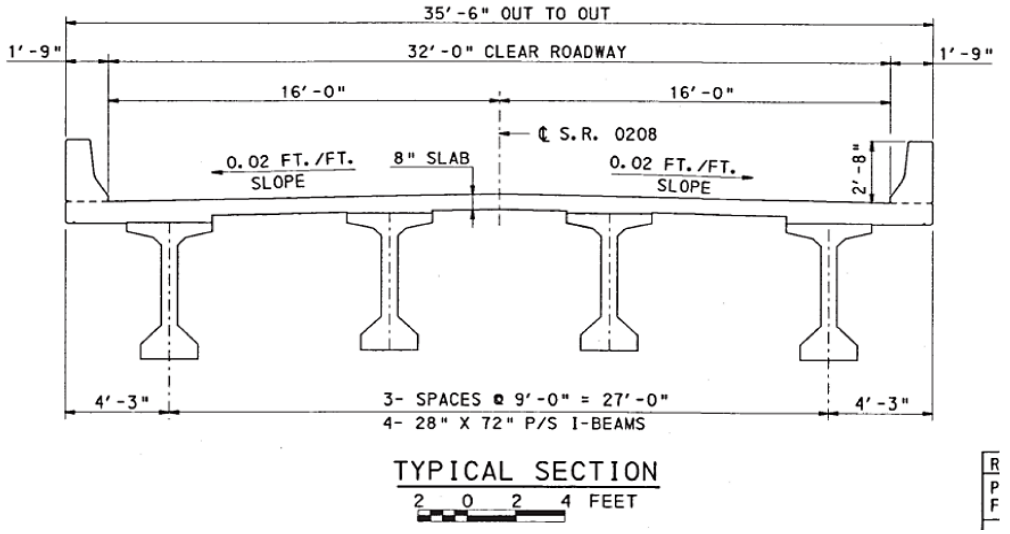

Figure 20 As-Built Plan (Typical Cross Section View) Bridge No. 22266

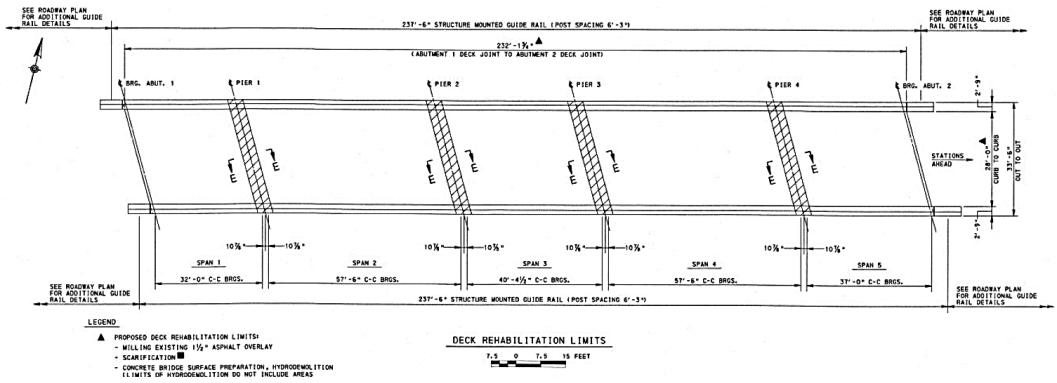

Figure 21 As-Built Plan (Plan View) Bridge No. 22387

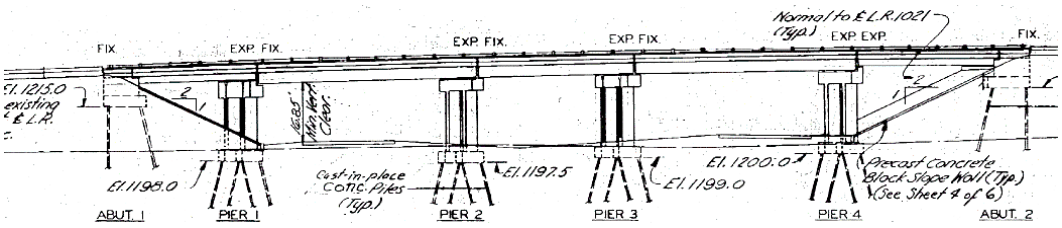

Figure 22 As-Built Plan (Elevation View) Bridge No. 22387

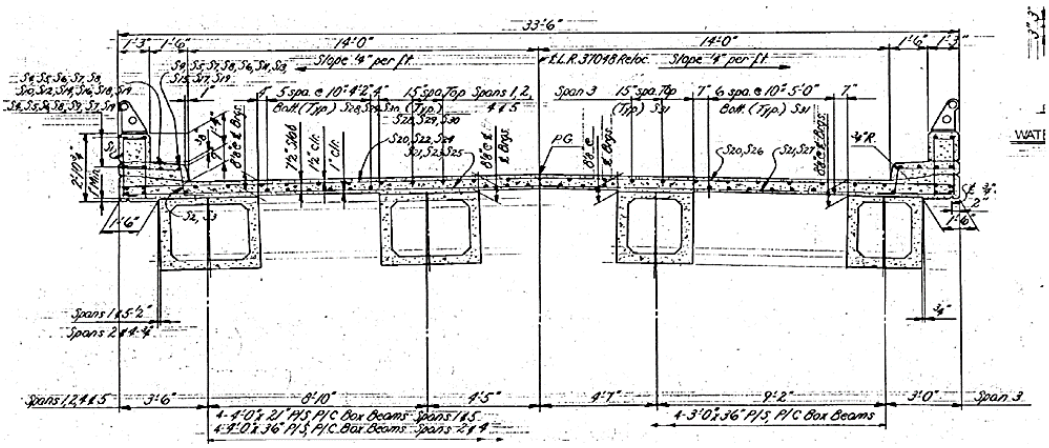

Figure 23 As-Built Plan (Typical Cross Section View) Bridge No. 22387

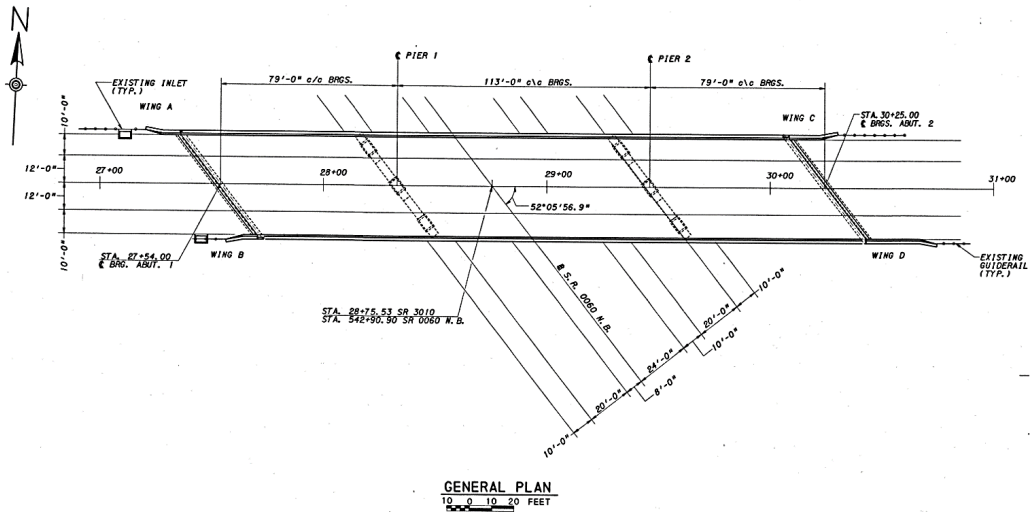

Figure 24 As-Built Plan (Plan View) Bridge No. 22451

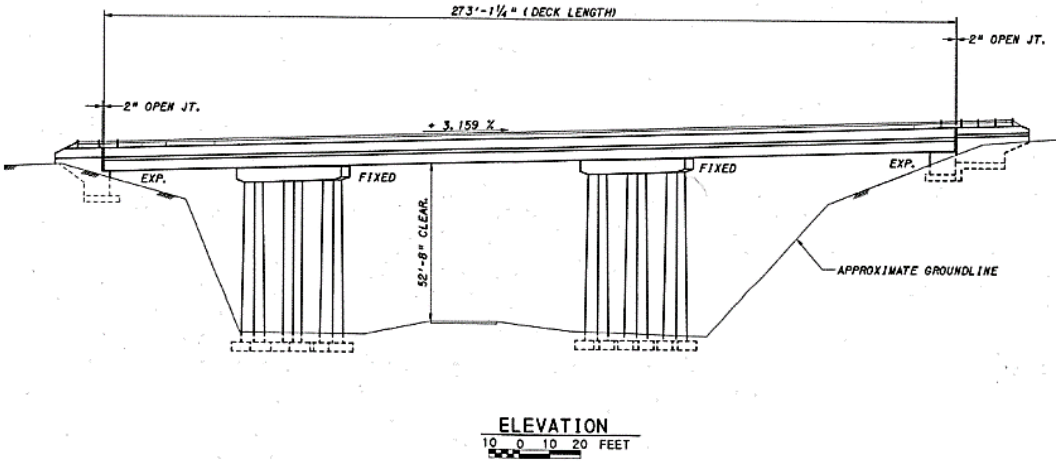

Figure 25 As-Built Plan (Elevation View) Bridge No. 22451

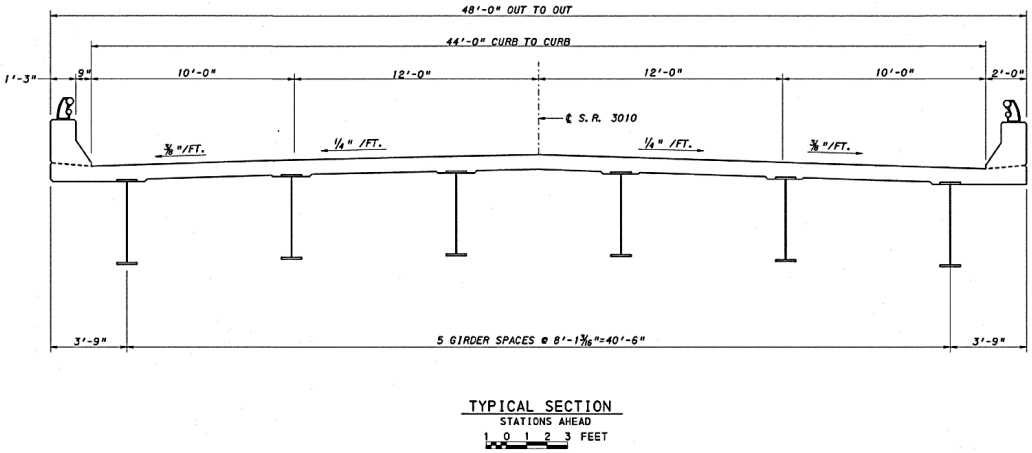

Figure 26 As-Built Plan (Typical Cross Section View) Bridge No. 22451

4 Demonstration of the Field Non-Destructive Testing

This study examines four methods from the categories of digital imaging (Surface Imaging), electro-magnetic (Ground Penetrating Radar), thermal (Infrared Thermography), and acoustic (Chain Dragging). Field non-destructive testing of the four bridges analyzed in this report was performed by two third party companies, Infratek Solutions Inc and NEXCO-West USA.

4.1 Digital Imaging

For visual digital images, NEXCO used Deck Top Scanning System (DTSS) which is a high-speed data collection system (Figure 49). This system includes two High Definition (HD) line-scanning cameras (LSC). These cameras identify surface defects on roadways and bridge decks [28].

Figure 27 High Definition (HD) Visual Inspection [28]

The high-speed images obtained from bridges provided a high-resolution representation of the bridge surface, showing various surface features as well as the surface cracks. Visual digital images of the four bridges analyzed in Kuraves-Actis and AutoCAD software were combined to draw the existing cracks of each bridge. The results of surface imaging provided by both third-party companies for the four bridges are as follow:

4.1.1 Digital Imaging of Bridge No. 22383

Figure 28 shows the digital imaging of bridge No. 22383:

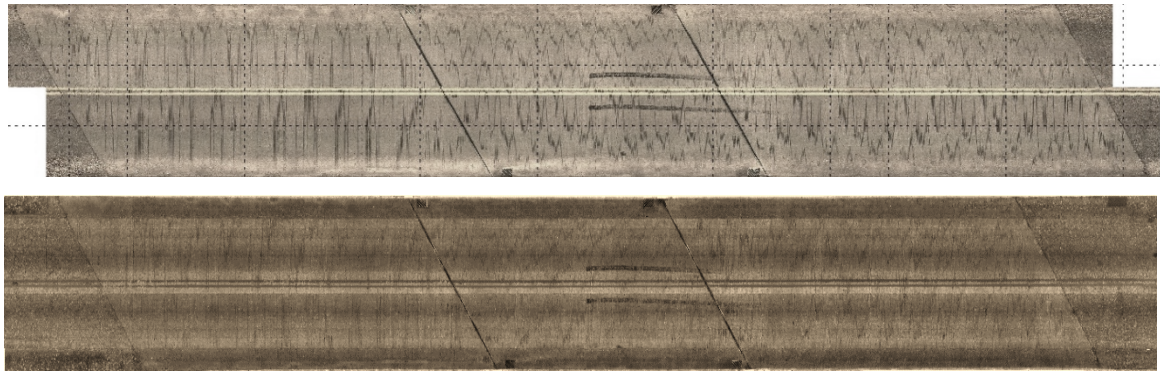

Figure 28 Overall View Images of Bridge Deck No. 22383

4.1.2 Digital Imaging of Bridge No. 22266

Figure 29 shows the digital imaging of bridge No. 22266:

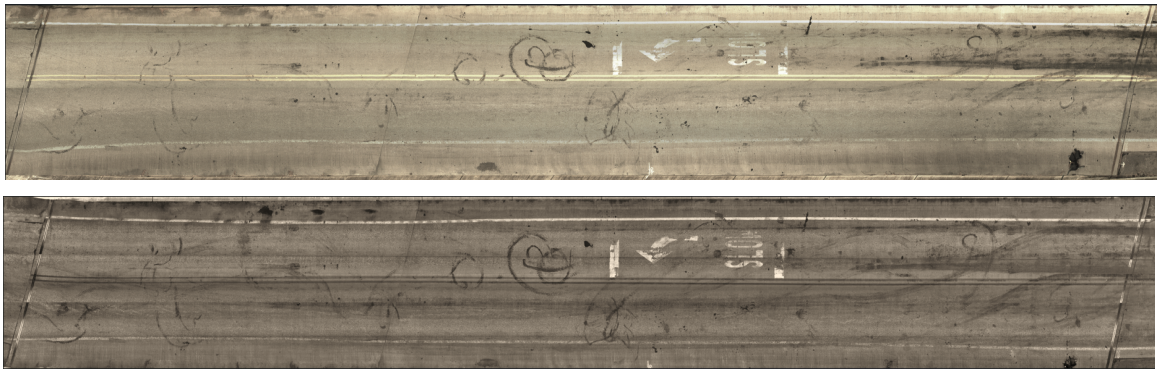

Figure 29 Overall View Images of Bridge Deck No. 22266

4.1.3 Digital Imaging of Bridge No. 22387

Figure 30 shows the digital imaging of bridge No. 22387:

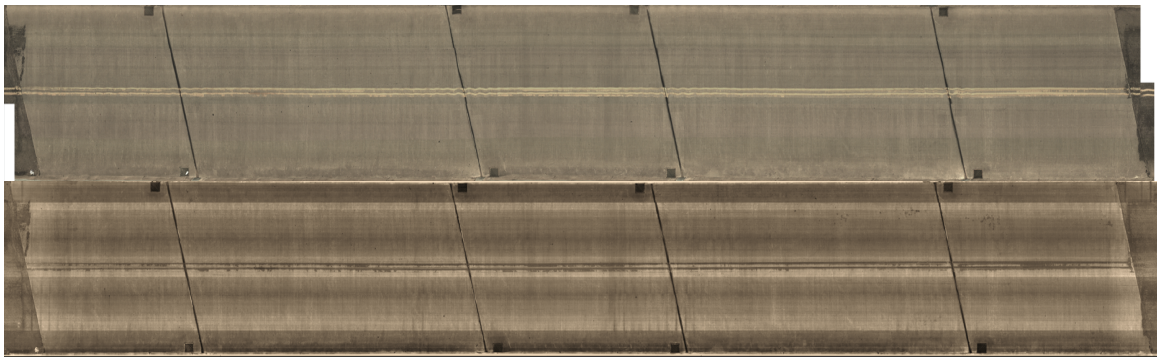

Figure 30 Overall View Images of Bridge Deck No. 22387

4.1.4 Digital Imaging of Bridge No. 22451

Figure 31shows the digital imaging of bridge No. 22451:

Figure 31 Overall View Images of Bridge Deck No. 22451

4.2 Electro-Magnetic (Ground Penetrating Radar (GPR))

The technique provides images of the subsurface by using the electromagnetic spectrum in the microwave range between 10 MHz and 2.6 GHz. These signals are transmitted through the ground and reflect off subsurface structures based on their electrical permittivity. A receiving antenna records variations in the return signals, which the GPR device uses to generate images that generally indicate changes in electrical properties. GPR signals can be used to find a wide range of items, and this subsurface tool is most effective when there is a large difference between the electromagnetic property of the target and surrounding material. GPR device can be used to find corrosion, moisture, debonding, voids, and delamination. Figure 32 shows the GPR system used by Infratek Solutions Inc.

Figure 32 Ground Penetrating Radar System [40]

The GPR data was collected by NEXCO's partner[1] using a mobile ground-coupled antenna manufactured by Kontur (formerly 3D-Radar), the DXG1820 model. The system uses Step-Frequency SF Radar Technology, which utilizes a radar waveform that comprises a sequence of sine waves that progressively increase in frequency. Step frequency ground penetrating radar (SF-GPR) is a type of ground penetrating radar (GPR) that uses a stepped frequency signal to transmit electromagnetic

1- iSee - Innovative Subsurface Evaluation & Engineering, LLC

waves into the ground. The radar receiver then detects the reflected waves and uses them to create an image of the subsurface. SF-GPR would be able to find the areas of deep delamination on the bridge decks. The GPR-DXG1820 is equipped with several technical specifications designed for effective ground-penetrating radar applications. It features a width of 1.8 meters and operates within a frequency range of 200-3000 MHz, utilizing 20 channels with a channel spacing of 75 mm (Cross-Line). This capability allows users to collect data spanning without the need to switch antennas, enhancing efficiency and convenience in practical applications [41].

The effective scan width is 1.5 meters, and it offers direct wave suppression greater than 50 dB. The system uses linear polarization in the in-line direction. Its dimensions are 1.845 meters in length, 0.795 meters in width, and 0.14 meters in height, with a total weight of 38 kg. For transport, the container size is 1.895 meters by 0.92 meters by 0.205 meters, and it has a transport container weight of 32 kg [42].

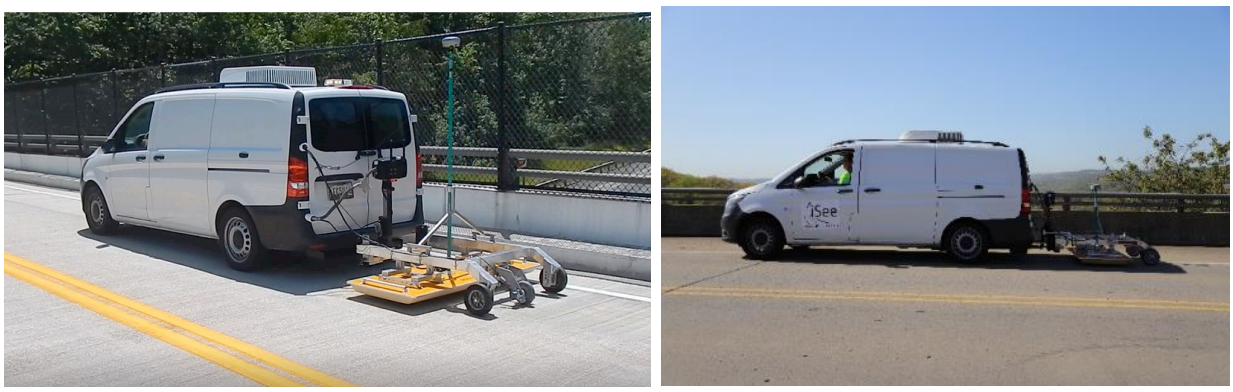

Figure 33 Step Frequency Ground Penetrating Radar [28]

By assessing the phase and amplitude at each frequency, the radar generates a time-domain profile through an inverse Fourier transform of the collected data. Therefore, the step-frequency radar acquires data in the frequency domain, which is subsequently converted into time-domain data through computer processing. The step-frequency waveform offers an optimal source signature featuring a uniform frequency spectrum. With the aid of computer control, users have the ability to define the duration of data acquisition at each frequency and determine the starting and ending frequencies.

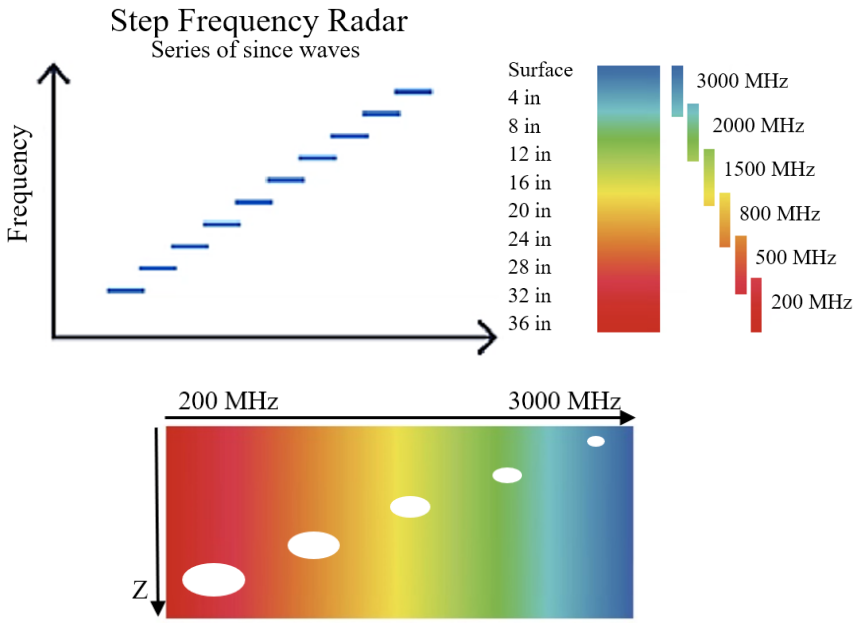

Figure 34 Step-Frequency Radar- Adopted from [42]

For the GPR analysis, the manufacturer's "3D-Examiner" software was used. This software loads the collected data into a pyramidal loading view by GPS positioning. Filtering functions can be applied quickly to large datasets and analysis notation functions are available [28].

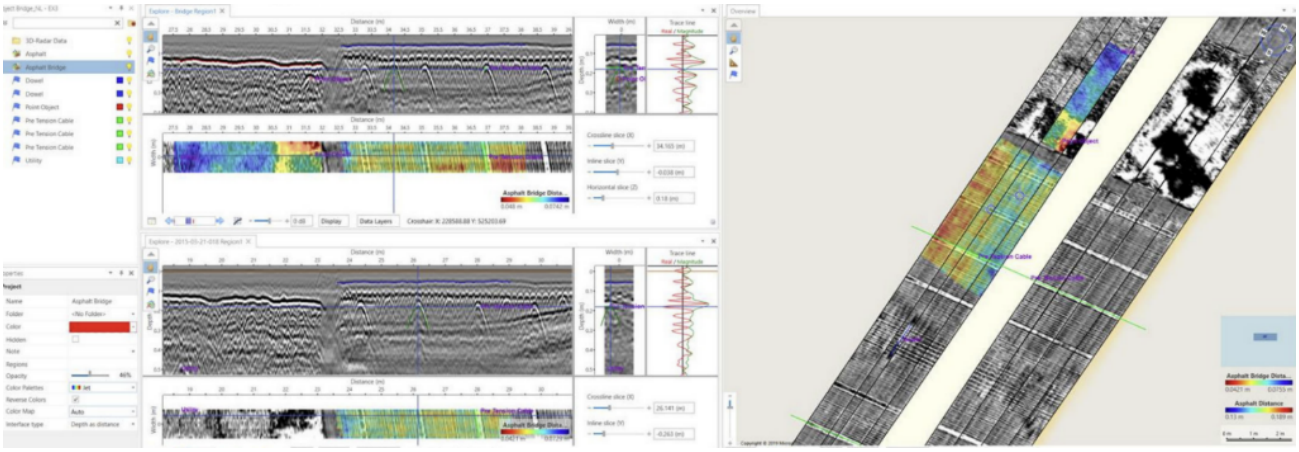

Figure 35 3D-Examiner Software [42]

The outcomes from GPR testing conducted on the four bridges are outlined as follows:

4.2.1 GPR Imaging of Bridge No. 22266

Figure 36 to Figure 38 show the top steel, bellow top steel condition, and cover thickness of the bridge deck No. 22266.

Figure 36 GPR Image Showing Top Steel Condition of Bridge Deck No. 22266

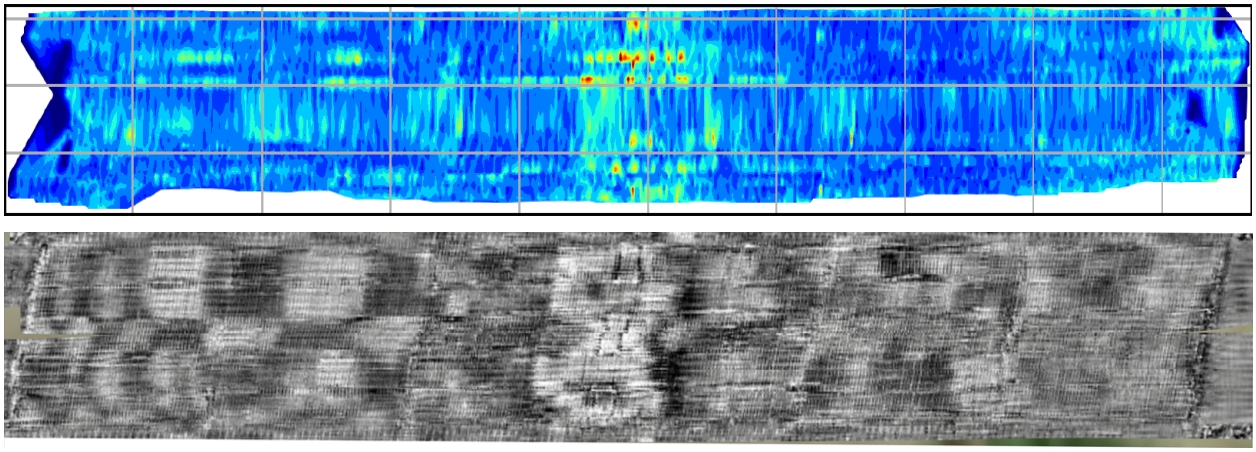

Figure 37 GPR Images Showing Bellow Top Steel Condition of Bridge Deck No. 22266

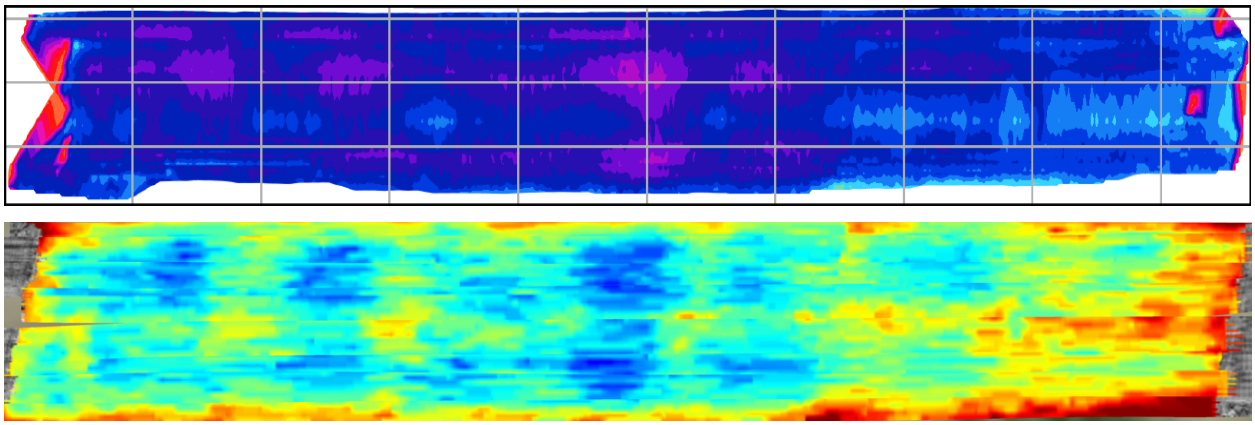

Figure 38 GPR Images Showing Cover Thickness of Bridge Deck No. 22266

4.2.2 GPR Imaging of Bridge No. 22383

Figure 39 to Figure 41 show the top steel, bellow top steel condition, and cover thickness of the bridge deck No. 22383.

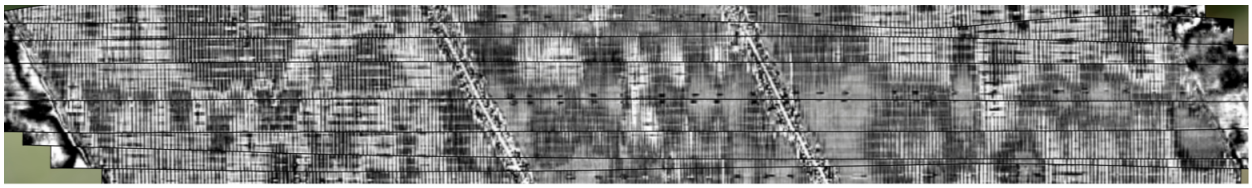

Figure 39 GPR Image Showing Top Steel Condition of Bridge Deck No. 22383

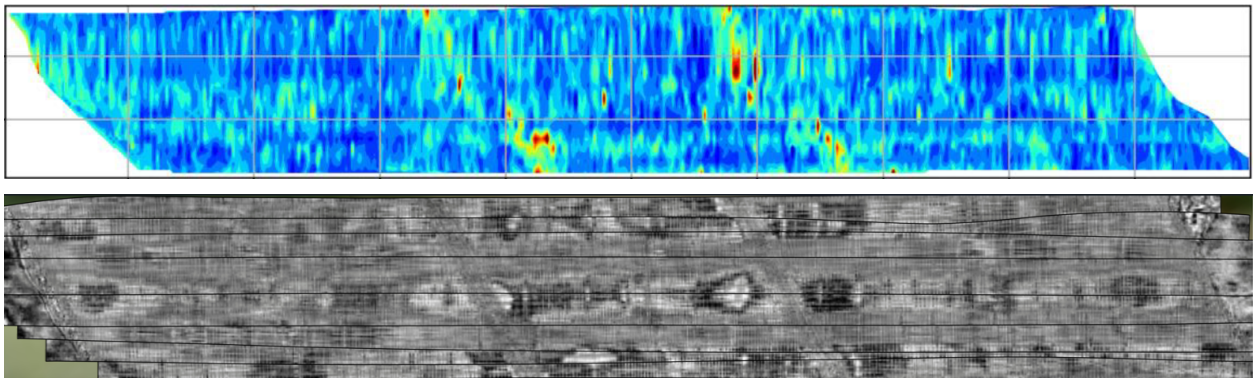

Figure 40 GPR Images Showing Bellow Top Steel Condition of Bridge Deck No. 22383

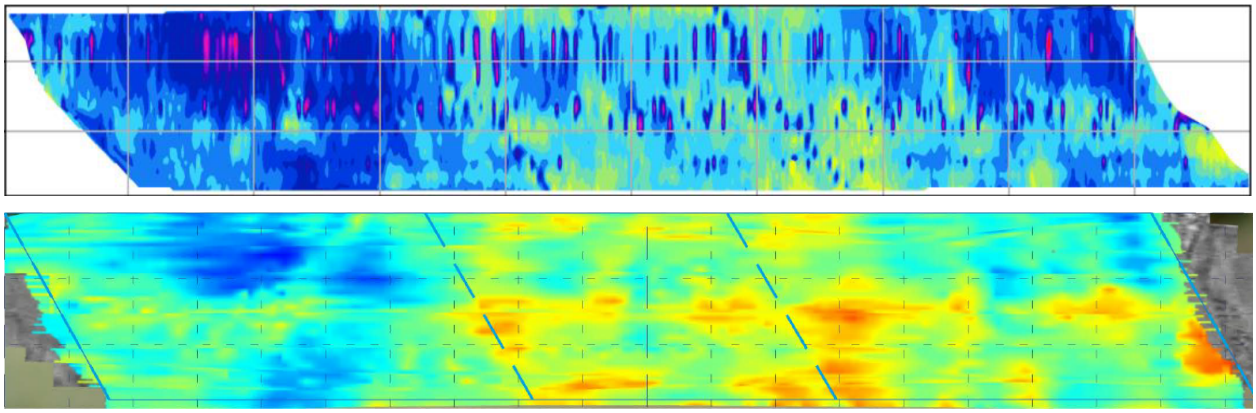

Figure 41 GPR Images Showing Cover Thickness of Bridge Deck No. 22383

4.2.3 GPR Imaging of Bridge No. 22387

Figure 42 to Figure 44 show the top steel and bellow top steel condition and cover thickness of the bridge deck No. 22383.

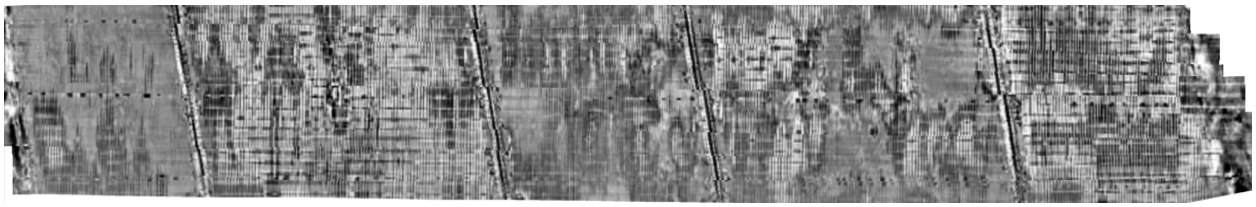

Figure 42 GPR Image Showing Top Steel Condition of Bridge Deck No. 22387

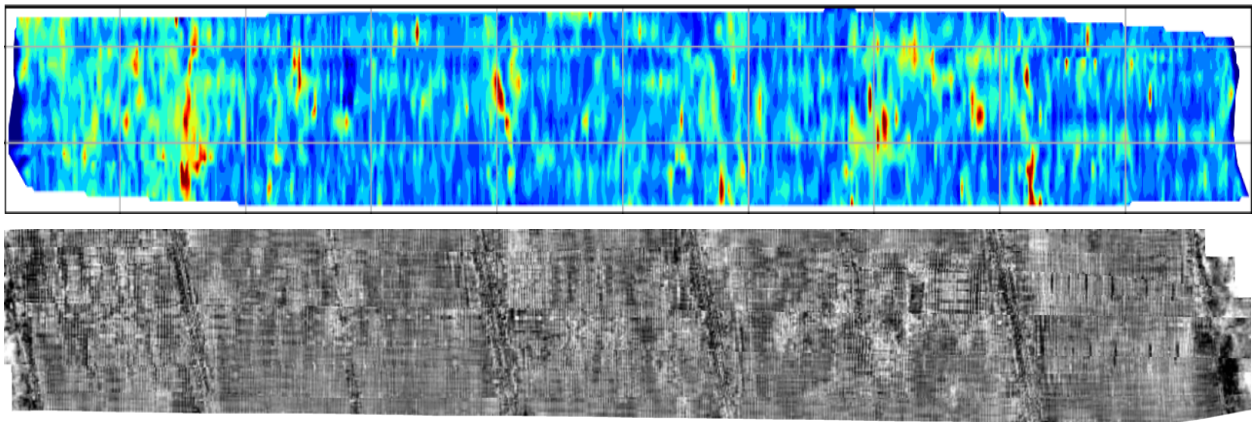

Figure 43 GPR Images Showing Bellow Top Steel Condition of Bridge Deck No. 22387

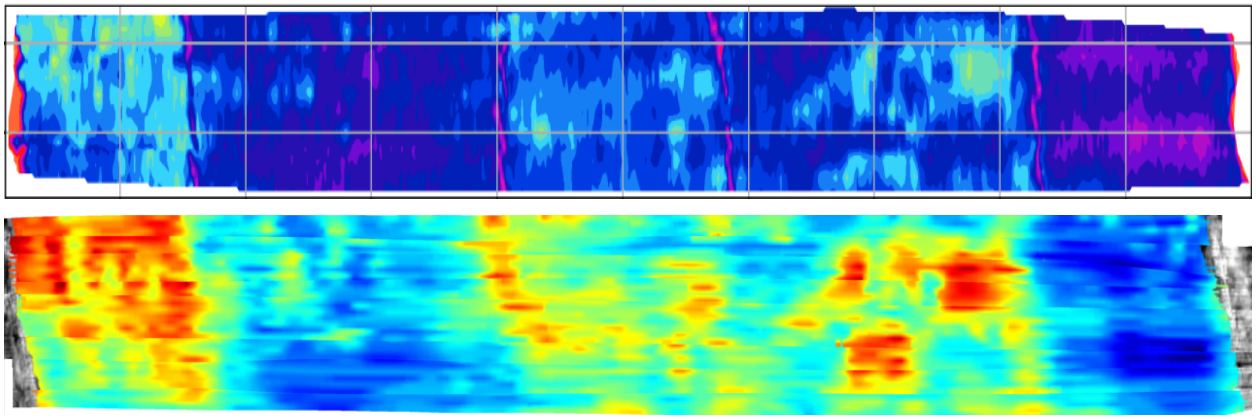

Figure 44 GPR Images Showing Cover Thickness of Bridge Deck No. 22387

4.2.4 GPR Imaging of Bridge No. 22451

Figure 45 to Figure 47 show the top steel and bellow top steel condition and cover thickness of the bridge deck No. 22383.

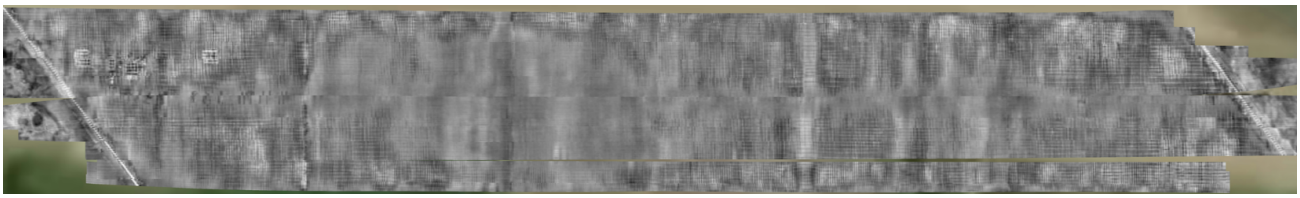

Figure 45 GPR Image Showing Top Steel Condition of Bridge Deck No. 22451

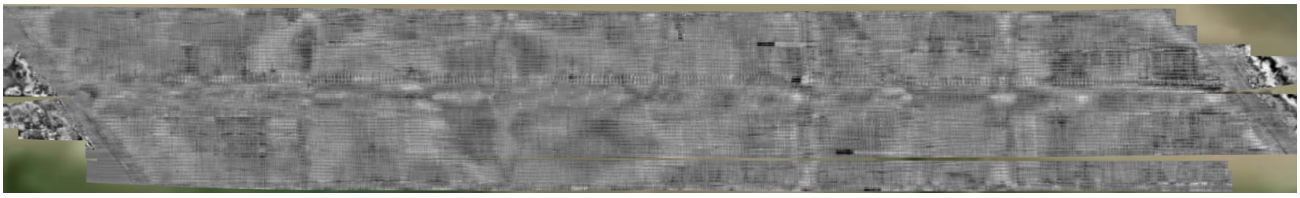

Figure 46 GPR Image Showing Bellow Top Steel Condition of Bridge Deck No. 22451

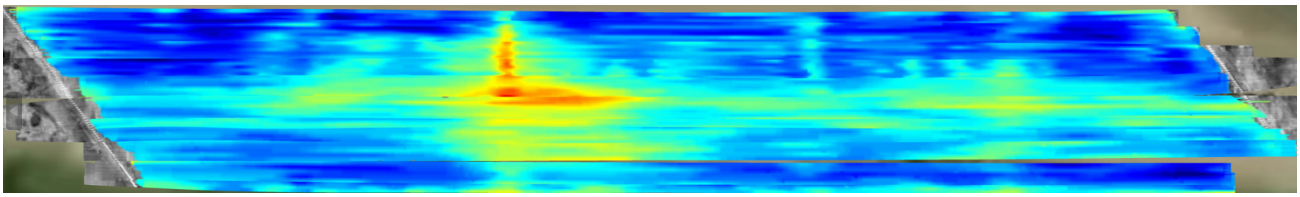

Figure 47 GPR Image Showing Cover Thickness of Bridge Deck No. 22451

4.3 Thermal

For IRT images, Infratek used a High Speed (HS) System, as shown in Figure 48.

Figure 48 High Speed (HS) System Include Infrared Thermography (IRT) [40]

NEXCO used Deck Top Scanning System (DTSS) which is a high-speed data collection system (Figure 49). This system includes FLIR A6701sc infrared camera, a GPS unit, and a speedometer unit. Combined, these sensors identify sub-surface defects on roadways and bridge decks [28].

Figure 49 FLIR A6701sc Camera [43] **and Deck Top Scanning System (DTSS) Include Infrared Thermography (IRT)** [28] [44]

IRT images by NEXCO were collected between 10 pm and 2 pm for daytime (DT) scanning and 7:30 pm to 9:30 pm for nighttime (NT) scanning. The data collection speed for IRT scanning was approximately 35mph, which is the posted speed limit.

4.3.1 Thermal Imaging of Bridge No. 22266

Figure 50 and Figure 51 show the IRT images of the bridge deck No. 22266.

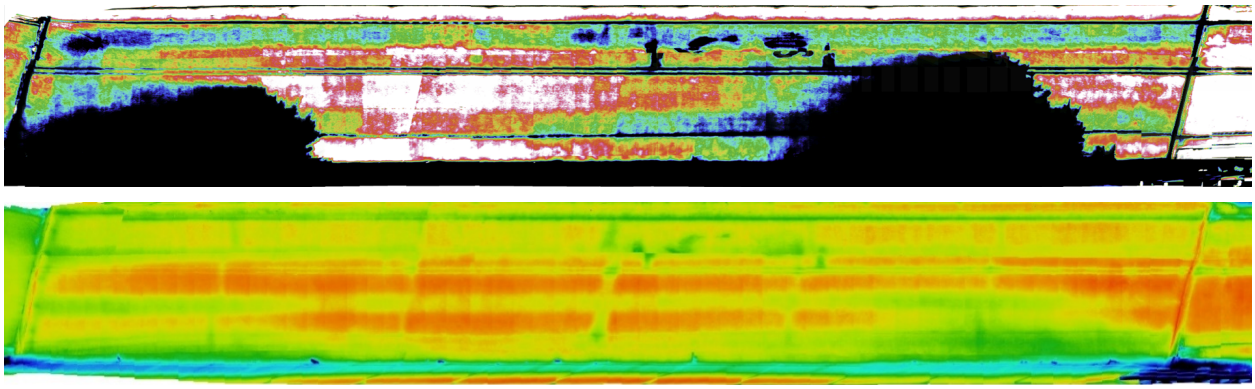

Figure 50 IRT Images of Bridge Deck No. 22266 by NEXCO – Top (Daytime) and Bottom (Nighttime)

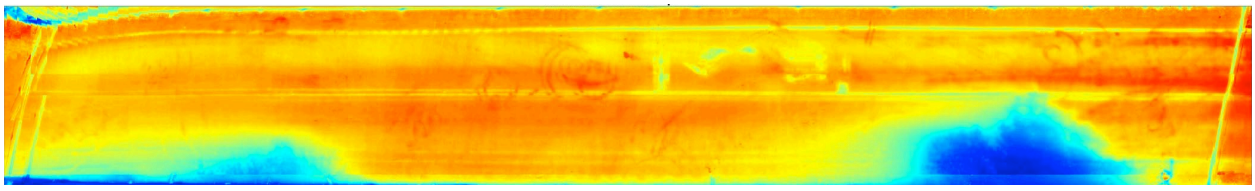

Figure 51 IRT Images of Bridge Deck No. 22266 by Infratek

4.3.2 Thermal Imaging of Bridge No. 22383

Figure 52 and Figure 53 show the IRT images of the bridge deck No. 22383.

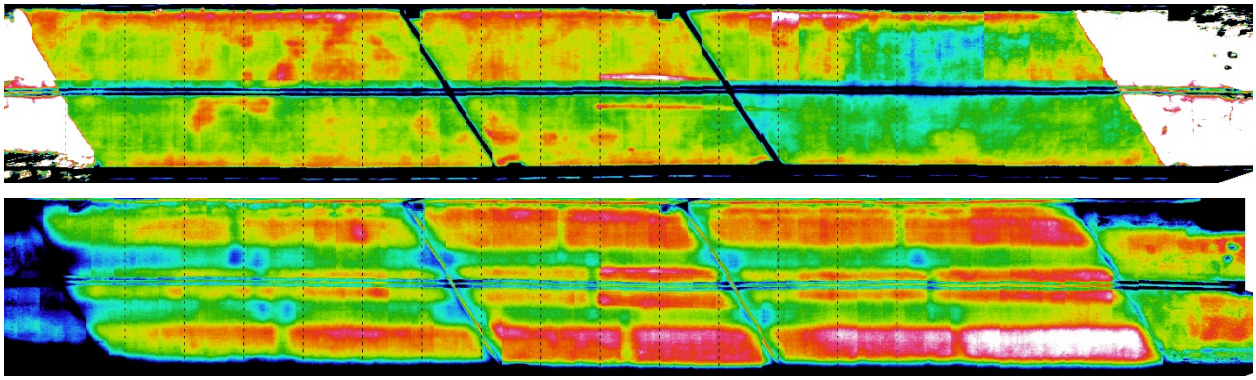

Figure 52 IRT Images of Bridge Deck No. 22383 by Reported NEXCO – Top (Daytime) and Bottom (Nighttime)

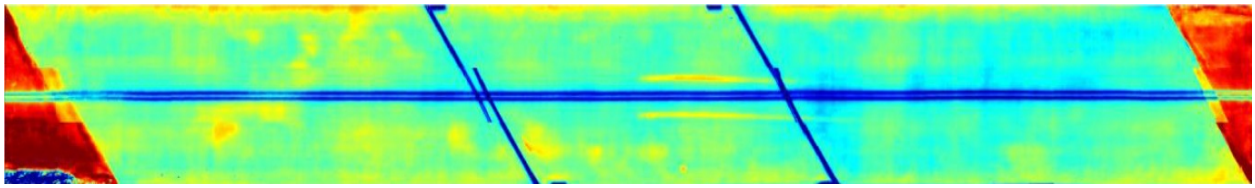

Figure 53 IRT Images of Bridge Deck No. 22383 Reported by Infratek

4.3.3 Thermal Imaging of Bridge No. 22387

Figure 54 and Figure 55 show the IRT images of the bridge deck No. 22387.

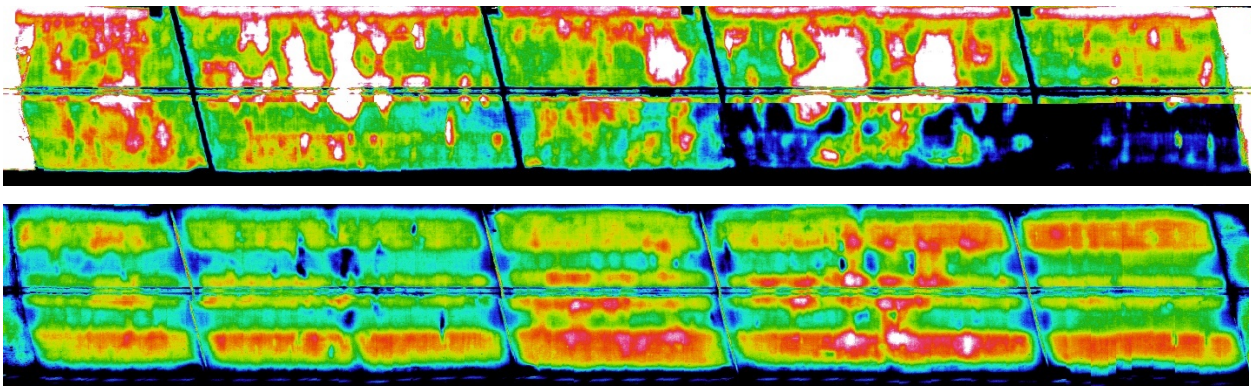

Figure 54 IRT Images of Bridge Deck No. 22387 Reported by NEXCO – Top (Daytime) and Bottom (Nighttime)

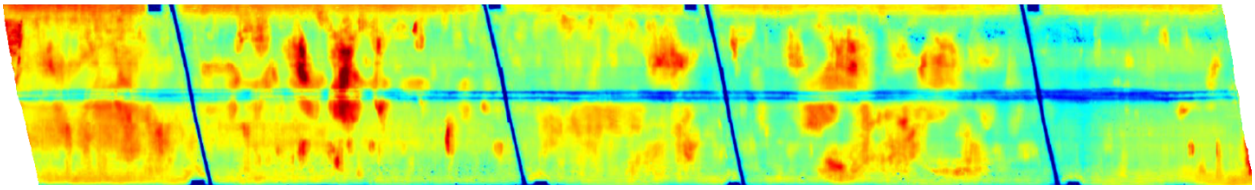

Figure 55 IRT Images of Bridge Deck No. 22387 Reported by Infratek

4.3.4 Thermal Imaging of Bridge No. 22451

Figure 56 shows the IRT images of the bridge deck No. 22451.

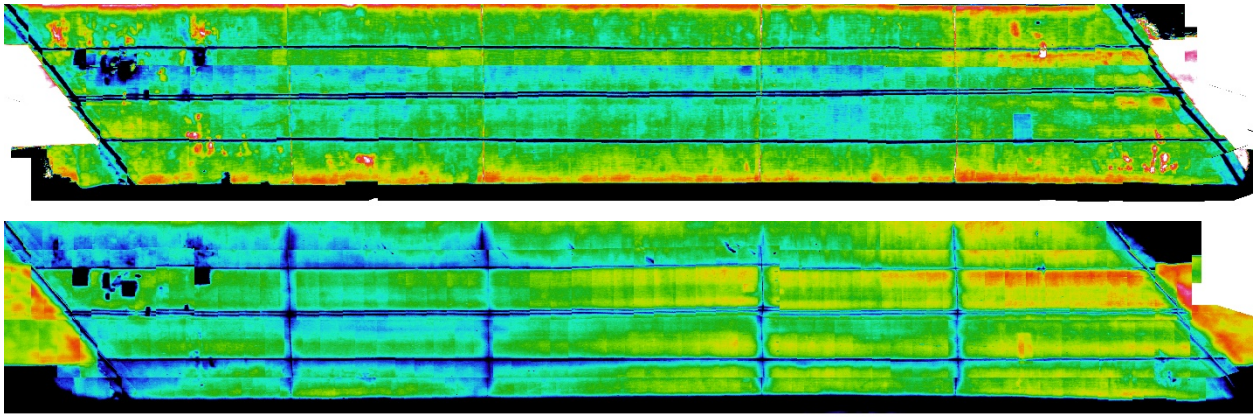

Figure 56 IRT Images of Bridge Deck No. 22451 Reported by NEXCO – Top (Daytime) and Bottom (Nighttime)

4.4 Acoustic

Infratek used High-Speed Sounding (Chain Dragging) for the detection top cover dimension (Figure 57). When the chain passes over a delaminated area, where the top layer of concrete has separated from the underlying layers, the sound changes. This change is usually a hollow or duller sound compared to the crisp ring produced by intact concrete. The sound test was also done by PennDOT's Engineering District 11.

Figure 57 High Speed Sounding (Chain Dragging) [40]

4.4.1 Acoustic Imaging of Bridge No. 22266

Figure 58 shows the deck sounding result of the bridge deck No. 22266.

Figure 58 Contour Map of Sound Test of Bridge Deck No. 22266

PennDOT's engineering district 11 reported no delamination found in bridge deck No. 22266.

4.4.2 Acoustic Imaging of Bridge No. 22383

Figure 59 and Figure 60 show deck sounding result of the bridge deck No. 22383.

Figure 59 Contour Map of Sound Test of Bridge Deck No. 22383

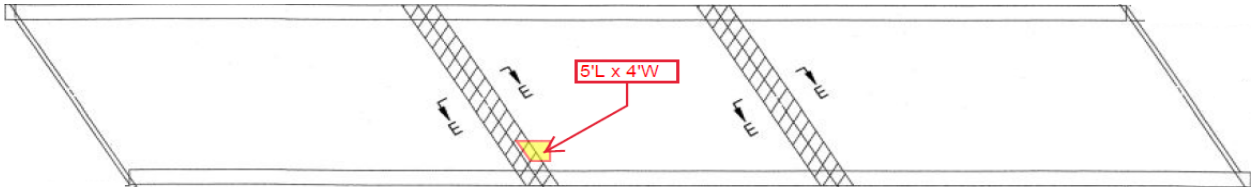

Figure 60 Map of Sound Test of Bridge Deck No. 22383-Reported by District 11

4.4.3 Acoustic Imaging of Bridge No. 22387

Figure 59 and Figure 60 show deck sounding result of the bridge deck No. 22387.

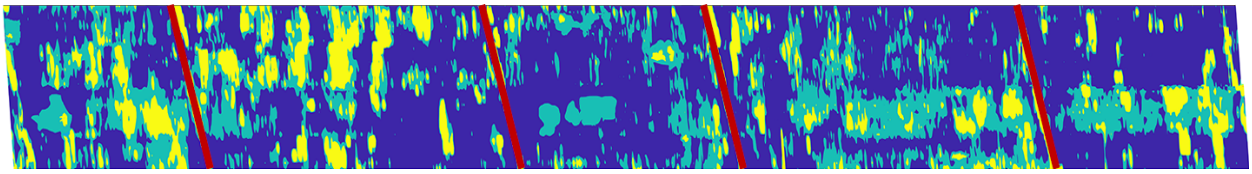

Figure 61 Contour Map of Sound Test of Bridge No. 22387

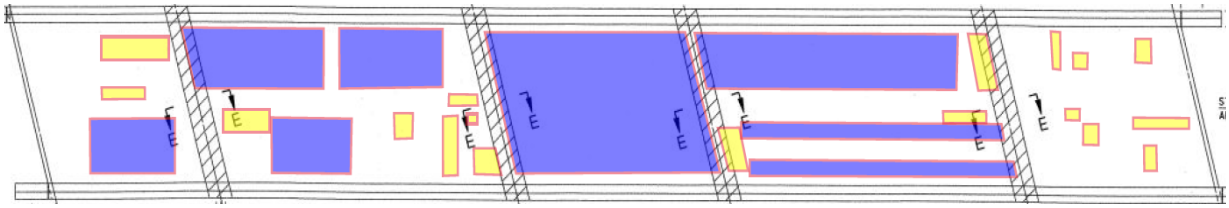

Figure 62 Map of Sound Test of Bridge No. 22387 Reported by District 11

Note: large areas of the wearing surface sounded like the latex overlay was not adequately bonded. These areas are generally marked in blue.

4.4.4 Acoustic Imaging of Bridge No. 22451

Figure 63 shows the deck sounding result of the bridge deck No. 22451.

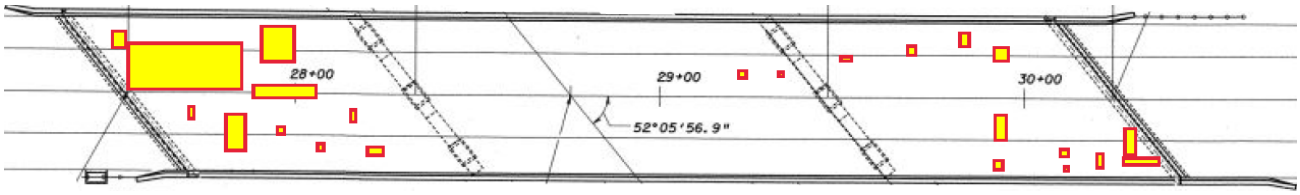

Figure 63 Map of Sound Test of Bridge No. 22451 Reported by District 11

5 Filed Data Analysis

5.1 Surface Image Analysis

Surface images of the four bridges analyzed in this report were processed using Kuraves-Actis and AutoCAD software. These programs were utilized to merge the images and delineate the existing cracks on each bridge.

According to the appendix A total length of cracks of bridge deck No. 22383 is as follow:

Table 2 Length of Cracks of Bridge Deck No. 22383

Bridge No. 22383	Span 1	Span 2	Span 3	Total
Crack length (ft)	184.11	140.25	115.47	439.83
Span Area (ft^2)	1939.5	1390.2	1914	5307
Ratio (ft/ft^2)	0.095	0.100	0.06	0.083

Figure 64 to Figure 67 show existing cracks of bridge No. 22383:

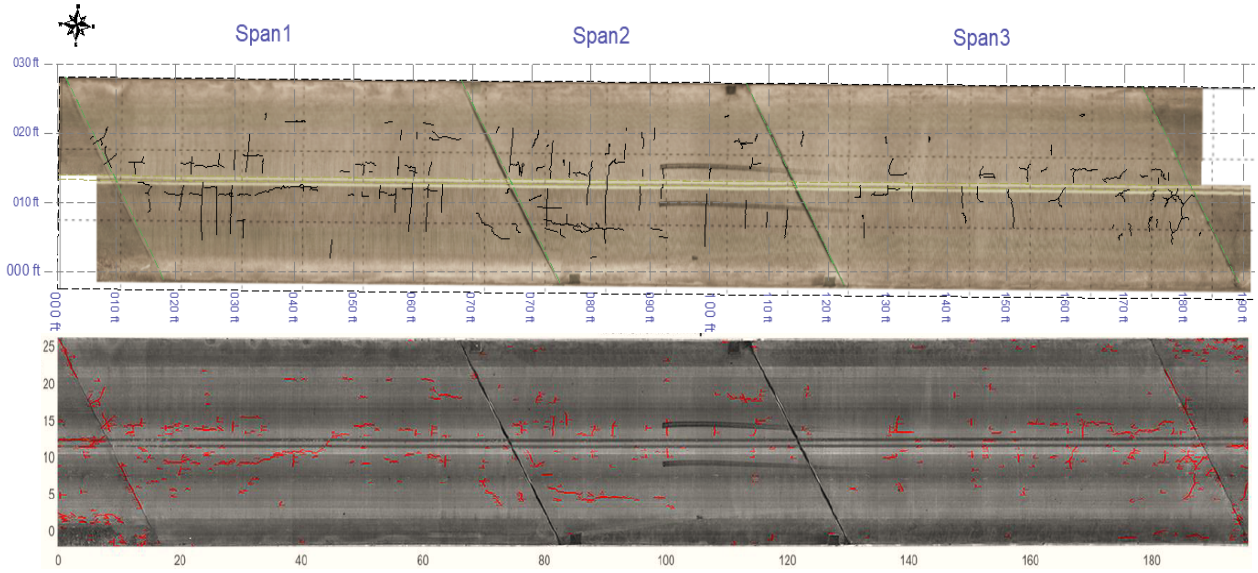

Figure 64 Existing Cracks of Bridge Deck No. 22383-Overall View Image

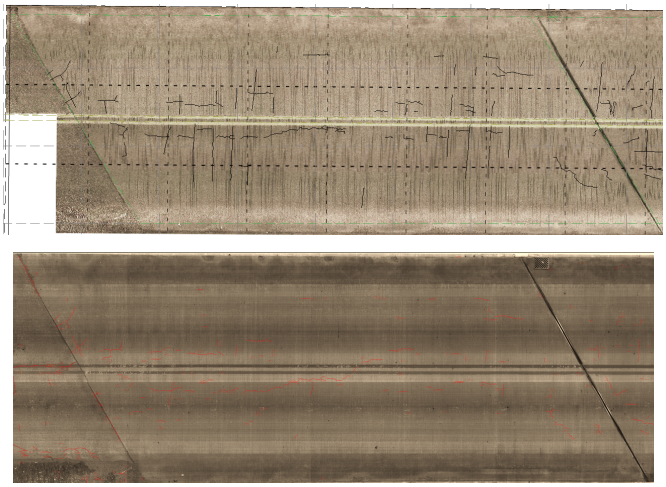

Figure 65 Existing Cracks of Bridge Deck No. 22383-Span 1

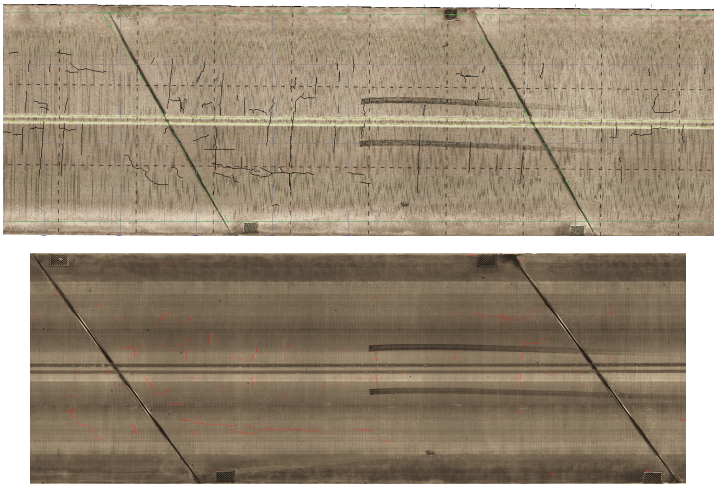

Figure 66 Existing Cracks of Bridge Deck No. 22383-Span 2

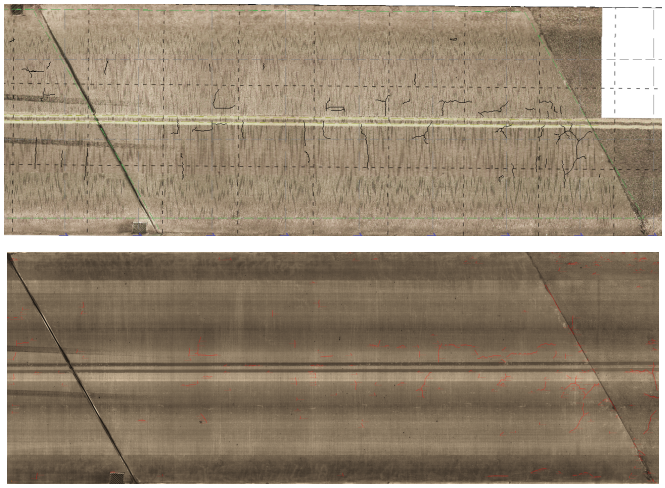

Figure 67 Existing Cracks of Bridge Deck No. 22383-Span 3

5.1.1 Digital Imaging of Bridge No. 22266

According to the appendix A total length of cracks of bridge deck No. 22266 is as follow:

Table 3 Length of Cracks of Bridge Deck No. 22266

Bridge No. 22266	Span 1	Span 2	Total
Crack length (ft)	20.28	69.22	89.50
Span Area (ft^2)	2575.6	5131.8	7665.9
Ratio (ft/ft^2)	0.008	0.013	0.012

Figure 68 to Figure 70 show existing cracks of bridge deck No. 22266:

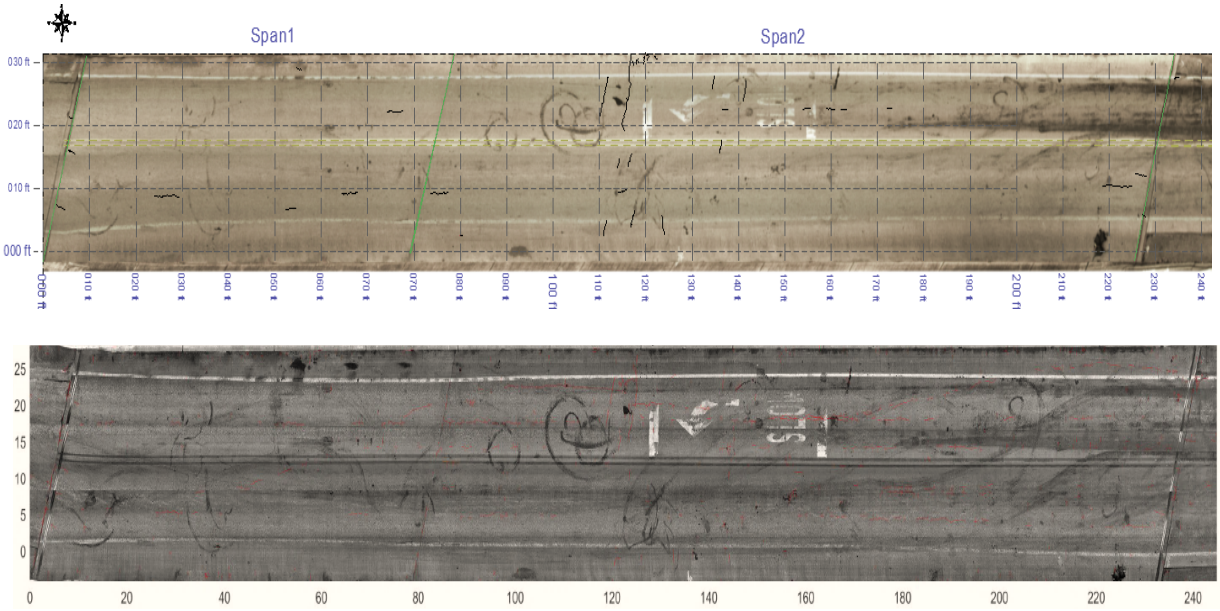

Figure 68 Existing Cracks of Bridge Deck No. 22266-Overall View Image

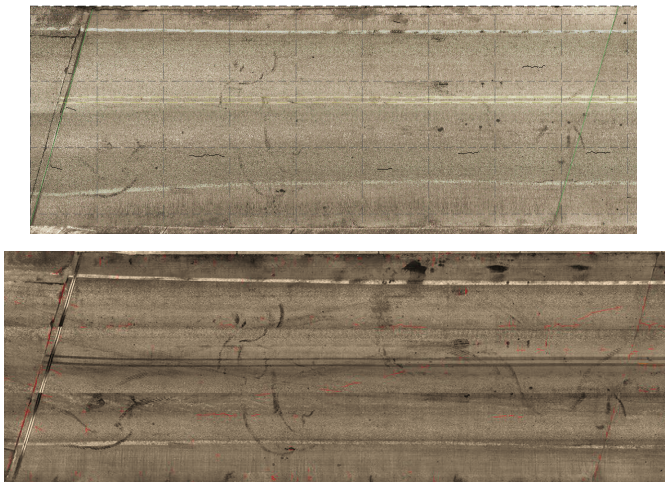

Figure 69 Existing Cracks of Bridge Deck No. 22266-Span 1

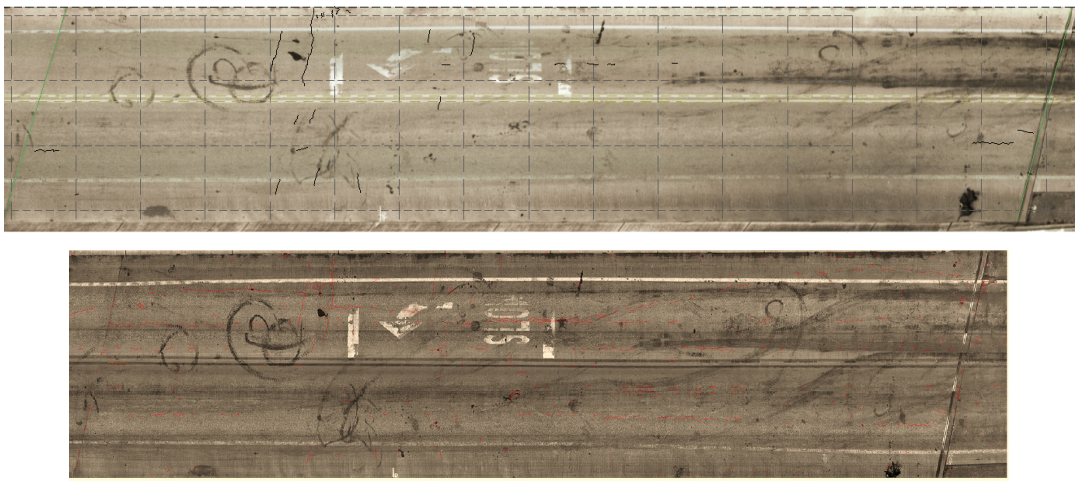

Figure 70 Existing Cracks of Bridge Deck No. 22266-Span 2

5.1.2 Digital Imaging of Bridge No. 22387

According to the appendix A total length of cracks of bridge deck No. 22387 is as follow:

Table 4 Length of Cracks of Bridge Deck No. 22387

Bridge No. 22387	Span 1	Span 2	Span 3	Span 4	Span 5	Total
Crack length (ft)	112.73	121.96	243.86	126.10	37.91	642.56
Span Area (ft^2)	943.9	1695.6	1198.5	1712.6	1105.9	6669
Ratio (ft/ft^2)	0.119	0.072	0.203	0.074	0.034	0.096

Figure 71 to Figure 76 show existing cracks of bridge deck No. 22387:

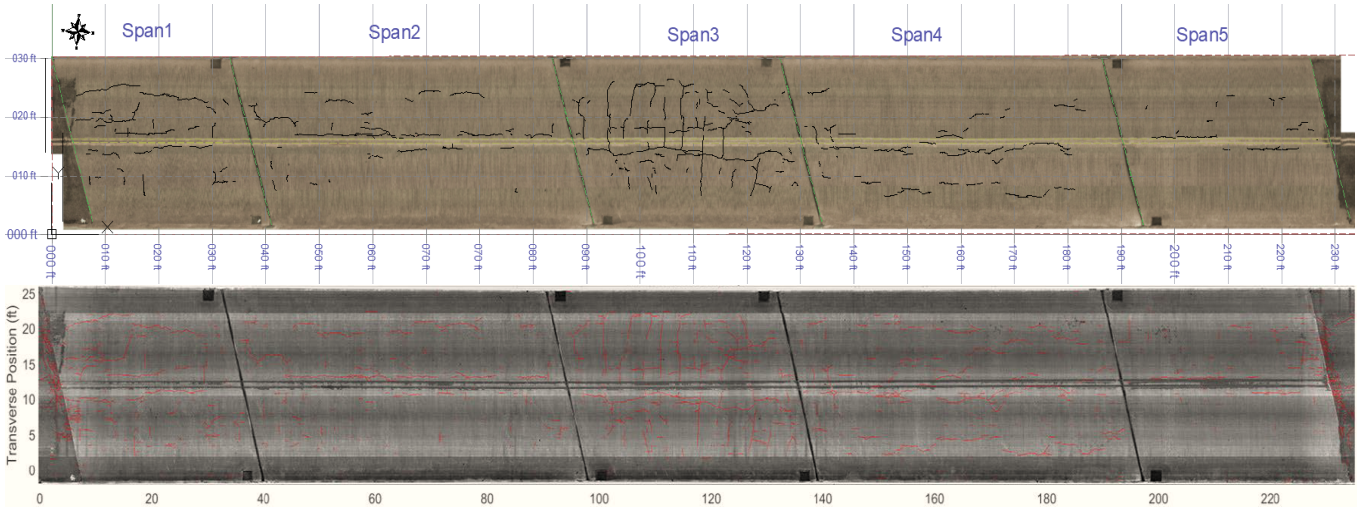

Figure 71 Existing Cracks of Bridge Deck No. 22387- Overall View Image

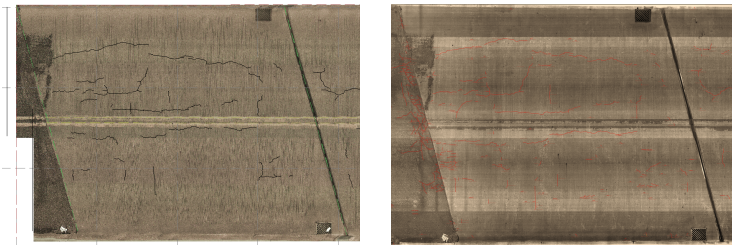

Figure 72 Existing Cracks of Bridge Deck No. 22387- Span 1

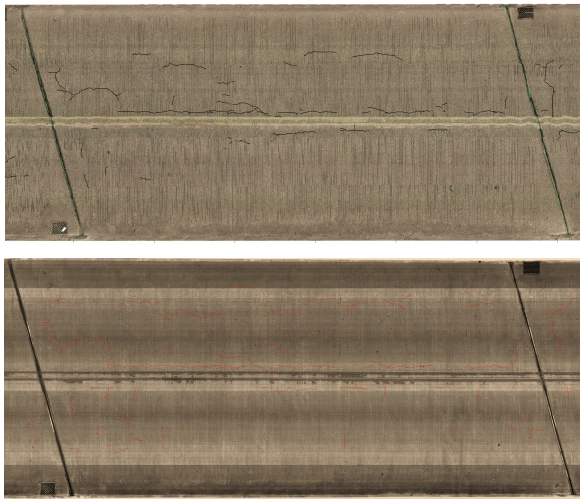

Figure 73 Existing Cracks of Bridge Deck No. 22387- Span 2

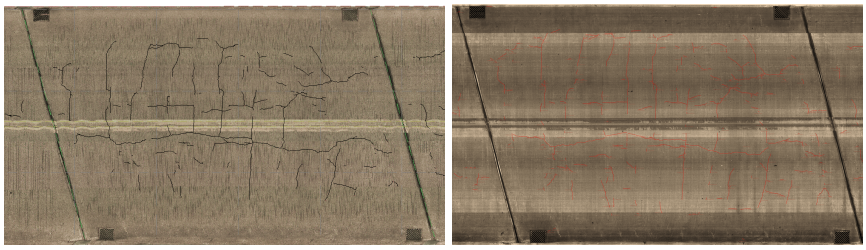

Figure 74 Existing Cracks of Bridge Deck No. 22387- Span 3

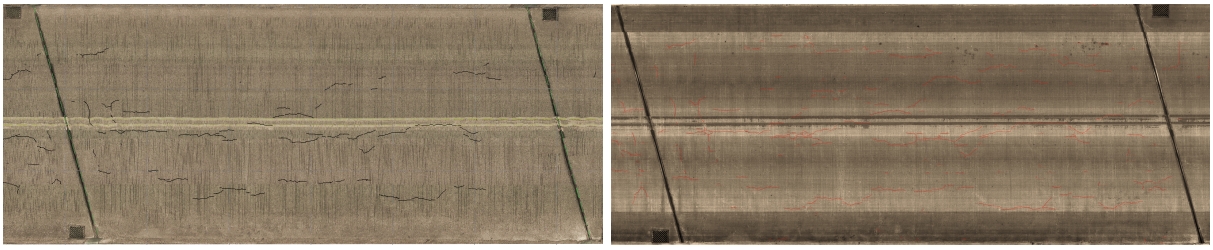

Figure 75 Existing Cracks of Bridge Deck No. 22387-Span 4

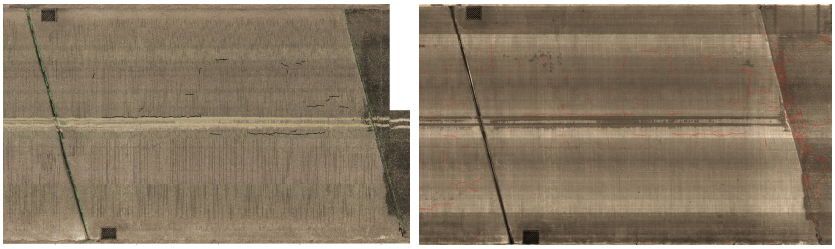

Figure 76 Existing Cracks of Bridge Deck No. 22387-Span 5

5.1.3 Digital Imaging of Bridge No. 22451

According to the appendix A total length of cracks of bridge deck No. 22451 is as follow:

Table 5 Length of cracks of bridge No. 22451

Bridge No. 22451	Span 1	Span 2	Span 3	Total
Crack length (ft)	51.67	29.03	53.95	134.65
Span Area (ft^2)	3579.8	5041.0	3638.6	12294.8
Ratio (ft/ft^2)	0.014	0.006	0.015	0.011

Figure 77 to Figure 80 show existing cracks of bridge deck No. 22451:

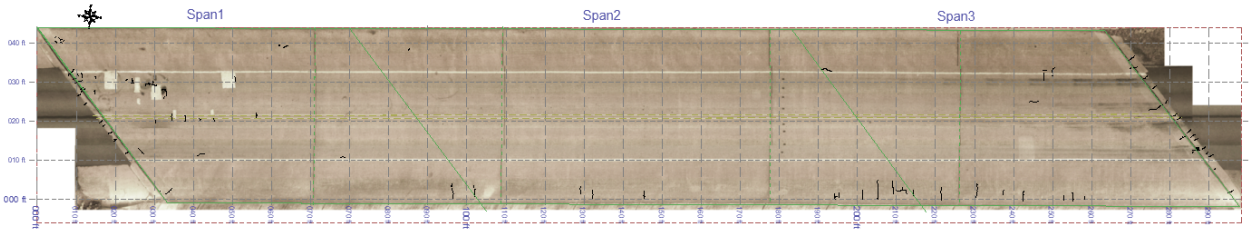

Figure 77 Existing Cracks on Bridge Deck No. 22451- Overall View Image

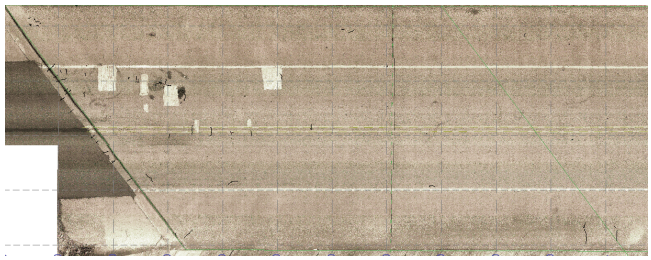

Figure 78 Existing Cracks on Bridge Deck No. 22451-Span 1

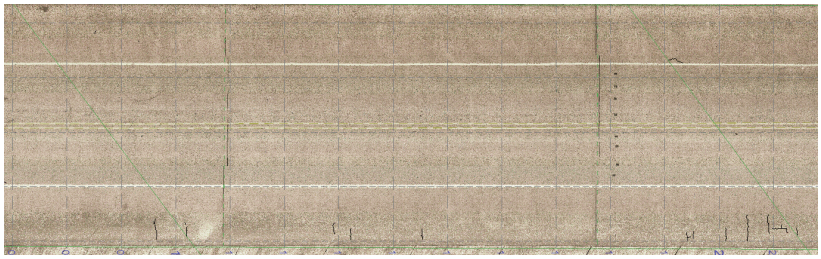

Figure 79 Existing Cracks on Bridge Deck No. 22451-Span 2

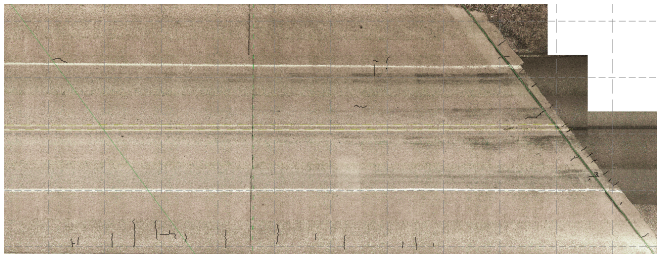

Figure 80 Existing Cracks on Bridge Deck No. 22451-Span 3

5.2 Infrared Thermography (IRT) Image Analysis

For the current study, the fieldwork was conducted during daytime and nighttime periods for the detection of delaminations in bridge decks. The mechanism for detecting delaminations during both daytime and nighttime is briefly described, as illustrated in Figure 81. During daylight hours, the sun's energy warms the concrete surface. If a delamination is present within the concrete deck, heat accumulates above it because the thermal conductivity of air (approximately 0.024 W/m°C) is much lower than that of concrete (ranging from 0.4 to 1.8 W/m°C). Consequently, the energy from the trapped heat is redirected towards the surface. Consequently, the concrete surface above the delaminations becomes warmer than its surroundings during the daytime. Conversely, during nighttime, the heat is radiated upward to the sky, causing the trapped heat volume to reside beneath the delamination. Consequently, the concrete surface above the delamination becomes cooler than its surroundings during nighttime. By employing an IR camera to capture thermal images at an opportune moment, defects can be identified based on temperature variations between the delaminated and surrounding areas [45].

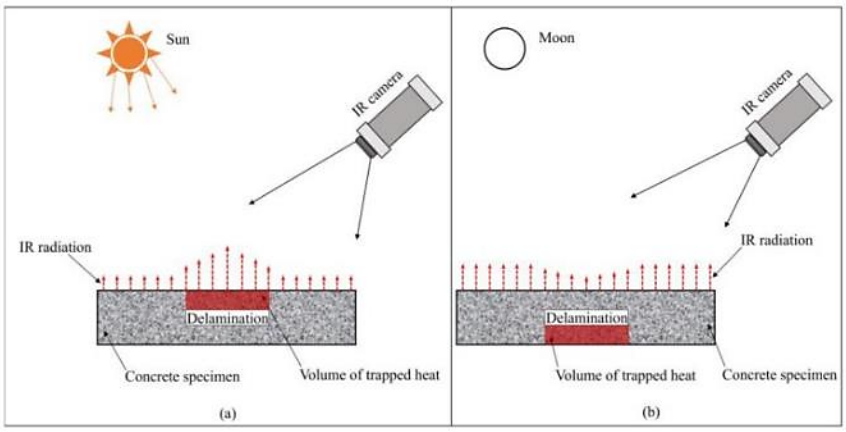

Figure 81 Principles of Defect Identification with Passive Infrared Thermography: (A) In Daylight Conditions; (B) In Nighttime Conditions [45]

IRT images of four bridges are selected from NEXCO West USA data. The raw data provided by them is in (*.kwt) format. Kuraves-Actis software was used to read and work with the data. AutoCAD software was also used to draw the delamination of each bridge. The relationship between temperature changes and delamination in materials or structures is primarily based on the differences in thermal properties and behavior of the delaminated region compared to the surrounding intact material. Delaminated regions often act as thermal insulators, meaning they do not conduct heat as effectively as the surrounding material. As a result, during a thermal stimulus (e.g., heating or cooling), these areas may heat up or cool down more slowly than the surrounding material. Combining IRT with other non-destructive testing methods such as Ground Penetrating Radar (GPR) or Ultrasonic Testing (UT) can provide more accurate information about delamination depth. The effectiveness of IRT for delamination detection depends on factors like the width-to-depth ratio of delaminations. Studies suggest that passive IRT techniques can detect shallow delamination (delaminations at depths of up to 4 cm from the structure's surface under specific conditions) [45] while GPR technology can detect beneath this shallow range into deeper depths. Shallow defects or anomalies in a material's surface tend to exhibit higher thermal contrast in IRT images. This is because these defects are closer to the surface, and their heat transfer properties differ significantly from the surrounding material. As a result, temperature differences are more pronounced, leading to a higher thermal contrast [46], [47].

5.2.1 Bridge No. 22383

Figure 82 to Figure 84 show existing delamination of bridge No. 22383. The light red hatches can be deep delamination (to top of steel) and dark reds can be shallow. Ground Penetrating Radar (GPR) can provide more accurate information about delamination depth.

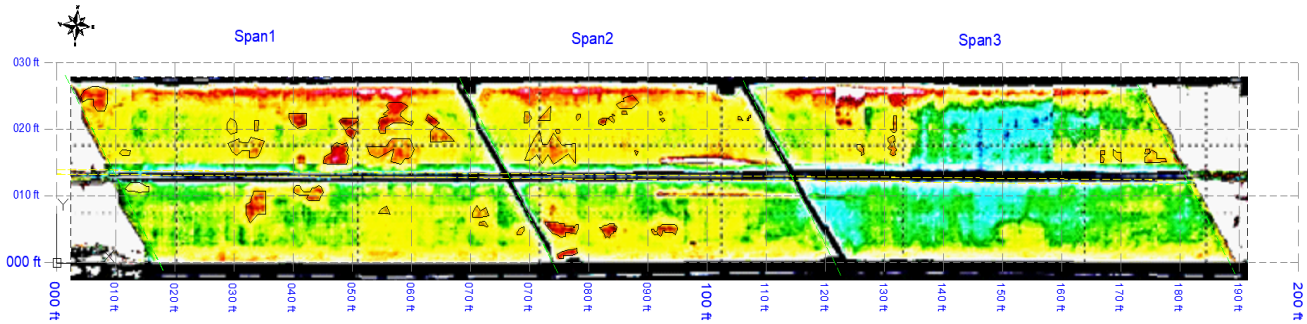

Figure 82 Existing Delamination in The IRT Image of Bridge Deck No. 22383

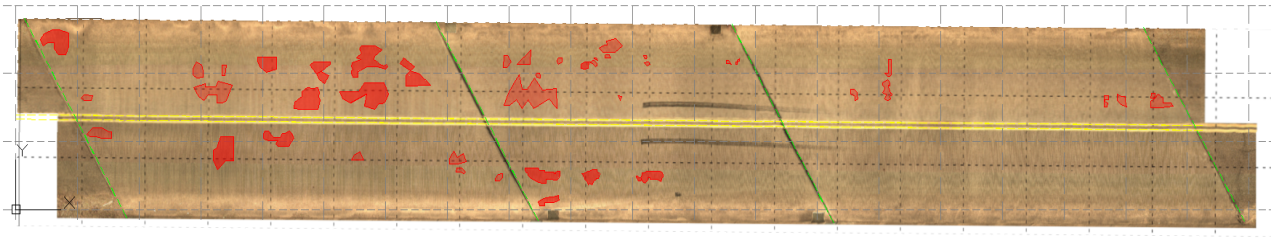

Figure 83 Existing Delamination in the Visual Image of Bridge Deck No. 22383

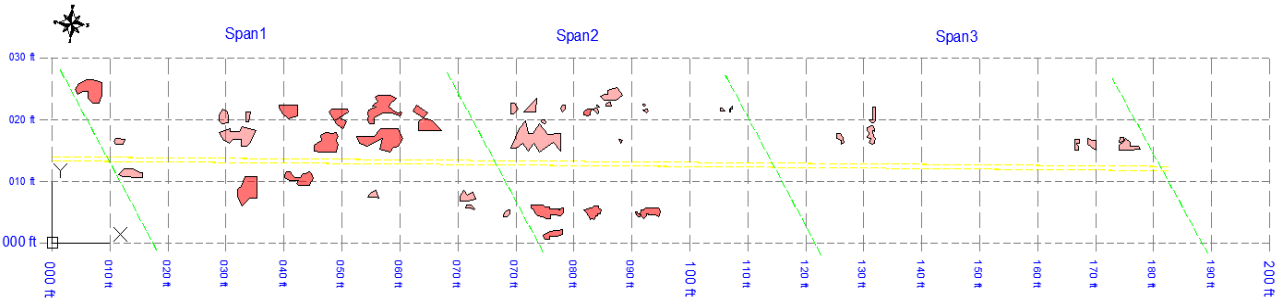

Figure 84 Existing Delamination in the Bridge Deck No. 22383

Therefore, according to the appendix B total area of delamination of bridge No. 22383 is as follow:

Table 6 Area of Delamination of Bridge No. 22383

Bridge No. 22383	Span 1	Span 2	Span 3	Total
Delamination Area (ft^2)	114.25	52.56	12.10	178.91
Span Area (ft^2)	1939.5	1390.2	1914	5307
Ratio (ft^2/ft^2) %	5.9%	3.8%	0.6%	3.4%

5.2.2 Bridge No. 22266

Figure 85 and Figure 86 indicate the absence of any existing delamination in bridge No. 22266. However, there is a lack of information in the shadowed areas. Ground Penetrating Radar (GPR) can provide more precise details regarding delamination depth.

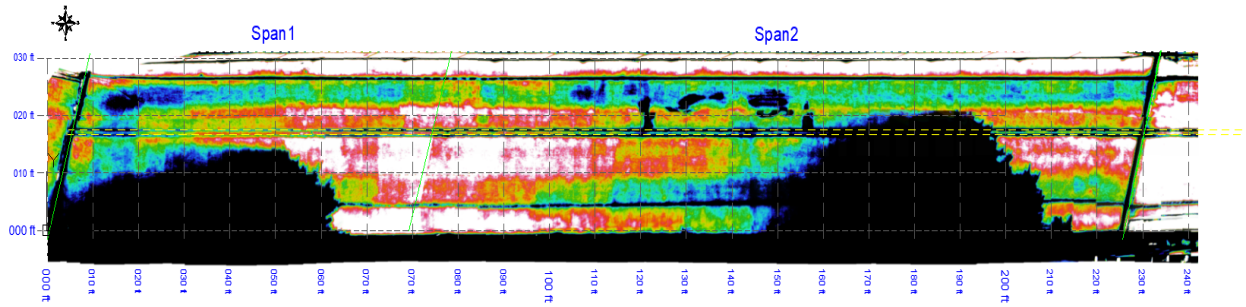

Figure 85 No Delamination Found in The IRT Image Of Bridge Deck No. 22266

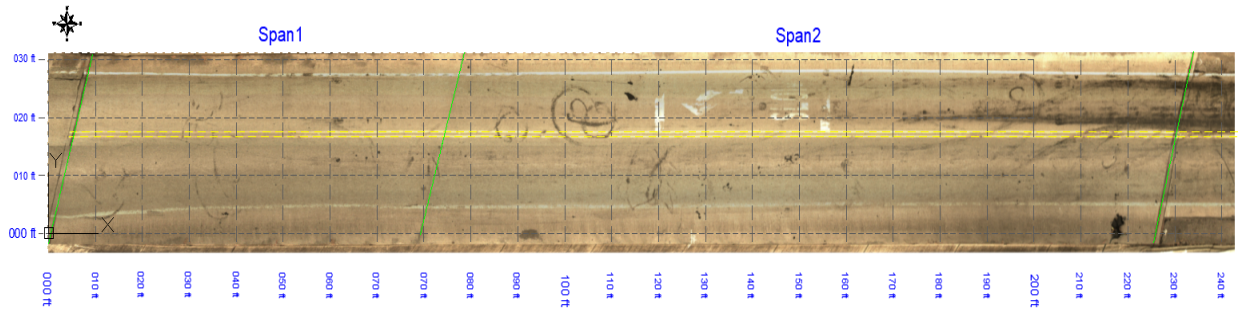

Figure 86 No Delamination Found in the Visual Image of Bridge Deck No. 22266

Therefore, delamination of bridge No. 22266 is as follow:

Table 7 Area of Delamination of Bridge No. 22266

Bridge No. 22266	Span 1	Span 2	Span 3	Total
Delamination Area (ft^2)	0	0	0	0
Span Area (ft^2)	1939.5	1390.2	1914	5307
Ratio (ft^2/ft^2) %	0%	0%	0%	0%

The chain drag survey also confirms no delamination is in bridge deck No. 22266.

5.2.3 Bridge No. 22387

Figure 87 to Figure 89 show existing delamination of bridge No. 22387. The light red hatches can be deep delamination (to top of steel) and dark reds can be shallow. Ground Penetrating Radar (GPR) or can provide more accurate information about delamination depth.

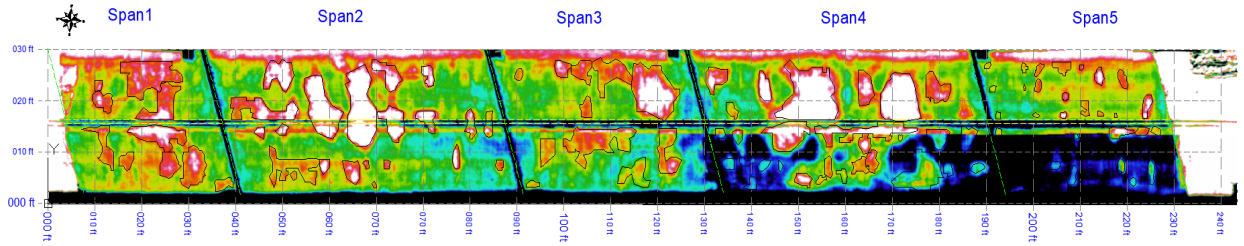

Figure 87 Existing Delamination in the IRT Image of Bridge Deck No. 22387

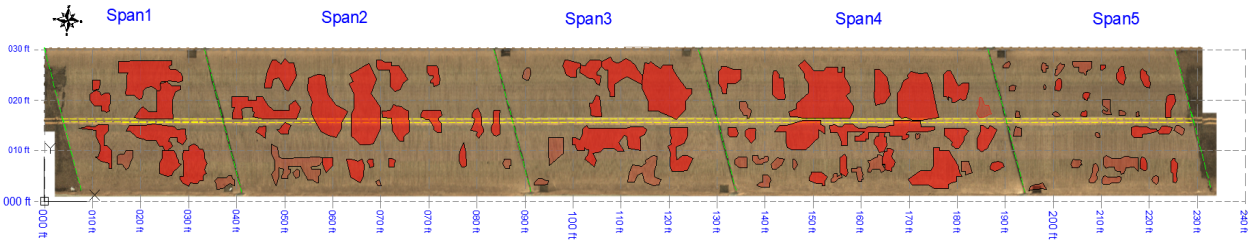

Figure 88 Existing Delamination in the Visual Image of Bridge Deck No. 22387

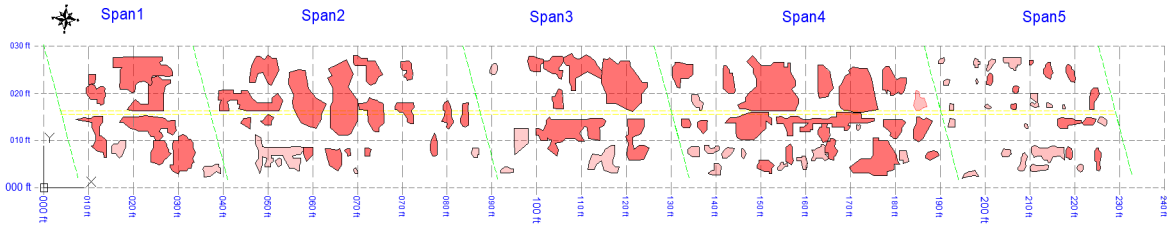

Figure 89 Existing Delamination in the Bridge Deck No. 22387

According to the appendix B total area of delamination of bridge deck No. 22387 is as follow:

Table 8 Area of Delamination of Bridge Deck No. 22387

Bridge No. 22387	Span 1	Span 2	Span 3	Span 4	Span 5	Total
Delamination Area (ft^2)	226.18	350.67	266.07	478.47	105.26	1426.65
Span Area (ft^2)	943.9	1695.6	1198.5	1712.6	1105.9	6669
Ratio (ft^2/ft^2) %	24.0%	20.7%	22.2%	27.9%	9.5%	21.4%

5.3 Bridge No. 22451

Figure 90 to Figure 92 show existing delamination of bridge No. 22451. The light red hatches can be deep delamination (to top of steel) and dark reds can be shallow. Ground Penetrating Radar (GPR) or can provide more accurate information about delamination depth.

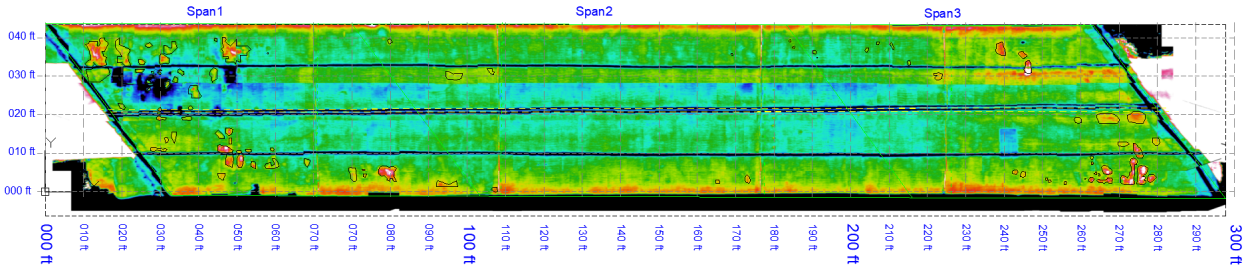

Figure 90 Existing Delamination in the IRT Image of Bridge Deck No. 22451

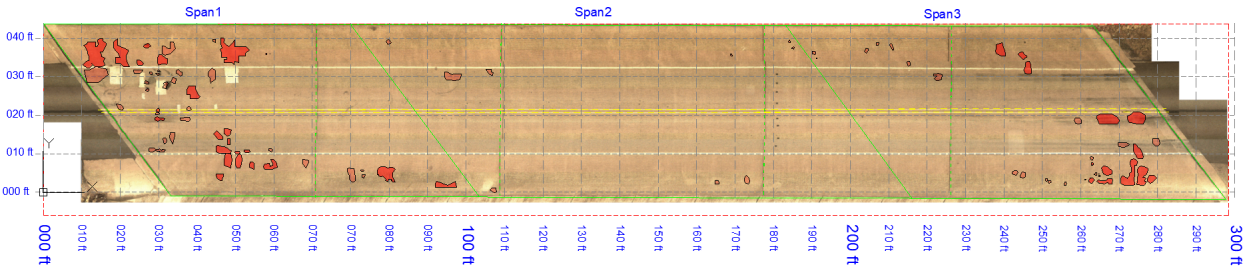

Figure 91 Existing Delamination in The Visual Image of Bridge Deck No. 22451

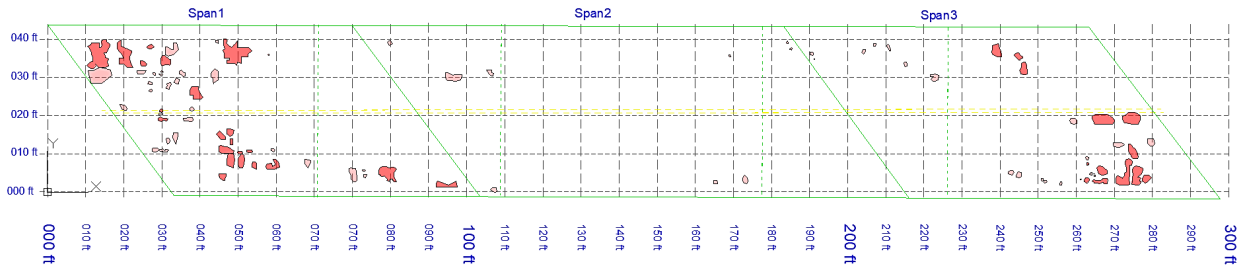

Figure 92 Existing Delamination in the Bridge Deck No. 22451

According to the appendix B total area of delamination of bridge No. 22451 is as follow:

Table 9 Area of Delamination of Bridge Deck No. 22451

Bridge No. 22451	Span 1	Span 2	Span 3	Total
Delamination Area (ft^2)	204.57	14.97	102.60	322.13
Span Area (ft^2)	3579.8	5041.0	3638.6	12294.8
Ratio (ft^2/ft^2) %	5.7%	0.3%	2.8%	2.6%

5.4 Ground Penetrating Radar (GPR) Data Analysis

As mentioned previously, the technique utilizes the electromagnetic spectrum in the microwave range, specifically between 10 MHz and 2.6 GHz, to generate images of the subsurface. These signals are transmitted into the ground and reflect off subsurface structures based on their electrical permittivity. A receiving antenna captures variations in the return signals, which the GPR (Ground Penetrating Radar) device uses to create images. These images generally indicate changes in electrical properties. GPR signals are effective for detecting a wide range of items, particularly when there is a significant difference in the electromagnetic properties of the target and the surrounding material. GPR devices can be used to identify corrosion, moisture, debonding, voids, and delamination. The following are the GPR results for the bridges investigated.

5.4.1 Bridge No. 22383

Figure 93 shows top of steel irregularity (2 to 4 in) in the deck of bridge No. 22383.

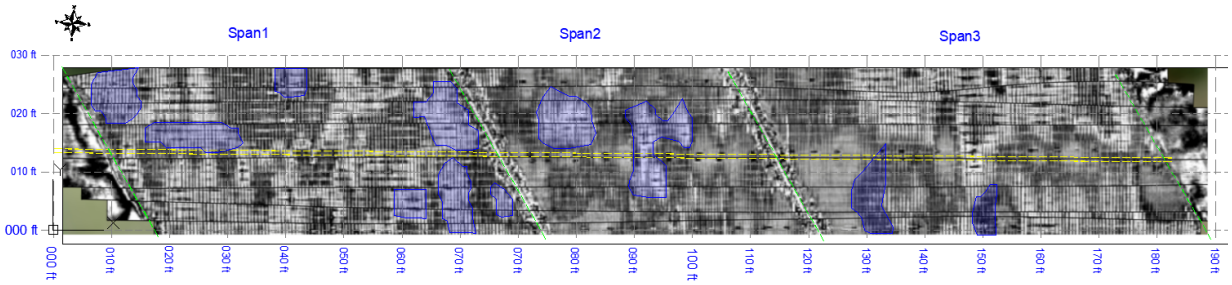

Figure 93 Irregularity in the GPR Top Steel Map of Bridge Deck No. 22383

In Figure 94, overlapping red and blue areas indicate shallow delamination areas. The red hatches are shallow delamination detected by IRT testing.

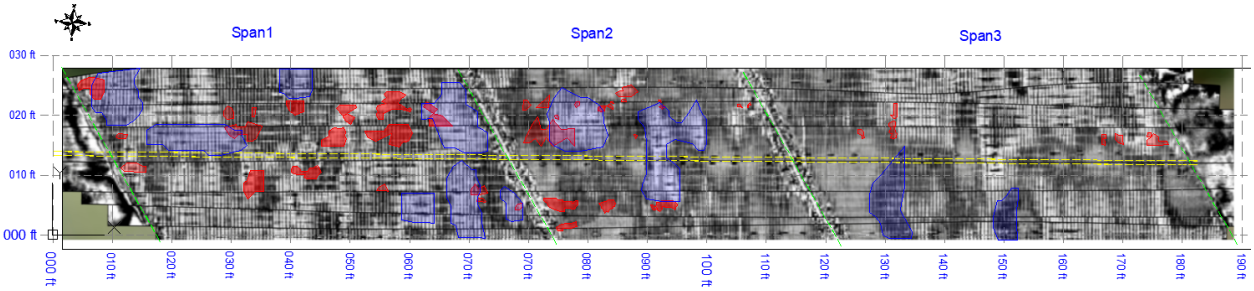

Figure 94 Existing Shallow Delamination in the GPR Map and IRT Detection of Bridge Deck No. 22387

5.4.2 Bridge No. 22266

Figure 95 shows there is no top of steel irregularity (2 to 4 in) in the deck of bridge No. 22266.

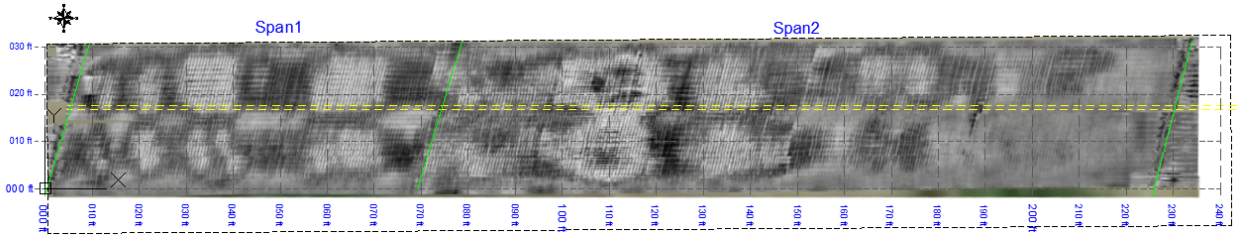

Figure 95 No Irregularity in the GPR Top-Steel Map of Bridge Deck No. 22383

5.4.3 Bridge No. 22387

Figure 96 shows top of steel irregularity (2 to 4 in) in the deck of bridge No. 22387.

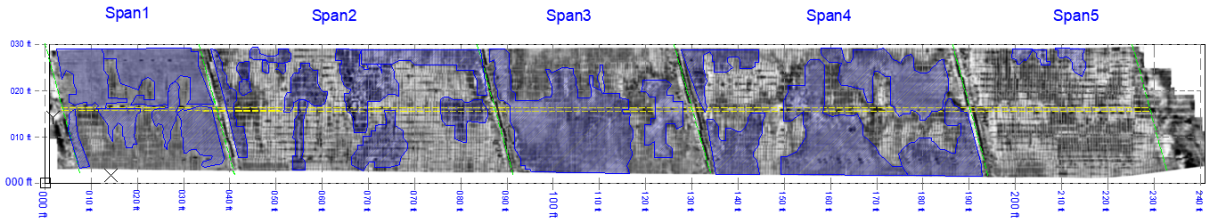

Figure 96 Irregularity in the GPR Top-Steel Map of Bridge Deck No. 22387

In Figure 97, overlapping red and blue areas indicate shallow delamination areas. The red hatches are delamination detected by IRT.

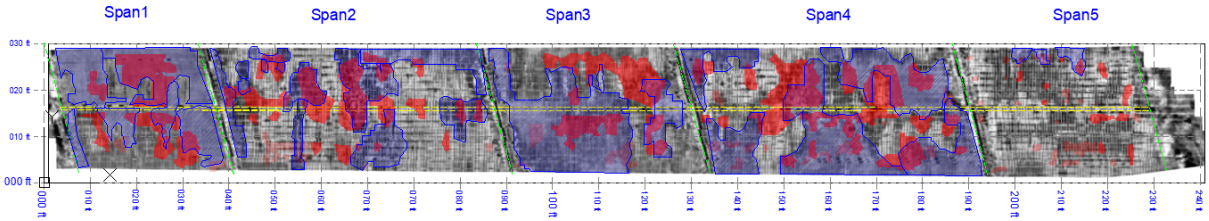

Figure 97 Existing Shallow Delamination in The GPR Map and IRT Detection of Bridge Deck No. 22387

5.4.4 Bridge No. 22451

Figure 98 shows top of steel irregularity (2 to 4 in) in the deck of bridge No. 22451.

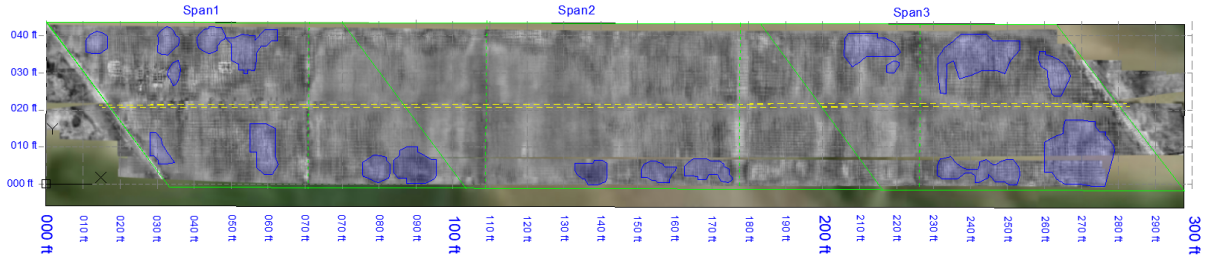

Figure 98 Irregularity in the GPR Top-Steel Map of Bridge Deck No. 22451

In Figure 99, overlapping red and blue areas indicate shallow delamination areas. The red hatches are delamination detected by IRT.

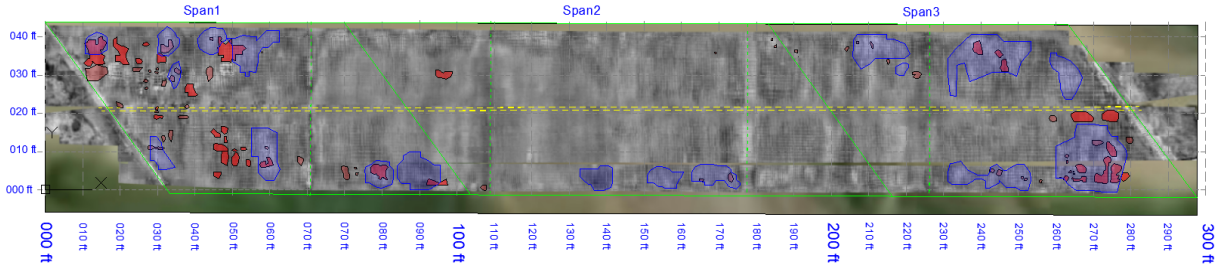

Figure 99 Existing Shallow Delamination in The GPR Map and IRT Detection Bridge Deck No. 22451

6 Comparison of laboratory and field data

The comparison between laboratory and field data in NDE of bridge decks highlights the importance of integrating findings from both environments to enhance the reliability, accuracy, and practical applicability of NDE methods. Field conditions introduce complexities that must be considered to effectively implement laboratory-developed techniques, underscoring the need for ongoing research, adaptation, and validation of NDE technologies in real-world settings.

In our study, we fabricated two concrete specimens in the laboratory to simulate conditions found in bridge decks, with the objective of assessing the efficacy of various non-destructive testing (NDT) techniques. These specimens were designed to mimic common defects found in bridge decks, such as delamination and voids, which can compromise structural integrity and longevity.

The dimensions and intended testing purposes of each specimen are as follows:

- **Specimen for Delamination Detection:**

This 60×60×10cm specimen (Figure 100) was specifically designed to study the detection capabilities of NDT methods for delamination defects within concrete. Delamination is a horizontal crack or separation within the concrete, often caused by corrosion of reinforcement, thermal stresses, or fatigue. These defects are critical as they can reduce the load-carrying capacity of the bridge deck.

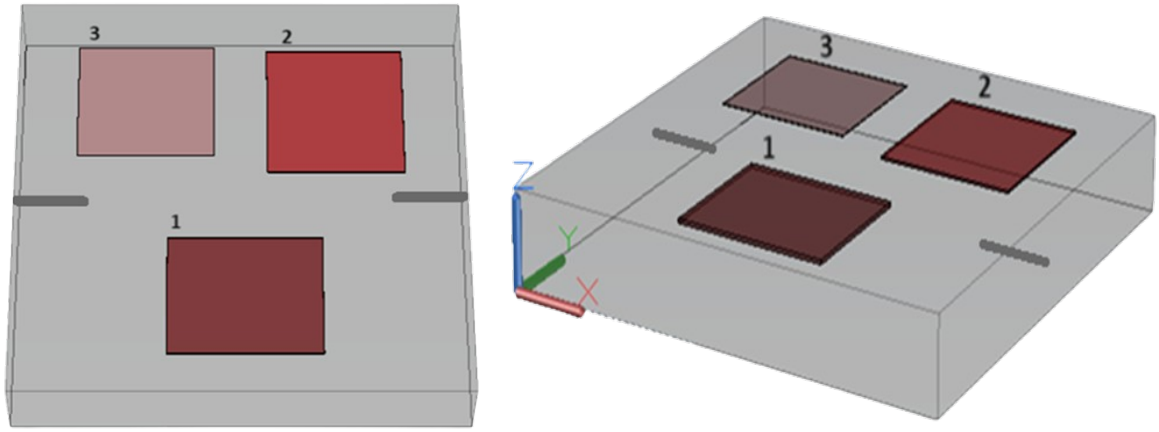

Figure 100 Schematic Views of the Specimen No.1 (60×60×10cm) with Embedded Delamination Defects

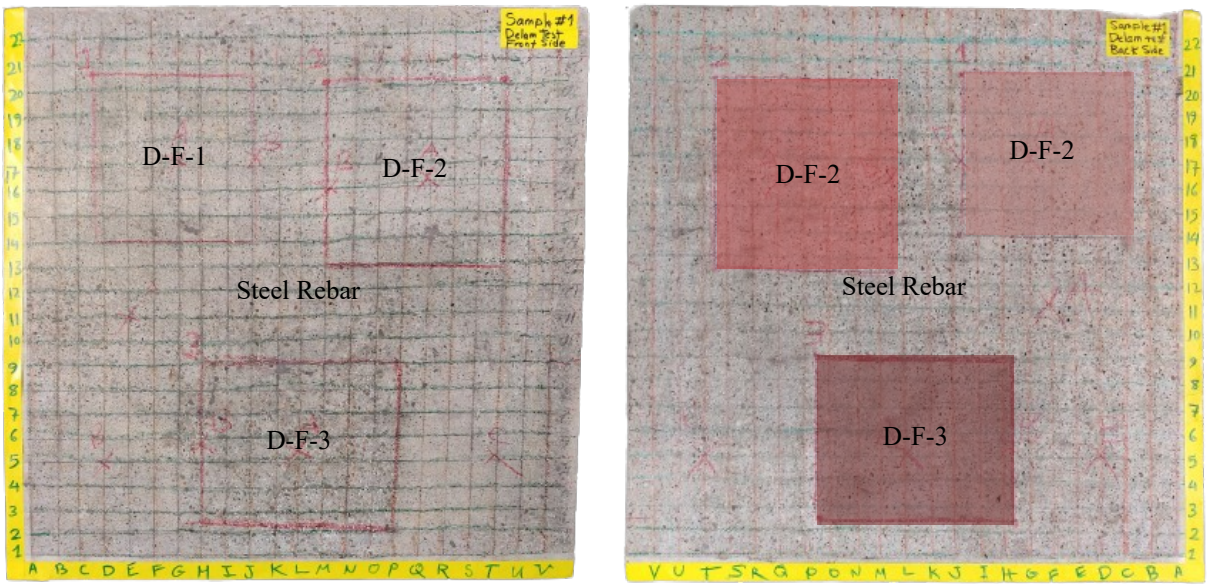

Sample No.1 Front Side ***Sample No.1 Back Side***

Figure 101 Front and Back Side Views of The Delamination Specimen

The artificial delamination defects were located at three separate positions, as illustrated in Figure 100 and Figure 100. These defects, which varied in thickness - 0.7 mm, 2.5 mm, and 4.5 mm – were created using folded sheets to simulate real-world defects (Figure 102).

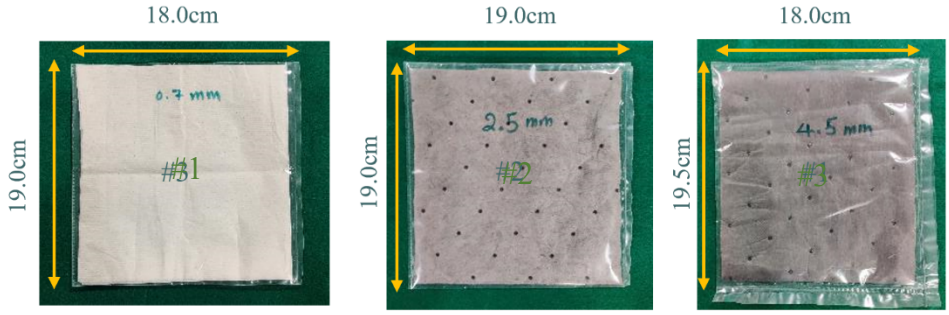

Figure 102 Artificial Delamination Defects

The dimensions and depths of delamination defects are shown in Table 10.

Table 10- Delamination Dimensions-Specimen No.1

Defect No.	Sizes (mm × mm × mm)	Intended Top Concrete Cover /Depth (cm)	Defect No.	Sizes (mm × mm × mm)	Intended Top Concrete Cover /Depth (cm)
D-F-1	180 × 190 × 0.7	1	D-B-1	180 × 190 × 0.7	9
D-F-2	190 × 190 × 2.5	1	D-B-2	190 × 190 × 2.5	9
D-F-3	180 × 19.5 × 4.5	1	D-B-3	180 × 19.5 × 4.5	9

- **Specimen for Void Detection:**

The larger depth of this 60×60×21cm specimen aims to challenge the depth penetration capabilities of NDT methods in locating voids within concrete structures. Voids are air pockets or hollow spaces that occur during the pouring of concrete, potentially leading to reduced structural integrity and durability.

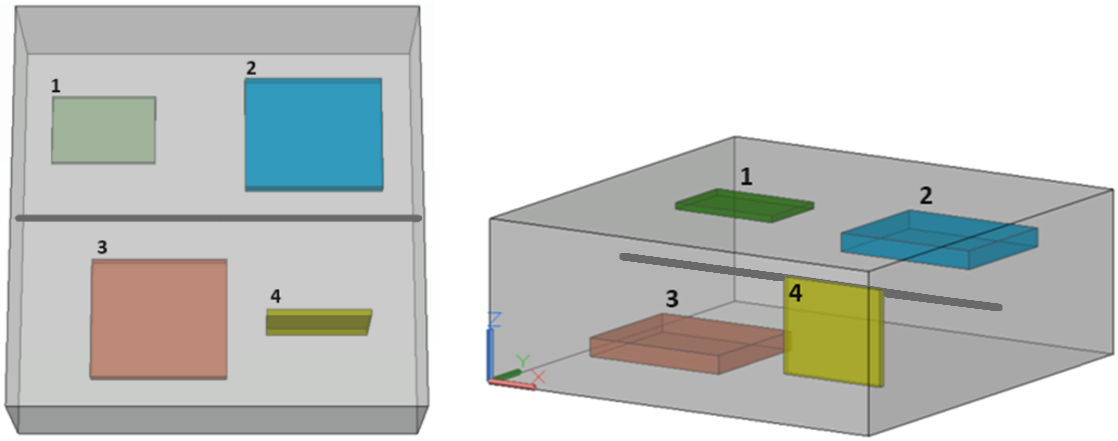

Figure 103 Schematic Views of the Specimen No.2 (60×60×21cm) with Embedded Void Defects

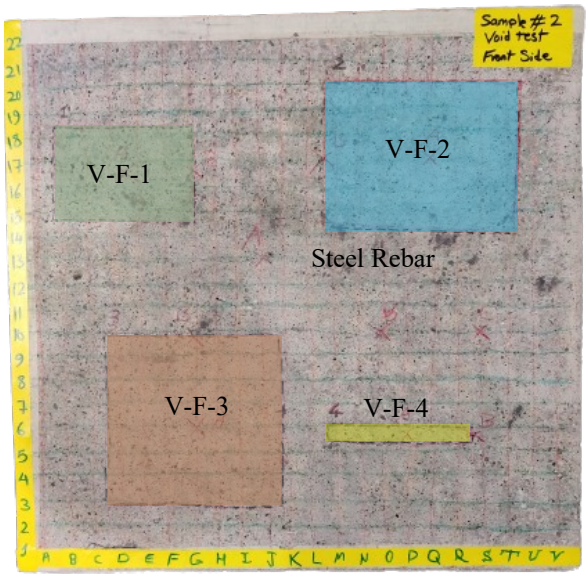

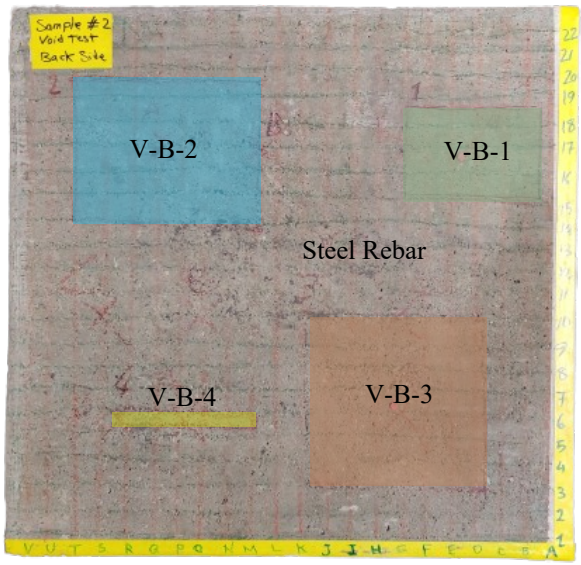

Sample No.2 front side ***Sample No.2 back side***

Figure 104 Front and Back Side Views of the Void Specimen

The artificial void defects were located at four separate positions, as illustrated in Figure 103 and Figure 104. These defects which varied in thickness between 0.9 mm (about 0.04 in) and 25 mm (about 0.98 in) were created using foam to simulate real-world defects. The dimensions and depths of voids are shown in Table 11.

Table 11 Voids Dimensions-Specimen No.2

Defect No.	Sizes (mm × mm × mm)	Intended Top Concrete Cover /Depth (cm)	Defect No.	Sizes (mm × mm × mm)	Intended Top Concrete Cover /Depth (cm)
V-F-1	100 × 150 × 9	4	V-B-1	100 × 150 × 9	17.1
V-F-2	200 × 165 × 25	4	V-B-2	200 × 165 × 25	15.5
V-F-3	200 × 175 × 25	17	V-B-3	200 × 175 × 25	2.5
V-F-4	9 × 130 × 150	5.2	V-B-4	9 × 130 × 150	3.8

In the following section, the comparison of laboratory and field data of the following techniques is discussed.

6.1 Infrared Thermography (IRT) Test

IRT works by detecting infrared radiation emitted from the surface of materials, which can be used to infer temperature variations. These temperature variations can indicate the presence of various deficiencies within concrete structures. Here's an overview of common types of IRT deficiencies and

their typical signatures in concrete:

- **Voids and Hollows**

Voids and hollows can affect the thermal properties of concrete. They may appear as anomalies in the thermal image, with the specific appearance depending on their size, depth, and the temperature difference between the voids and the solid concrete.

- **Delamination**

Separation of subsurface and/or surface concrete layers is usually caused by corrosion of reinforcement steel or inadequate construction. Temperature differentials observed by IRT locate subsurface occurrences. Like voids and hollows, delamination defects in the concrete can trap air or moisture, leading to differences in thermal conductivity and capacity. These areas may appear cooler or warmer depending on the surrounding conditions and the time of day the thermography is conducted. Typically, delaminated areas are seen as irregular, often somewhat circular, patterns on the thermal image (Figure 105).

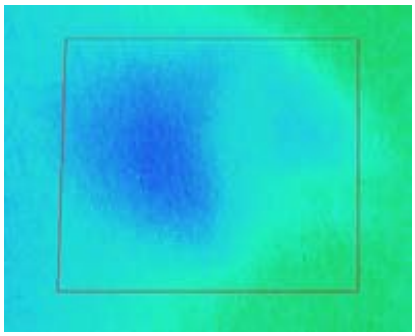

Figure 105 Delaminated Areas in IRT Images [1]

6.1.1 IRT Laboratory Results

This experiment aimed to assess the effectiveness of Infrared Thermography (IRT) in detecting voids and delamination with varying thicknesses and depth within a concrete sample. The focus was on understanding how well IRT can identify defects in different depths and how different thicknesses of defects impact the thermal imaging results. For our laboratory tests, two IR cameras were employed to capture the thermal profiles of the concrete specimens. Each camera, with its specifications, contributed to a comprehensive evaluation of the specimens' conditions.

- **Camera #1: FLIR E54-24 º**

The first camera used in our IRT tests was the FLIR E54-24 º (Figure 106), known for its high-resolution imaging and sensitivity. The specifications of this camera are as follows:

- IR Resolution: 320×240 Pixels - This high resolution allows for detailed thermal images,

enabling precise identification of areas with potential defects.

- Image Frequency: 30 Hz - The high image capture rate ensures smooth thermal video capture, useful for real-time monitoring and analysis.
- Thermal Sensitivity: <40 mK @ 30°C (86°F) - With this level of sensitivity, the camera can detect very small differences in temperature, which is crucial for identifying subtle thermal patterns indicative of delamination or voids.

- **Camera #2: Testo 875i**

The second camera, the Testo 875i (Figure 106), complements the first by offering robust thermal imaging capabilities with slightly different specifications:

- IR Resolution: 160×120 pixels - While this resolution is lower than that of the FLIR E54-24, it remains effective for identifying significant thermal anomalies across the concrete specimens.
- Image Frequency: 30 Hz - Similar to the FLIR camera, this frequency supports the capture of fluid thermal videos, aiding in dynamic analysis.
- Thermal Sensitivity: < 50 mK @ 30°C (86°F) - This sensitivity level, though slightly lower than that of the FLIR E54-24°, still permits the detection of minor temperature variations that could indicate the presence of defects.

Testo 875 ***FLIR E54-24º***

Figure 106 Testo 875 High-Resolution Thermal Imager

By employing both cameras, we ensured that our IRT test was both thorough and versatile, maximizing our ability to detect a wide range of defect types and sizes within the concrete specimens. Figure 107 shows the experimental setup for the Infrared Thermography (IRT) test of the concrete specimens. During the IRT test, the concrete specimens are heated by infrared lamps. These lamps are

used to uniformly heat the surface of the concrete specimens, which is a standard procedure in active IRT testing. The camera records changes in the thermal profiles. These changes can reveal hidden features within the concrete due to the different heat transfer properties of sound concrete versus defects. Delamination defects, for instance, might heat up or cool down faster than solid concrete because of the air gap that provides thermal insulation, leading to a contrasting thermal pattern on the image. The IR camera's role is to capture these patterns. The camera's specifications, such as its resolution and thermal sensitivity, will determine the clarity and detail of the thermal images and, thus, the effectiveness in identifying defects. By analyzing the differences in heat signatures over time, researchers can identify and map the locations of potential defects within the concrete. This information is critical for assessing the health of concrete structures, such as bridge decks, and can inform maintenance and repair strategies. This setup provides a controlled environment to simulate how IRT would be conducted in the field, allowing for a detailed study of the method's effectiveness in a laboratory setting. The controlled conditions also allow for the calibration of the IR cameras and refinement of the IRT technique for field use.

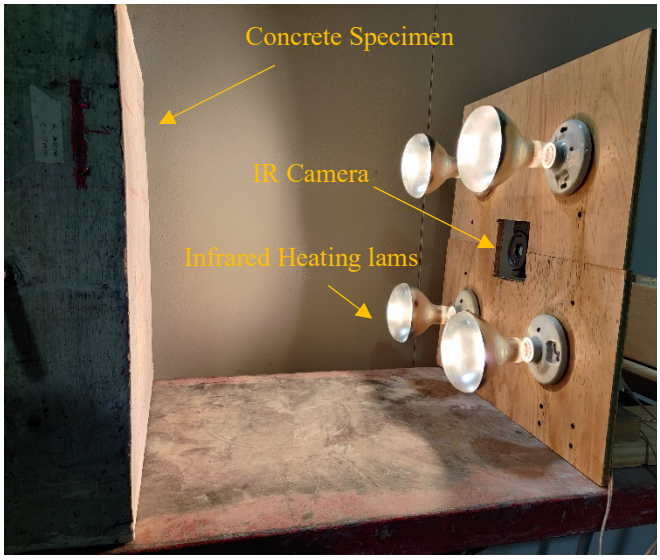

Figure 107 Setup of the Laboratory IRT Test

The front-side image in Figure 108 taken by camera #1 shows clear, well-defined concentric heat patterns that indicate the presence of delamination areas labeled D-F-1, D-F-2, and D-F-3. The distinct rings with central hotspots correspond to areas where the delamination defects exist, and they alter thermal conductivity. The variation in color intensity within each delaminated area can be used to estimate the relative thickness of the delamination defects or the delamination distance to the surface. Brighter or hotter areas suggest thinner/further away sections, while cooler colors suggest thicker/

closer sections. In Figure 108.a and Figure 108.b defects D-F-1, D-F-2, and D-F-3 are 0.7 mm, 2.5 mm, and 4.5 mm thick. Although camera #2 has a lower resolution, which is evident in the less detailed thermal images, it shows better the shape of defects.

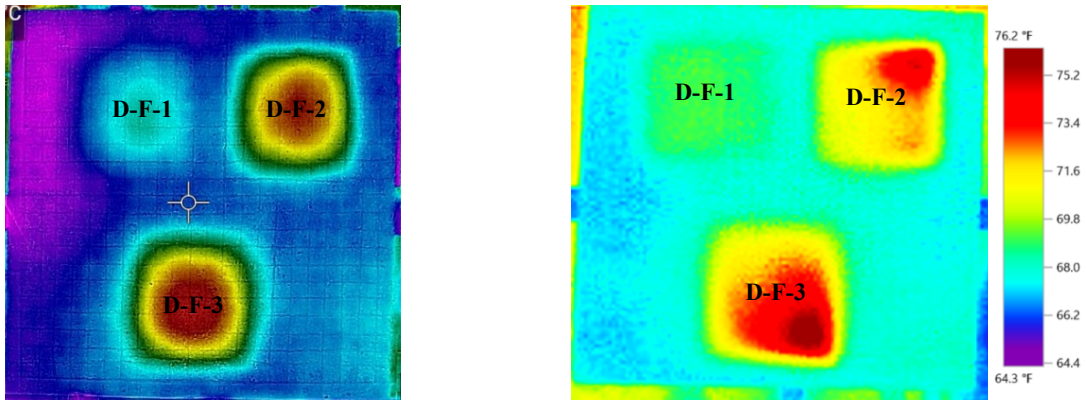

a) Camera #1 *b) Camera #2*

Figure 108 Results of the IRT Test in the Front Side of Specimen No.1 (Delamination)

The back-side image in Figure 109 is quite uniform and does not show the defects clearly by both cameras, confirming that the increased depth of the defects from this side makes it difficult to locate deep delamination defects.

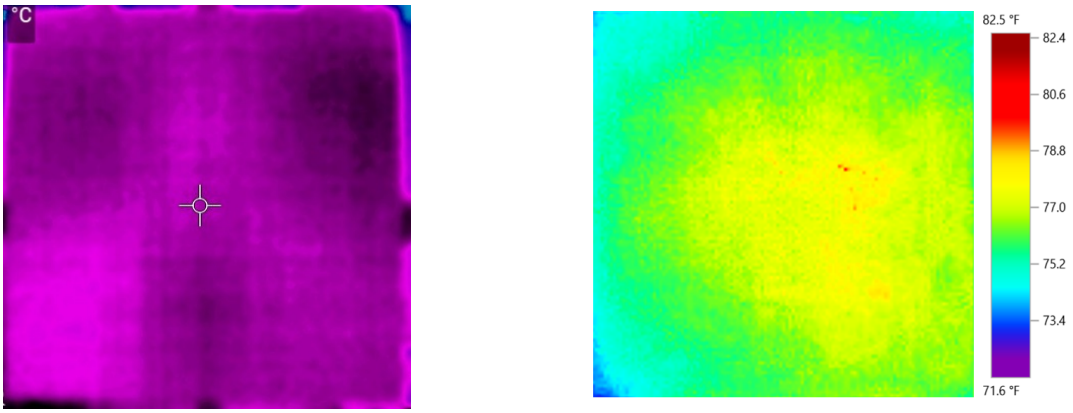

a) *Camera #1* b) *Camera #2*

Figure 109 Results of the IRT Test in the Back Side of Specimen No.1 (Delamination)

In Figure 110, the image from camera #1 presents clearly defined areas of interest with high contrast between the colors, indicating temperature variations across the surface. The void areas marked as V-D-1 (thickness: 9mm) and V-D-2 (thickness: 25mm) show a strong, centralized heat signature surrounded by a cooler area, suggesting the presence of voids close to the surface (4cm), where the lack of material leads to less heat being retained. The dashed outlines indicate the identified locations of potential voids. V-D-3 and V-D-4, which are marked by cooler colors, suggest these voids are deeper, V-D-3 (depth: 17cm), and smaller (V-D-4) as they do not retain as much heat as V-D-1

and V-D-2. The image from camera #2 produces a more uniform and less contrasted image, with the marked areas appearing as diffused warm spots on a broadly hot background. The distinctions between the areas of interest and the surrounding material are less pronounced, making it harder to accurately determine the size and depth of the voids. V-D-1 and V-D-2 are still identifiable as warmer areas, but the resolution and thermal sensitivity limitations of this camera lead to a less detailed depiction.

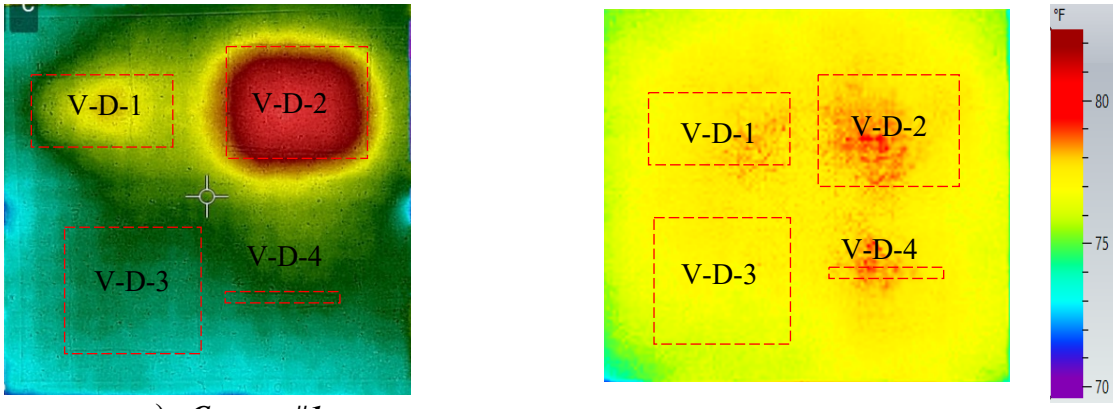

a) ***Camera #1*** b) ***Camera #2***

Figure 110 Results of the IRT Test in the Front Side of Specimen No.2 (Voids)

Therefore, while both cameras are capable of identifying potential voids in the concrete specimen, Camera #1 shows a greater capacity for detail and might be more suited for precise diagnostics. In Figure 110, the image from camera #1 seems to provide a more precise and localized indication of the void, V-D-3, suggesting a superior ability to detect and detail the extent of the voids from the back side of the specimen at the dept of 2.5cm. Camera #2, while still identifying the void, gives a more generalized and less detailed representation.

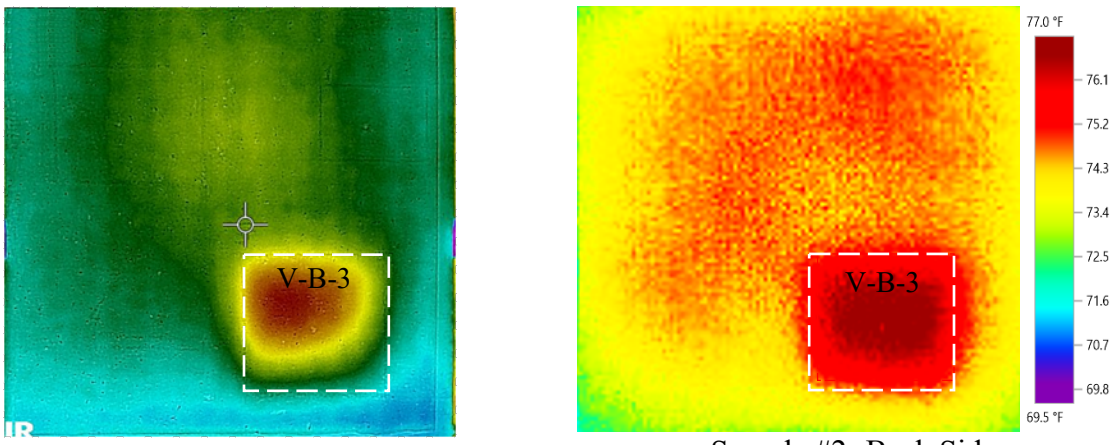

Sample #2- Back Side Sample #2- Back Side

Figure 111- Results of the IRT Test in the Back Side of Specimen No.2 (Voids)

In conclusion, according to Table 12, Infrared Thermography (IRT) proves to be an effective non-destructive testing method for identifying delamination within concrete when these defects are

relatively shallow (up to 1 cm deep) and sufficiently thick (over 0.7 mm). The technology's efficiency is contingent upon the defect's proximity to the surface and its physical characteristics; thicker and shallower delamination presents a stronger thermal contrast, leading to more accurate detection. For deeper delamination (9 cm), the effectiveness of IRT significantly decreases, highlighting the limitations of this method for detecting defects that are far from the surface.

Table 12 Efficiency of IRT in Delamination Detection

Defect No.	Result	Thickness (mm)	Depth (cm)	IRT Efficiency	Defect No.	Result	Thickness (mm)	Depth (cm)	IRT Efficiency
D-F-1	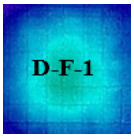	0.7	1	Moderate	D-B-1	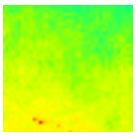	0.7	9	Poor
D-F-2	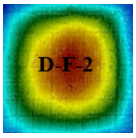	2.5	1	Strong	D-B-2	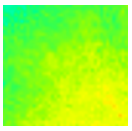	2.5	9	Poor
D-F-3	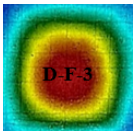	4.5	1	Strong	D-B-3	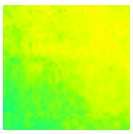	4.5	9	Poor

These findings suggest that IRT is most suitable for applications where delamination is expected to be near the surface of the structure. As part of a comprehensive structural assessment, IRT should be used in conjunction with other methods, especially when dealing with deeper elements of a structure, to ensure all potential defects are identified and appropriately addressed.

Table 13 shows that Infrared Thermography is more effective at detecting voids thicker and closer to the concrete specimen's surface. There is a clear trend showing that as voids become deeper, IRT's efficiency in detecting them decreases. This is likely because the fact that thermal energy dissipates as it travels through a medium, and the deeper a void is, the less pronounced the thermal signature will be on the surface. However, even at significant depths, thick voids (25 mm) can still be detected, though with reduced clarity. The absence of data for the efficiency rating in the table makes it challenging to quantitatively assess how well IRT performs under these conditions. Nevertheless, qualitatively, the thermal images show that IRT has limitations when voids are deep and possibly when they are of lesser thickness. For effective bridge deck evaluation, IRT is recommended to be

used with other NDT methods to ensure accurate detection of voids at various depths and thicknesses. This multi-method approach can compensate for the limitations of IRT and provide a more comprehensive assessment of the concrete's condition.

Table 13- Efficiency of IRT in Void Detection

Defect No.	Result	Thickness (mm)	Depth (cm)	IRT Efficiency	Defect No.	Result	Thickness (mm)	Depth (cm)	IRT Efficiency
V-F-1	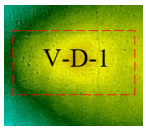	9	4	Moderate	V-B-1	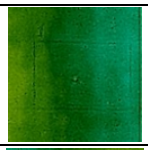	9	17.1	Poor
V-F-2	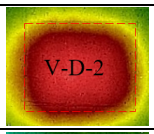	25	4	Strong	V-B-2		25	15.5	Poor
V-F-3		25	17	Poor	V-B-3	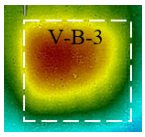	25	2.5	Strong
V-F-4	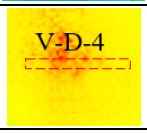	-	5.2	Moderate	V-B-4	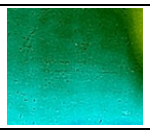	-	3.8	Poor

6.1.2 IRT Field Results

In this report bridge No. 22383 is selected for comparing the efficiency of different techniques. The reddish hatched areas in both images of Figure 112 show existing delamination and areas surrounded with blue line shows sound test results. The dash-line boxes shown in Figure 112, indicate the IRT test can detect almost all the defects identified in the sound tests marked with blue lines. The location of the cracks on the bridge's surface does not nearly match the location of the defects identified in the IRT and sound tests. Also, some reddish areas in the above image are not included as defects in the subcontractor's reports. We discuss them in the discussion part 6.5.

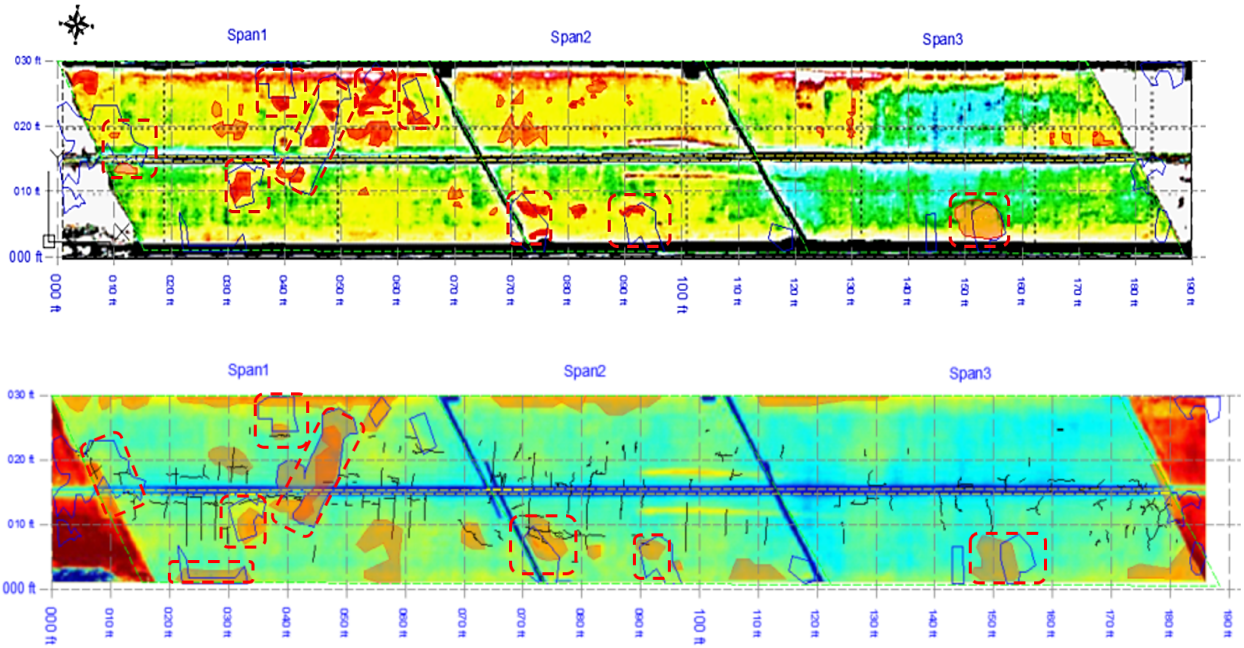

Figure 112 IRT Contour Maps of Bridge Deck No. 22383 [1], [2]

6.2 Ground Penetrating Radar (GPR) Test

A Ground Penetrating Radar (GPR) device measures wave velocity by emitting electromagnetic waves into the ground and analyzing the reflected signals, which vary based on the dielectric properties of the materials encountered. GPR technique utilizes electromagnetic radiation to detect and map the presence of objects, changes in material properties, voids, cracks, and other features within concrete. The wave velocity (v) of a GPR signal in a medium is related to the relative permittivity (ε_r) of the material it is passing through by the following formula:

$$v = \frac{c}{\sqrt{\varepsilon_r}}$$

where:

- v is the velocity of the electromagnetic wave in the material,
- c is the speed of light in vacuum (approximately 3×10^8 meters per second), and
- ε_r is the relative permittivity of the material.

On the one hand, understanding material characteristics is fundamental for professionals working with Ground Penetrating Radar GPR. Variations in dielectric permittivity significantly impact the accuracy and interpretation of GPR data, playing a crucial role in the success and efficacy of subsurface investigations provides a list of various materials along with their corresponding dielectric

properties [3].

Table 14 Dielectric Properties of Various Materials (Cassidy, 2008)

Material	Relative Permittivity ε_r	Electrical Conductivity σ (mS/m)	Propagation Velocity u (m/ns)
Air	1	0	0.3
Concrete (dry)	4-10	1-10	0.09-0.15
Concrete (wet)	10-20	10-100	0.07-0.09
Fresh water	81	0.1-10	0.03
Granite (dry)	5-8	0.001-0.00001	0.11-0.13
Granite (wet)	5-15	1-10	0.08-0.13
Limestone (dry)	4-8	0.001-0.0000001	0.11-0.15
Limestone (wet)	6-15	10-100	0.08-0.12
Sand (dry)	4-6	0.001-1	0.12-0.15
Sand (wet)	10-30	0.1-10	0.05-0.09
Soil (average)	16	5	0.08
Steel	1	∞	~ 0

These properties include the relative permittivity (ε_r), the electrical conductivity (σ, measured in millisiemens per meter), and the propagation velocity (u, measured in meters per nanosecond). The relative permittivity measures how much the electric field is reduced inside the material compared to a vacuum. Electrical conductivity indicates how well the material can conduct electricity, with higher values indicating better conductivity. The propagation velocity refers to the speed at which electromagnetic waves, such as radar, can travel through the material. Notably, the values change when the material is wet, generally resulting in higher permittivity and conductivity, which can greatly affect the wave propagation speed. These properties are critical in various applications, including Ground Penetrating Radar (GPR) for subsurface investigations, where they influence the reflection, absorption, and transmission of radar waves. It has been observed that concrete possesses a higher dielectric constant (also known as relative permittivity, ε_r) compared to steel or air. In general, moisture, corrosion, delamination, and voids alter the capacity of concrete to store electrical energy by changing its dielectric constant and conductivity, which affects how much and how quickly it can polarize in response to an electric field. When concrete absorbs moisture, it increases its dielectric constant. Water molecules align with the electric field, enhancing the material's ability to store energy. However, excessive moisture can lead to reduced conductivity due to ion migration and electrolytic effects. Corroded reinforcing steel within concrete creates localized areas of higher conductivity. These regions alter the overall conductivity and affect energy storage. Additionally, corrosion

products can occupy voids, changing the dielectric properties. Delaminated concrete layers create interfaces with varying dielectric constants. These interfaces disrupt the uniformity of the material, affecting its overall energy storage capacity. Air voids or gaps reduce the effective dielectric constant. They act as insulators, limiting energy storage. Additionally, voids can trap moisture, further impacting conductivity.

On the other hand, understanding the types of deficiencies and their typical signatures in concrete can help accurately interpret GPR data for structural assessment and maintenance. Here are some common types of GPR deficiencies and their typical signatures in concrete:

- **Voids and Hollows**

Voids or hollows within the concrete will cause strong reflections that can appear as patches of strong amplitudes or hyperbolic patterns (Figure 113) in GPR data if the void/hollow is small or rounded. Drastic dielectric changes appear similarly. The shape and intensity of the reflection can vary depending on the size and depth of the void.

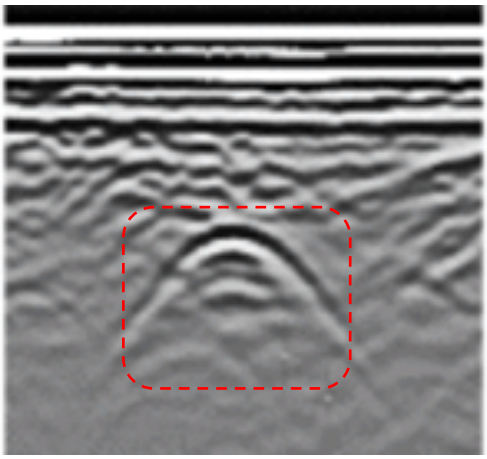

Figure 113 Strong Hyperbola Reflections of Voids or Hollows

- **Delamination**

Delamination within concrete layers causes sudden strong reflections (Figure 114) due to the air gap created by the separation. These are typically identified as continuous, flat-lying reflections parallel to the surface.

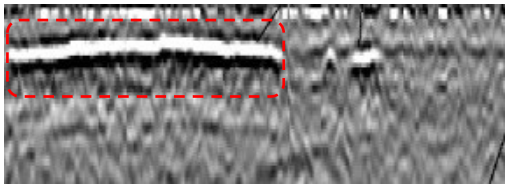

Figure 114 Strong Area Reflections of Delamination

- **Cracks and Fractures**

Cracks can be more challenging to detect depending on their orientation and width. They may appear as discontinuities or irregular patterns in the GPR data, often requiring high-resolution scans for detection.

- **Corrosion of Reinforcement**

While GPR itself cannot directly detect corrosion, the effects of corrosion (such as increased porosity or delamination) can alter the GPR signal indirectly indicating potential corrosion areas. For example, areas with comparatively weak signal responses are indicative of corrosive or moist environments.

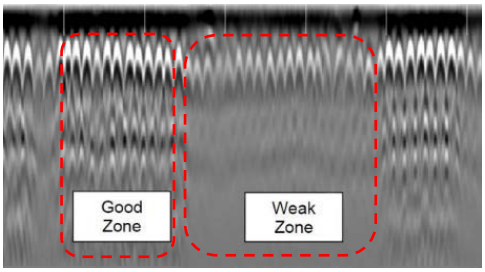

Figure 115 Weak Signal Responses of Corrosive or Moist Environment

- **Moisture Content Variations**

Areas with higher moisture content have different dielectric properties, which can be detected by GPR. Like rebar corrosion but generally to a greater extent. A higher dielectric permittivity hinders the signal, so slower and weaker responses indicate moisture after a stronger surface reflection. These areas may appear as zones of differential reflection amplitude or velocity changes.

- **Rebar and Metallic Objects**

Metallic objects such as rebar, conduits, and utility lines provide strong reflections. They appear as hyperbolic patterns (Figure 113) due to their cylindrical shape, with the apex indicating the position of the object.

- **Concrete Cover Thickness**

The thickness of the concrete cover over reinforcement can be determined by analyzing the time delay between the surface reflection and the reflection from the top of the rebar. The distance between the surface and the rebar can be measured accurately so long as the dielectric constant of the medium stays relatively consistent. Areas with less cover thickness are susceptible to deterioration (Figure 116).

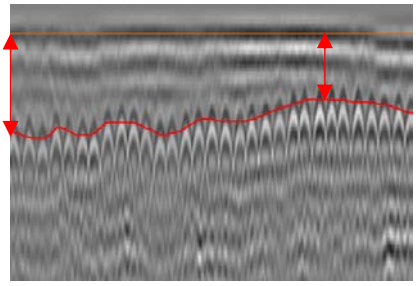

Figure 116 The Distances Between the Surface and the Rebar Indicate the Cover Thickness

Interpreting GPR data involves various formats, each providing unique insights into subsurface features, as illustrated in Figure 117.

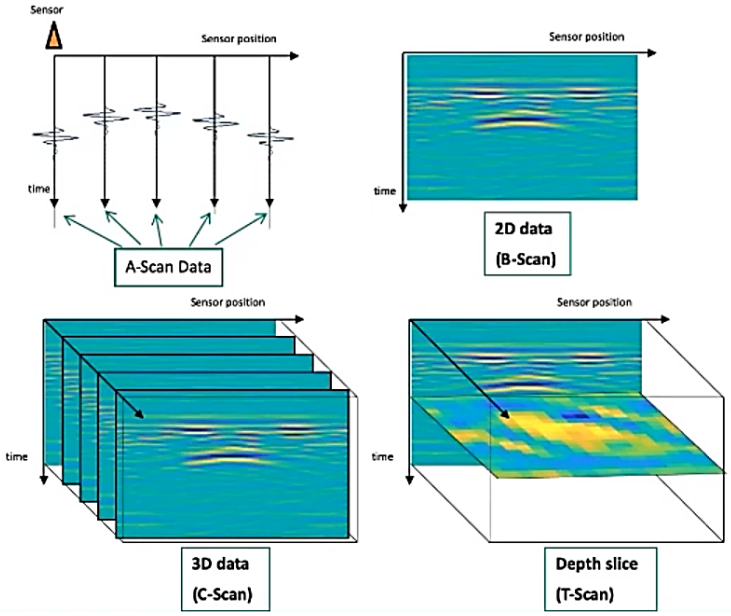

Figure 117 Different Forms of GPR Interpretation [4]

An A-scan in GPR is a fundamental data form that displays signal strength over time at a single point, useful for identifying individual reflectors and their depths [4]. In the context of GPR testing on a concrete specimen, here's what an A-scan can reveal:

Reflection Strength: The amplitude of reflections in the A-scan can help identify the presence of objects within the concrete. A strong reflection might indicate a dense object or a defect boundary, such as a void, a crack, or embedded rebar.

Material Boundaries: Changes in material properties, such as the boundary between different concrete layers or the interface between concrete and air in a void, can be identified. These boundaries cause reflections due to the contrast in electromagnetic properties.

Depth Estimation: By knowing the speed of the electromagnetic waves in the concrete, the time it takes for the radar signal to return can be converted into depth, allowing for an estimation of where

within the concrete a feature is located.

Defect Detection: Any anomalies in the expected pattern of the subsurface, such as cracks, delamination defects, or voids, can be detected. The shape and intensity of the reflections can give clues about the nature of these defects.

A B-scan, created by stacking A-scans along a line, provides a 2D cross-sectional view of the subsurface, revealing layers, interfaces, and buried objects [4]. Here's how B-scan results help in detecting defects in concrete:

Visualization of Defects: B-scans allow for the visualization of the internal structure of the concrete over a scanned area. Defects such as voids, cracks, delamination, and other anomalies are identified as discontinuities or irregular patterns within the consistent background reflection pattern of the concrete.

Depth and Size Estimation: The depth of features within the concrete can be estimated based on the time it takes for the radar waves to return to the surface. This information, along with the horizontal spread of a feature on the scan, helps in estimating the size and orientation of detected defects.

Embedded Object Location: B-scans are effective in locating embedded objects within concrete, such as rebar, conduits, and utility pipes. These objects typically appear as continuous or periodic reflections depending on their orientation and material.

Layer Thickness Measurement: In layered structures, the interfaces between different materials or concrete layers can be clearly seen. This enables measurements of layer thicknesses and identification of potential issues like thinning or uneven layers.

A C-scan, which combines parallel B-scans across an area, offers a 3D plan view of subsurface features, aiding in mapping their extent and distribution.

A T-scan, extracting data at a specific depth from B-scans, yields a focused 2D horizontal slice of the subsurface. The selection of a GPR interpretation format is dependent on the specific application and the information required [4]. Here's how T-scan results are used in detecting defects in concrete:

Defect Mapping: T-scans provide a detailed map of defects such as cracks, voids, and delamination within the concrete. These defects are identified as anomalies in the uniform pattern of the scan, often showing up as irregular shapes or areas with distinct reflectivity characteristics.

Location and Distribution of Embedded Objects: The position of embedded objects like rebar, conduits, and utility pipes can be precisely located. T-scans help in identifying the layout of these objects, assessing their coverage, and detecting potential issues such as clustering or areas lacking

sufficient reinforcement.

Material Uniformity: T-scans can reveal variations in material properties, such as changes in moisture content, concrete density, or the presence of different materials. These variations affect the electromagnetic properties of the scanned area, resulting in detectable patterns on the T-scan image.

Area Coverage: By providing a comprehensive view of the entire scanned area, T-scans allow for the assessment of the extent and distribution of subsurface features across a large section of the concrete specimen. This is particularly useful for planning repairs, renovations, or for quality control in construction.

6.2.1 GPR Laboratory Results

In the course of our investigation, we employed the Proceq GPR GP8000 (Figure 118), a state-of-the-art GPR system, to examine artificial defects within concrete specimens. Our study focused on two specific types of defects: delamination and voids, both of which were intentionally introduced into the specimens to simulate common concrete pathologies. The uniqueness of this application lies in the variance of the defects' characteristics, specifically their thicknesses and depths within the concrete. The Proceq GPR GP8000, renowned for its high-resolution imaging and depth penetration capabilities, was instrumental in detecting these differences. By utilizing its advanced features, we adjusted the radar's settings to optimize the detection of the defects' extents and locations. The process involved meticulously scanning each specimen, with the radar emitting electromagnetic waves that penetrated the concrete. When these waves encountered a defect, their behavior altered, reflecting back to the device. The GPR GP8000's sophisticated software processed these signals, creating detailed images highlighting the defects' presence, thickness, and depth.

For the specimen with delamination, the GPR effectively identified the layered separations, even when these were situated at varying depths. Similarly, in the specimen with voids, the GPR's sensitivity allowed for the precise localization of air gaps, regardless of their size or depth within the concrete. This application of the Proceq GPR GP8000 underscores its value not only as a diagnostic tool but also as a means to accurately assess the integrity of concrete structures, facilitating targeted interventions that address specific defects. The data and insights gained from this exercise have significantly contributed to our understanding of concrete pathology and the efficacy of GPR technology in structural diagnosis.

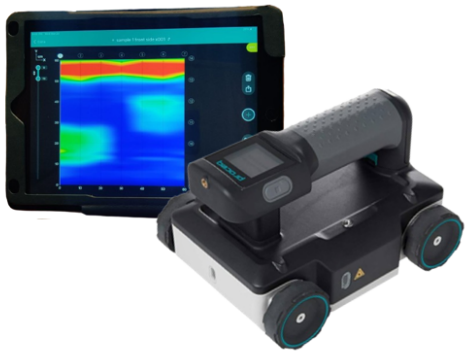

Figure 118 Proceq GPR GP8000

The specifications for the Proceq GP8000 are as follows:

- Probe S/N: PM08-001-0179
- Hardware Version: B0
- Firmware Version: 4.9.1
- Contract Type: Pro 2017
- Contract Validity: Lifetime
- App Version: 5.1.1 (310)
- Software: Proceq GPR App Version 5.1.1

The procedure involved methodically scanning both sides of each previous concrete specimen shown in Figure 100 to Figure 104, structuring the approach into a grid pattern consisting of 7 rows and 7 columns. This meticulous grid approach ensured comprehensive coverage of the specimen's surface, allowing for a detailed subsurface image to be constructed. By moving the device along this grid, we were able to collect consistent and overlapping data points, which contributed to the accuracy of the defect mapping. The resulting scans produced clear imagery of the internal composition of the concrete, revealing the location and depth of embedded rebar, as well as the presence of any defects or inconsistencies within the material. The results of the GPR tests encompassing A-scan, B-scan, and T-Scan analyses for both sides of both specimens are illustrated in Figure 119 to Figure 125. Additionally, 3D visualizations of the detected defects are included within this range of figures. The complete set of GPR data, which includes the B-scan and T-scan images in all depths, can be found in Appendix A, presented from Figure 140 to Figure 152.

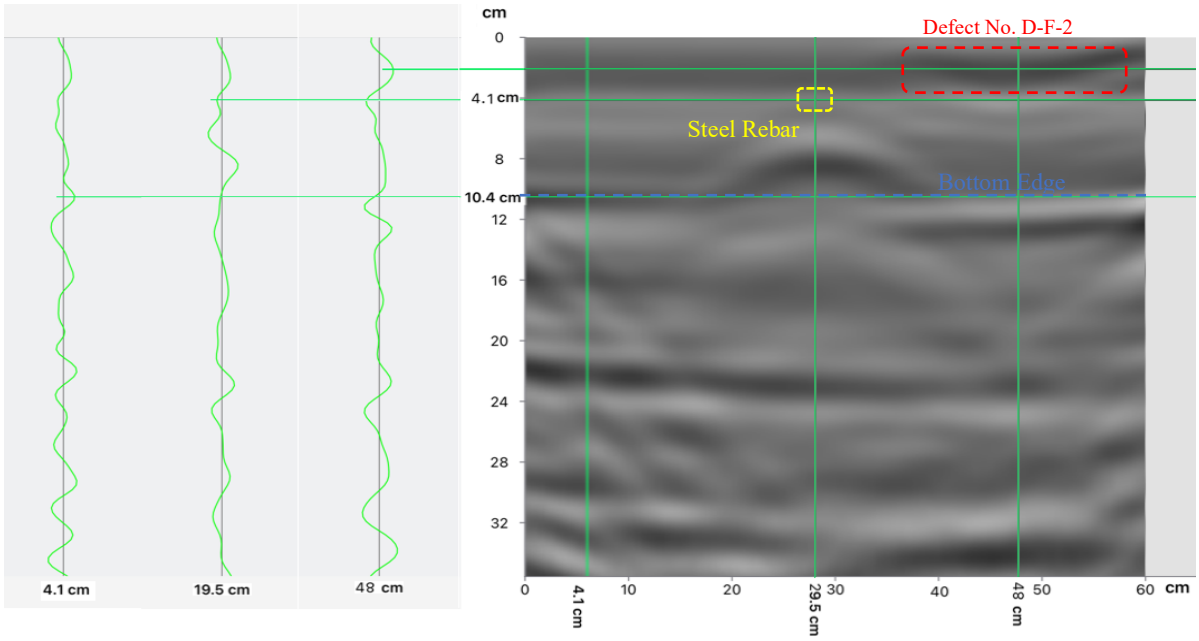

Figure 119 A-Scans and B-Scan of Front Side of Specimen No. 1 (Line 6- Y-Direction Scan)

Figure 119 shows a set of A-Scans and a B-Scan from the GPR survey on the front side of concrete specimen No.1 (delamination sample). On the left image, there are three A-Scan traces displayed as vertical lines with green peaks and troughs, representing the amplitude of the reflected radar signals at specific points (shown in the right image) along the specimen. These traces illustrate the variation in signal reflection over depth at a single location, with the green lines indicating the strength of the reflection where peaks correspond to strong reflectors within the concrete.

On the right image, there is a B-Scan which is a two-dimensional cross-sectional view, combining multiple A-Scans along line No. 1 on the specimen's surface. This view provides a slice through the specimen, showing the depth and position of subsurface features, including steel rebar, delamination defect No. D-F-2, and the specimen's bottom edge. It shows that the depth of the delamination D-F-2, steel rebar, and specimen's downside are respectively 2, 4.1, 10.4 cm.

Figure 119 illustrates full-depth T-Scans from GPR testing on Specimen No. 1, with artificially introduced delamination defects of varying thicknesses, which explains the different colors observed in the scans.

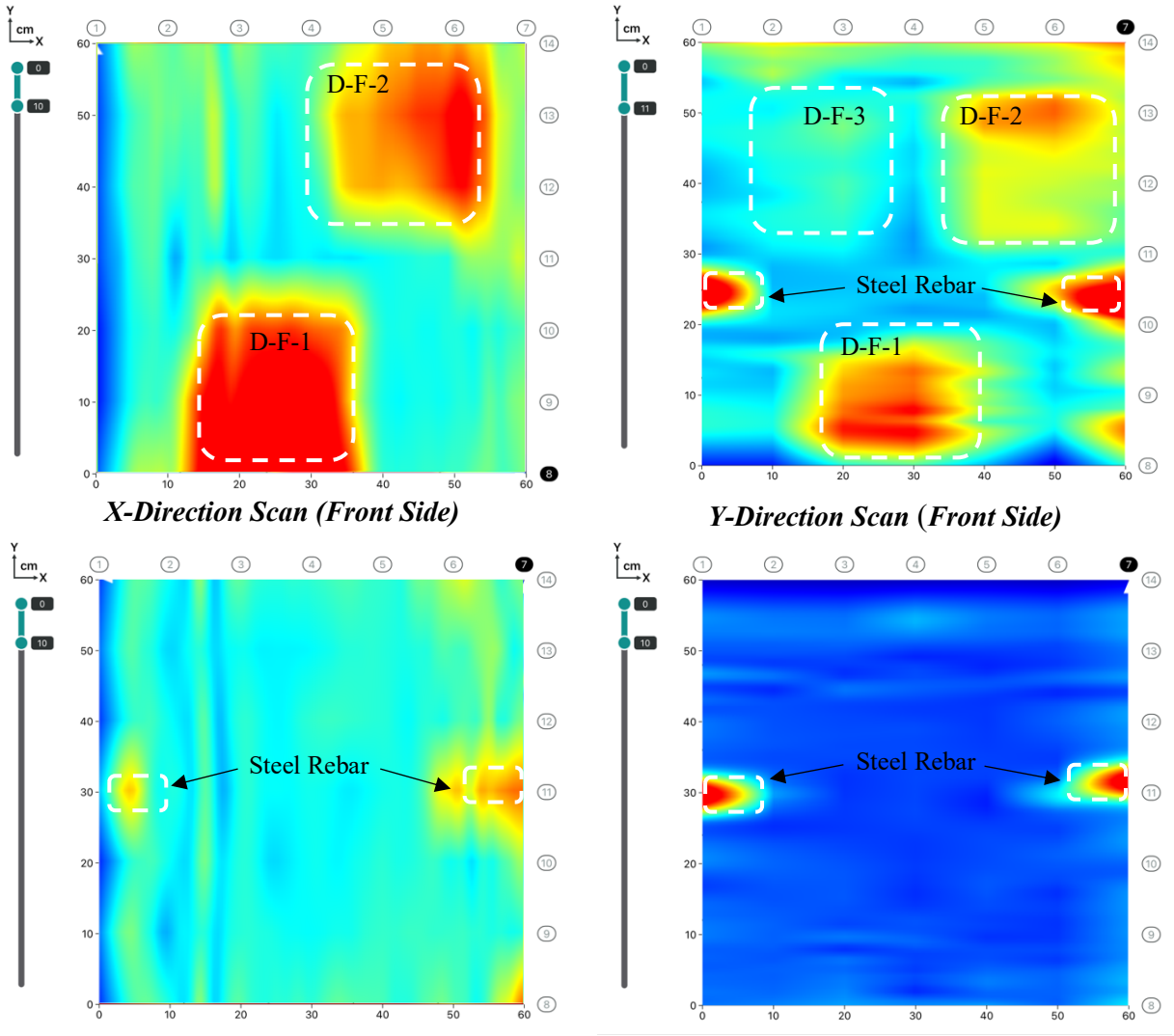

X-Direction Scan (Front Side)

Y-Direction Scan (Front Side)

X-Direction Scan (Back Side)

Y-Direction Scan (Back Side)

Figure 120 T-Scan Results of Specimen No. 1 (0 to 10 cm Depth)

The direction of the axes in the images is adjusted according to the direction of the scan paths. The defects are indicated as D-F-1, D-F-2, and D-F-3, with thicknesses of 0.7 mm, 2.5 mm, and 4.5 mm, respectively. The color variation corresponds to the differing signal responses from each defect's distinct thickness; thinner defects likely present as lighter anomalies on the scan, while thicker defects appear with more intense coloration due to their greater impact on the electromagnetic waves. In the top scans (X-Direction and Y-Direction Front Side), the defects were placed 1 cm below the surface. Here, D-F-1 (the thinnest) is shown in a lighter red, D-F-2 (medium thickness) in a deeper red, and D-F-3 (the thickest) in the most vivid red to yellow hues. The pronounced color differences highlight how GPR signal amplitude and phase can change with defect thickness. On the bottom scans (X-Direction and Y-Direction Back Side), the defects were placed deeper within the specimen, at 9 cm

from the surface. This greater depth, combined with the concrete cover, can cause the GPR signal to attenuate, potentially explaining why the back side scans show less pronounced color differentiation and the defects are not as easily distinguishable as on the front side. The scans also consistently show the steel rebar as bright reflections due to the strong contrast in dielectric properties between the steel and the surrounding concrete, verifying the GPR's capability to identify metallic objects within a concrete matrix at varying depths.

Notably, the steel rebars are less conspicuous in the X-direction scans than in the Y-direction scans. This reduced visibility is attributed to the orientation of the rebar in relation to the scan direction. When the GPR scan is conducted parallel to the length of the rebar—as is the case in the X-direction scans—the radar signal's reflection from the rebar is not as prominent because the electromagnetic wave is not encountering a perpendicular or significant cross-sectional area of the rebar to reflect back a strong signal. This results in a less distinct detection of the rebar on the GPR images. Conversely, in the Y-direction scans, where the GPR's path crosses the rebar perpendicularly, the radar waves reflect more efficiently off the rebar, creating clearer and more discernible signals that highlight the presence of the metallic bars within the concrete.

Figure 121 shows 3D representations of artificial delamination defects within Specimen No. 1, as identified by GPR scanning. The 3D views are derived from GPR data and showcase the location of the defects D-F-1, D-F-2. The delamination D-F-3 is not visible in the images. The upper two images represent the X-direction and Y-direction scans of the specimen's front side, indicating that the defects were positioned at a depth of 1 cm from the surface. These defects appear as shaded shapes in 3D space, with the varying thicknesses likely causing differences in color intensity or shape representation in the actual GPR software outputs.

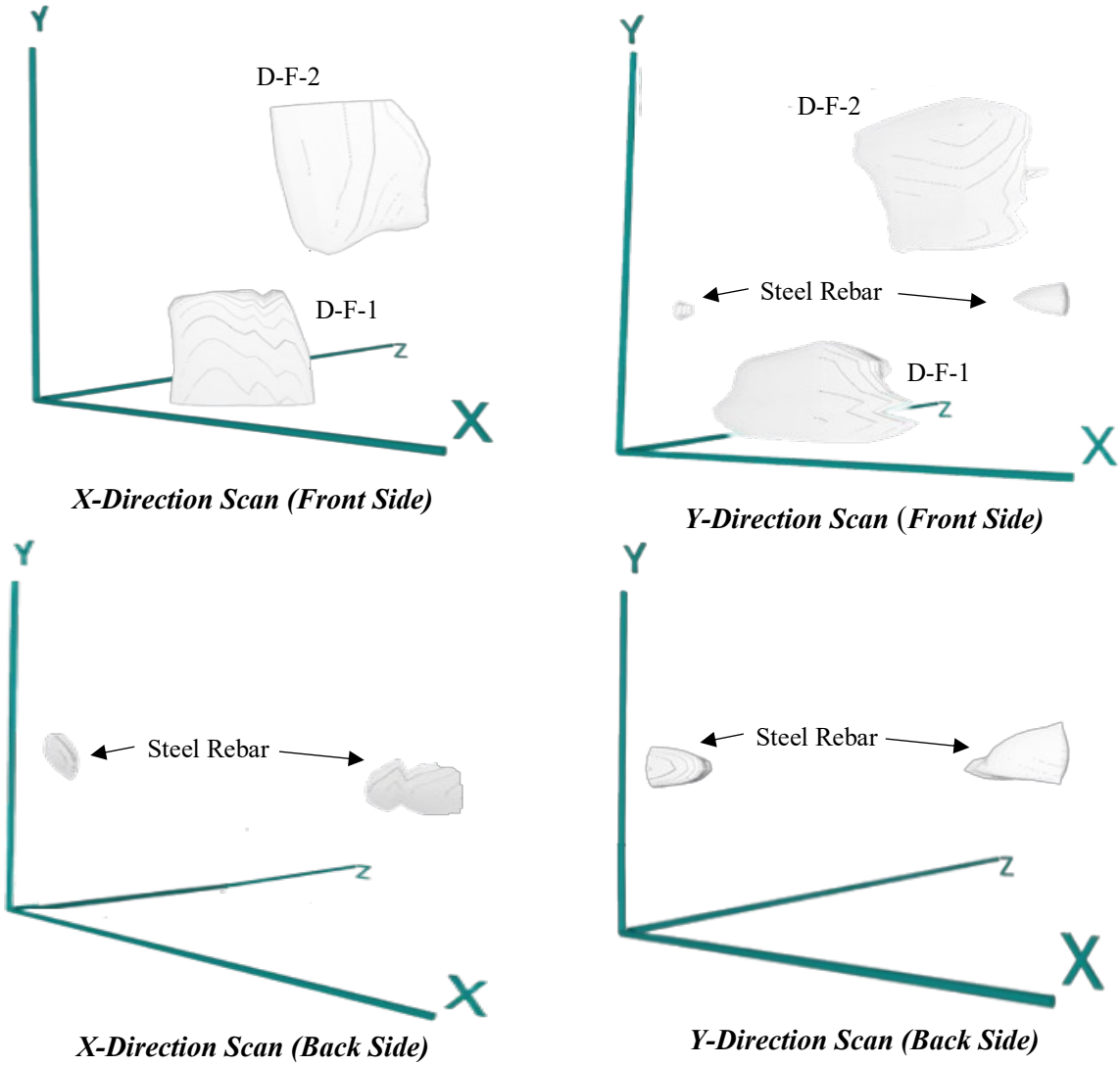

Figure 121 3D View of Defects of Specimen No. 1

The lower two images illustrate the scans from the back side of the specimen. Since the defects are located at a depth of 9 cm in the sample, they are not seen in the results. The steel rebar is indicated in each scan direction but appears more defined in the Y-direction scan, which is consistent with the alignment of the rebar being perpendicular to the scan direction, making it more detectable, as discussed previously. The 3D renderings help to visualize the relative positions and dimensions of the defects and the rebar within the concrete matrix, demonstrating the effectiveness of GPR in identifying structural and material differences within a scanned volume.

Figure 122 displays test results for Specimen No. 2, which was examined for void defects. The left section of the image shows multiple A-scans, revealing the variation in signal reflection at different depths. On the right image, the B-scan depicts a two-dimensional cross-sectional view of the specimen, highlighting two marked void defects, the location of the steel rebar, and the bottom edge

of the specimen. This provides insight into the internal features and demonstrates GPR's capability to detect subsurface anomalies such as voids.

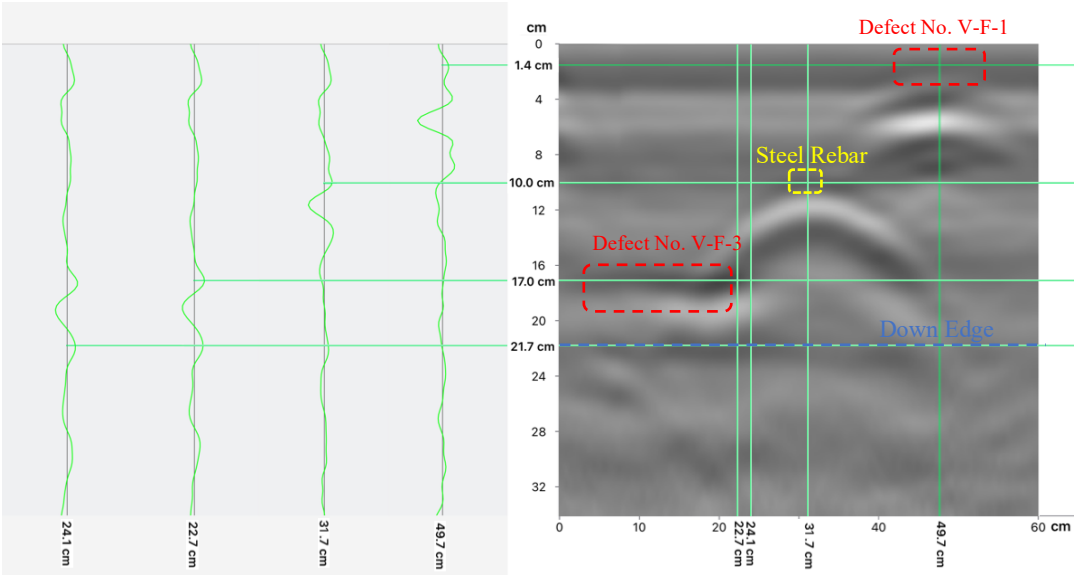

A-Scans ***B-Scan***

Figure 122 A-Scans and B-Scan of Front Side of Specimen No. 2 (Line 1- X-Direction Scan)

Figure 123 illustrates full-depth T-Scans from GPR testing on Specimen No. 2, with artificially introduced voids defects of varying thicknesses and depths, which explains the different colors observed in the scans. The direction of the axes in the images is adjusted according to the direction of the scan paths. The scans show that voids closer to the surface have stronger signal reflections, hence clearer visibility, while those deeper have weaker signatures. Additionally, steel rebar is consistently detected in Y-direction scans due to its significant contrast with the concrete's dielectric properties. It is notable that again the steel rebar is less conspicuous in the X-direction scans than in the Y-direction scans.

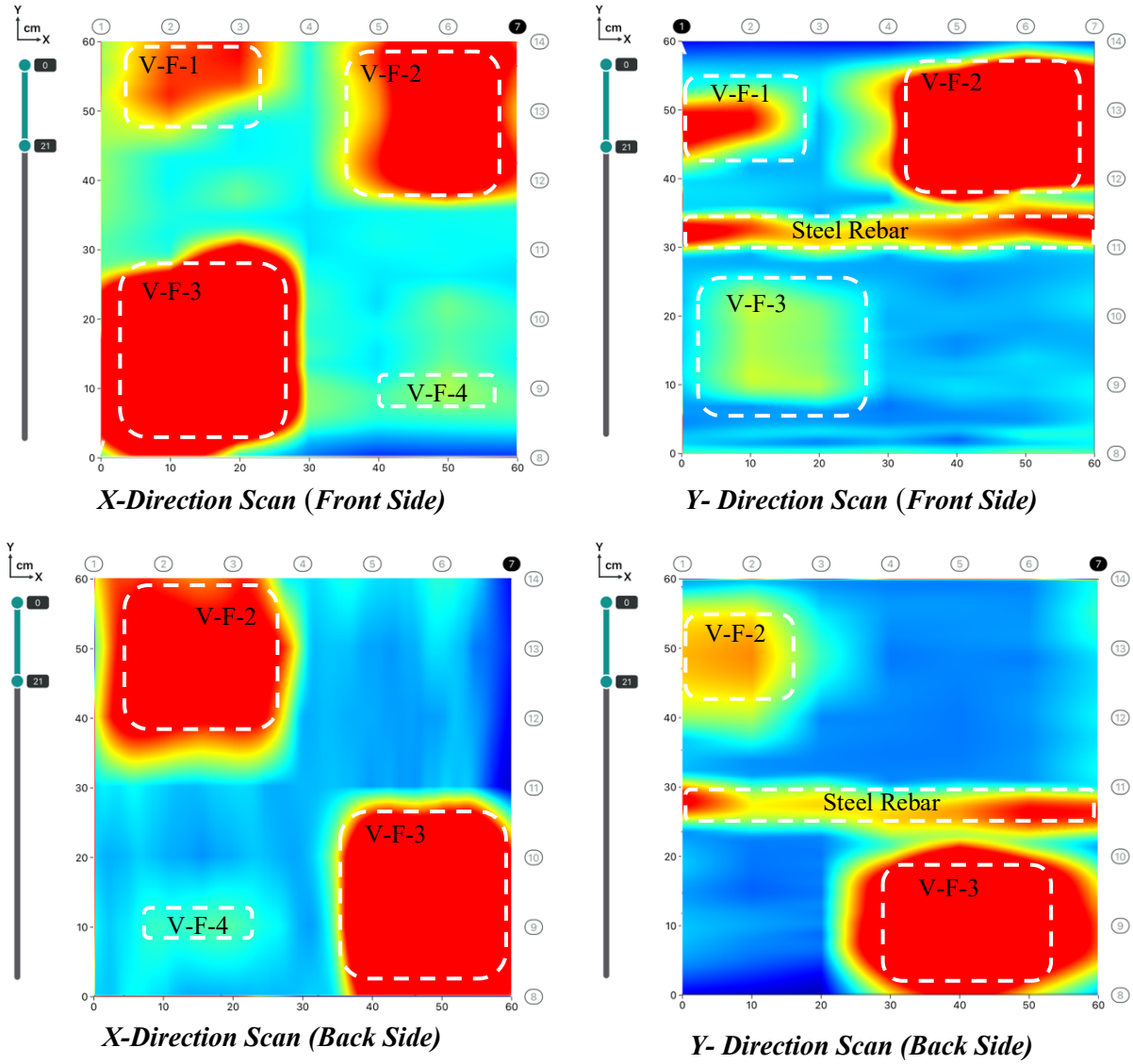

Figure 123 T-Scan of Specimen No. 2 (0 to 21 cm Depth)

Figure 124 shows 3D representations of artificial void defects within Specimen No. 2, as identified by GPR scanning. The 3D views are derived from GPR data and showcase the location of the defects.

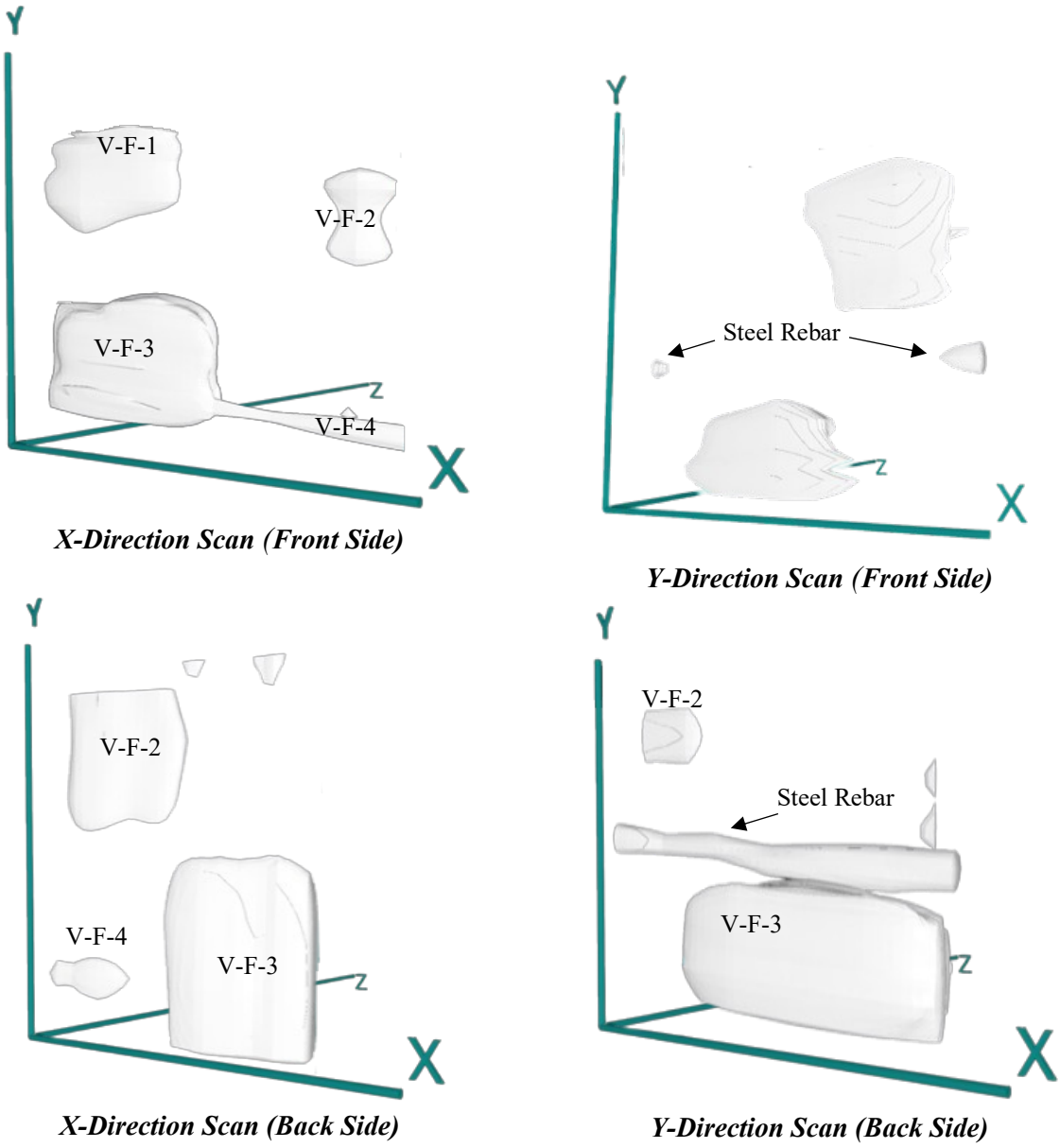

X-Direction Scan (Front Side)

Y-Direction Scan (Front Side)

X-Direction Scan (Back Side)

Y-Direction Scan (Back Side)

Figure 124 3D View of Defects of Specimen No. 2

6.2.2 GPR Field Results

In this report bridge No. 22383 is selected to compare the efficiency of the GPR technique. In shallow delamination defects and surface cracks, denoted by solid black lines and black arrows, respectively, are closest to the surface. Deep delamination defects, indicated by solid blue boxes, are farther from the surface. Corrosion or moisture, outlined in pink dashes, may not always be directly linked to visible defects but indicate a likely presence of conditions conducive to progressive deterioration and are typically spread across the structure, potentially affecting both the surface and

the subsurface. It shows that in BRKEY22283 longitudinal cracks are mostly in the corrosion/moisture areas. Therefore, crack patterns can indicate the type of subsurface defects. It also shows the locations of defects obtained from the IRT test and those obtained from the GPR test are different.

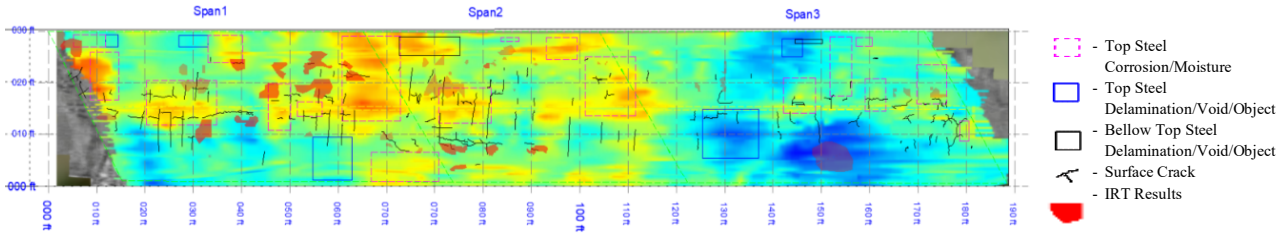

Figure 125 GPR Result of Bridge Deck No. 22283

6.3 Ultrasonic Pulse Velocity (UPV) Test

6.3.1 UPV Laboratory Results

Figure 126 illustrates the UPV test results, clearly indicating the locations of the voids and delamination. As depicted in Figure 27.a, the test successfully identified all three delamination defects, with variations in color intensity corresponding to the thicknesses of the defects. Notably, the TOF for the thinnest delamination defect D-F-1 (0.7 mm) is greater than that for defects D-F-2 (2.5 mm) and D-F-3 (4.5 mm), indicating that ultrasonic waves travel faster through thinner delamination defects. Figure 126.b demonstrates that for void V-F-1 (9 mm thickness), the TOF is greater than voids V-F-2 and V-F-3, both with a thickness of 25 mm. Despite being at different depths, V-F-2 and V-F-3 exhibit similar TOF, suggesting that depth has a negligible impact on the wave velocity in this case. For the vertically oriented void V-F-4, with a small cross-sectional area, the UPV test was able to detect its presence, albeit with less clarity than the larger voids V-F-2 and V-F-3.

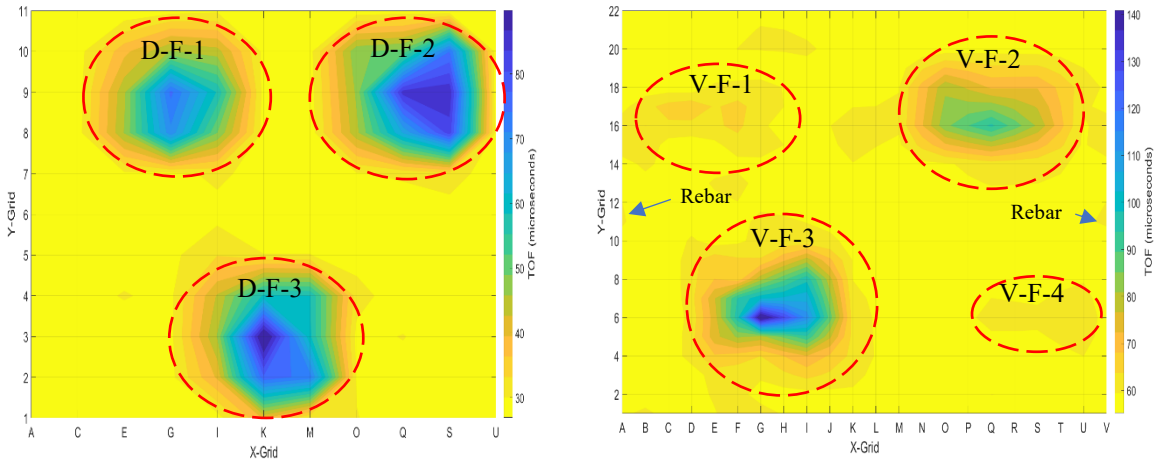

a. SpecimenNo.1 (Delamination) *b. SpecimenNo.2 (Voids)*

Figure 126 Defect Mapping of both Specimens Using UPV Test

6.4 Sounding Test

Chain dragging and Hammer Sounding Tests are two traditional sounding test, low-tech methods used for evaluating the integrity of concrete structures, particularly to locate delamination defects, voids, and other defects that might not be visible on the surface. Chain dragging method involves dragging a chain across the concrete surface or tapping it with a chain. Sound concrete will produce a clear, ringing sound, whereas delaminated areas will create a dull or hollow sound due to the separation between the concrete layers, which changes the acoustic properties. This technique is effective over larger areas and is commonly used on horizontal surfaces such as bridge decks and slabs where the resonance produced by the chain can be easily distinguished. The hammer sounding test is similar to chain dragging, this method involves striking the concrete with a hammer. The practitioner listens for variations in the sound produced by the hammer blows. A solid "thunk" sound typically indicates intact concrete, while a hollow "thud" may suggest a defect such as a delamination, void, or area of deterioration. Hammer sounding is more localized than chain dragging and can be used on vertical structures and horizontal surfaces.

6.4.1 Laboratory Sounding Test Results

The test involves dropping a stone ball onto the concrete surface and recording the resulting sound across each grid section with a sound meter. The maximum decibel (dB) level of the sound produced by the impact of the stone ball on the concrete is measured and analyzed. A higher dB level typically indicates a solid area, while a lower dB level may indicate the presence of delamination defects or voids where the sound is more subdued due to the lack of dense material to propagate the sound waves effectively. By systematically performing this test across the entire grid and recording the sound levels at each point, it is possible to create an acoustic map of the concrete specimen. This map can then be analyzed to locate and outline the defects. Areas with significantly lower dB readings compared to the surrounding grid areas are marked as potential defects. The results provide a visual and quantitative indication of the specimen's condition, allowing for targeted further investigation or repair.

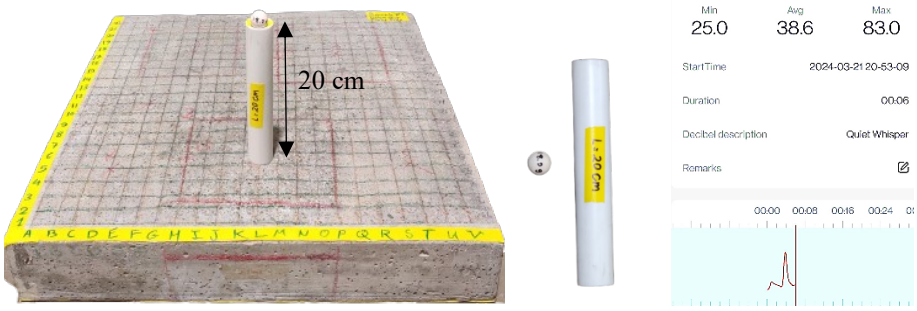

Figure 127 Setting of Sound Test on Specimen No. 1 (Front Side)

The results from the sound test on specimen No. 1, as shown in Figure 128, indicate the maximum decibel levels recorded after performing the test on the front side of the specimen across rows 1 to 22. The color gradient illustrates the locations of defects. Cooler colors denote lower dB levels, while warmer colors signify higher dB levels. This offers a visual indicator to identify areas of the sample that may have compromised integrity. The results show that this technique can detect all shallow delamination.

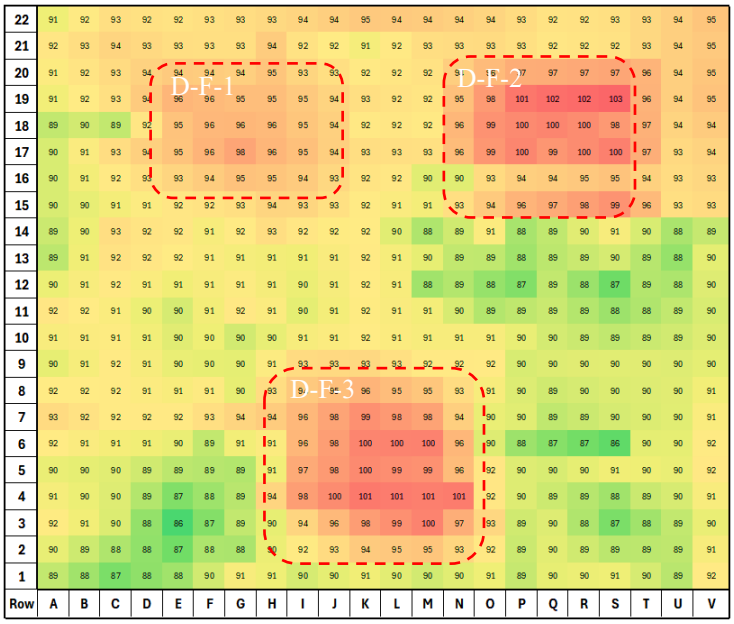

Figure 128 Sound Test Results of Specimen No. 1 (Front Side)

Focusing more on the data of defects area illustrates a noticeable range of sound volumes pointing to the regions of defects marked D-F-1 and D-F-2 (Figure 129). The data indicates that in regions D-F-1 and D-F-2, the average sound volume registered at 95 dB and 98.5 dB, respectively, in contrast to an average of 92.8 dB in other regions. Similarly, in Figure 130, defect D-F-3 shows an average sound volume of 96.2 dB, whereas the surrounding areas average at 89.9 dB. These elevated sound levels in the region of defects are significant when compared to the non-defected areas. The variations in sound

volume are directly correlated with the thickness of the delamination. Delamination D-F-1, with the smallest reported thickness of 0.7 mm, shows a slight increase in sound volume, while D-F-2 and D-F-3, with greater thicknesses of 2.5 mm and 4.5 mm, respectively, exhibit progressively higher average sound volumes. This escalation in sound volume with the increasing thickness of delamination is consistent with the physical properties of concrete. Thicker delamination defects are likely to create a larger cavity, which would lead to a more pronounced acoustic response when impacted by the stone ball.

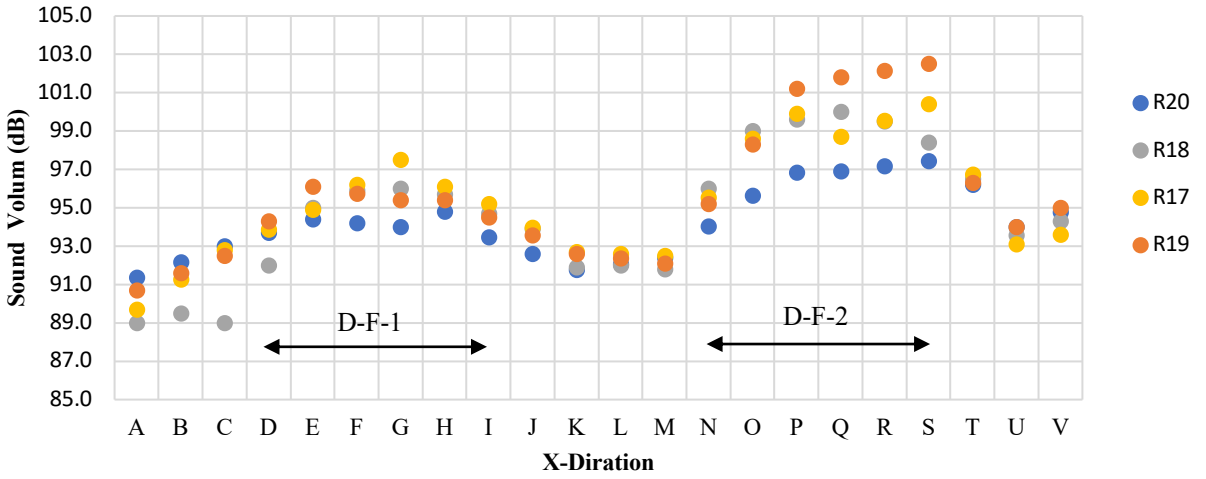

Figure 129 Sound Test Data in Rows 17 to 20

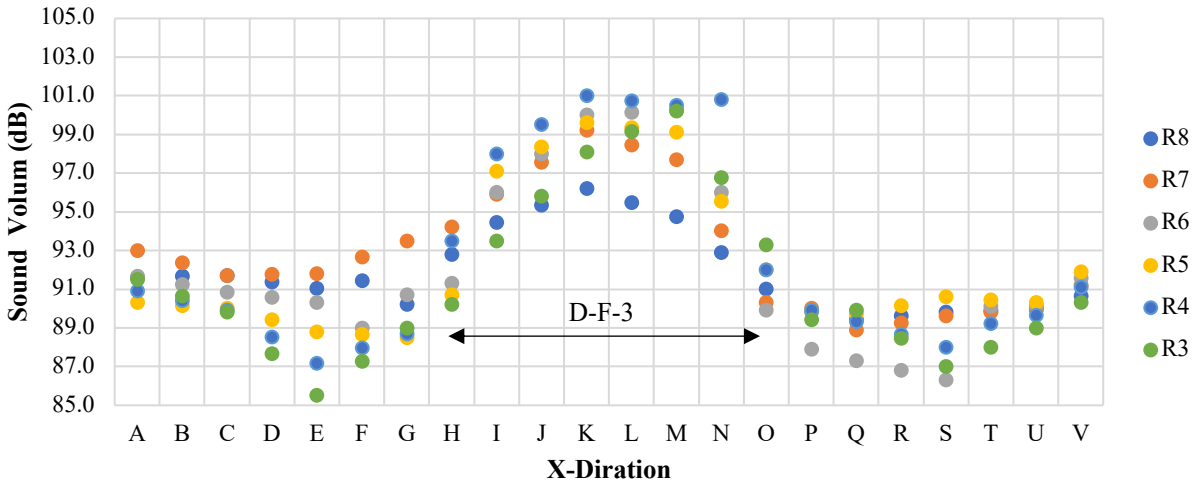

Figure 130 Sound Test Data in Rows 3 to 8- Specimen No. 1

The results from the sound test on specimen No. 2, as shown in Figure 131, indicate the maximum decibel levels recorded after performing the test on the front side of the specimen across rows 1 to 22. The color gradient illustrates the locations of defects. Cooler colors denote lower dB levels, while warmer colors signify higher dB levels. This offers a visual indicator to identify areas of the sample

that may have compromised integrity. The results show this technique can detect shallow defects, such as void V-F-2, and even vertical void defects, like V-F-4. While the void V-F-1 is barely visible due to its lower thickness (9 mm), the deep void V-F-3 is not detectable at the depth of 17 cm.

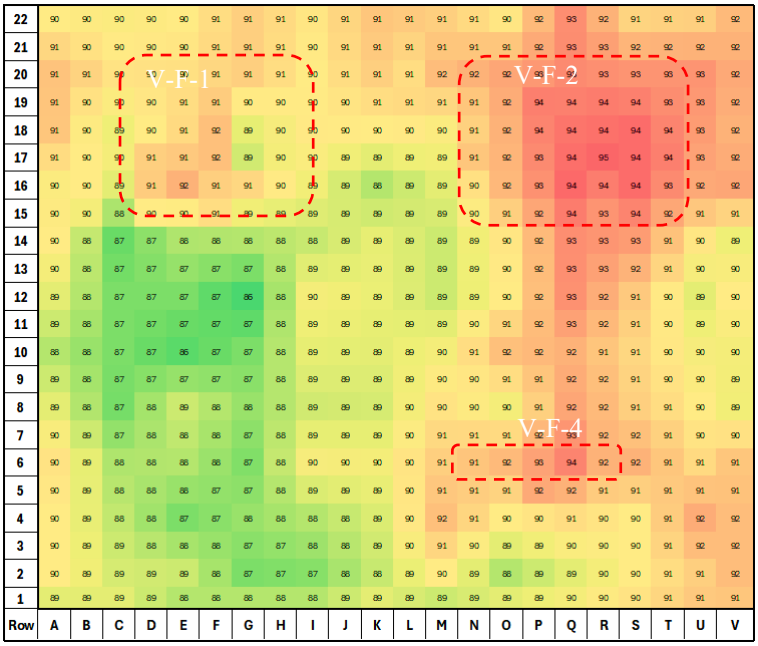

Figure 131 Sound Test Results of Specimen No. 2 (Front Side)

Focusing more on the data of defects area in Figure 31 illustrates a noticeable range of sound volumes pointing to the regions of defects marked V-F-2 (average 93.1dB) and V-F-4 (92.1dB) in contrast to an average of 90.9 dB in other regions. In this test, the shallow void V-F-2, which has a thickness of 25 mm and is located at a depth of 4 cm from the surface, is indicated by the consistent variation in sound levels within a defined region on the graph This shows that the sound test is sensitive enough to detect such defects, as evidenced by the localized increase in dB levels where the void V-F-2 is present. The results also illustrate the test's capability to detect vertical voids, exemplified by V-F-4, a vertical void with a thickness of 25 mm situated at a depth of 5.2 cm. In the laboratory condition, the vertical orientation of the void does not hinder the test's ability to register a distinct acoustic response, marking its position on the specimen with a specific sound volume profile that stands out from the adjacent areas.

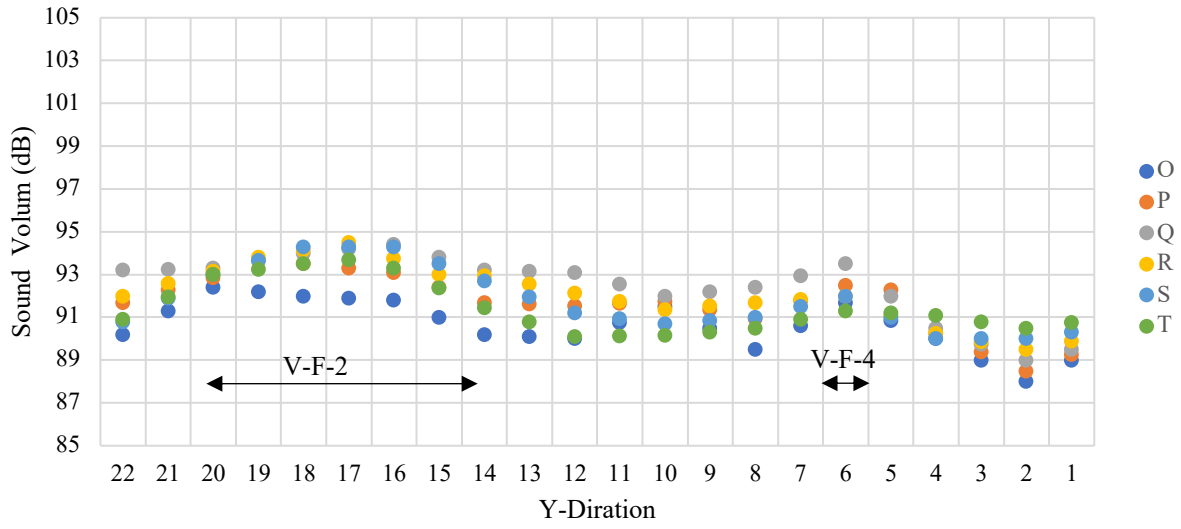

Figure 132 Sound Test Data in Column O to T- Specimen No. 2

6.4.2 Chain Dragging Field Results

In this report bridge No. 22383 is selected for comparing the efficiency of high-speed chain dragging technique. Figure 133 provides a deterioration map of the bridge deck from chain dragging acquired by the high-speed data collection system. Overall, the Chain Drag results indicate a high amount of delamination throughout the deck with higher concentration in the northwest regions of the deck. The quantitative assessment below shows the percentage of defects picked by the chain drag system. The "Delaminated" category indicates a very high likelihood of the presence of subsurface damage, out of which the "Severe" portion is dedicated to areas of the bridge deck that the chain drag deems the strongest reflection of sound from the delaminated area. It's worth mentioning that due to the physical working principles of chain drag sounding, deep delamination will not be picked up by the chain drag system at higher speeds which prompts the use of other NDT techniques like ultrasonic testing or chain dragging at speeds of 2 mph where necessary. The areas of severe delamination are shown in bright yellow while the moderate areas are shown in darker yellow with the blue background depicting the intact regions. Please note that the span demarcations are visible on the chain drag plot and marked in red [1].

The sound test results for Bridge No. 22383 indicate that the IRT results, marked in red rectangles, correspond to the detected defects, whereas the surface cracks do not coincide with these detected defects.

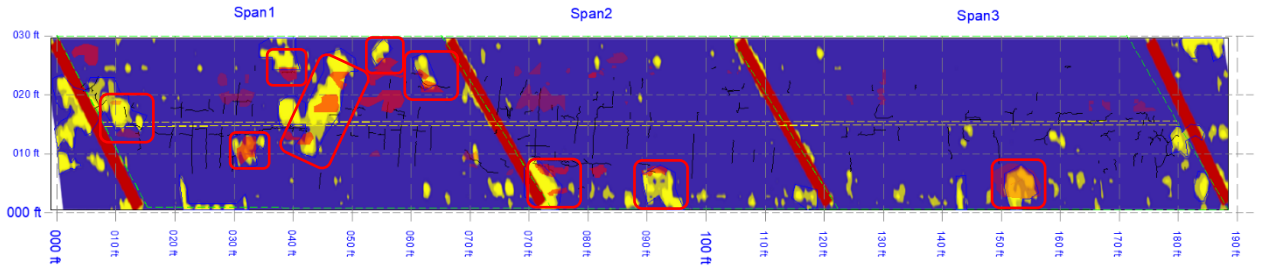

Figure 133 Chain Dragging Contour Map of Bridge Deck No. 22383 [2]

The results of another chain dragging test are shown in Figure 134. Large areas of the wearing surface sounded like the latex overlay was not adequately bonded. These areas are generally marked in blue. The results of this test do not completely match the location of the defects identified in the sound test conducted by the subcontractor.

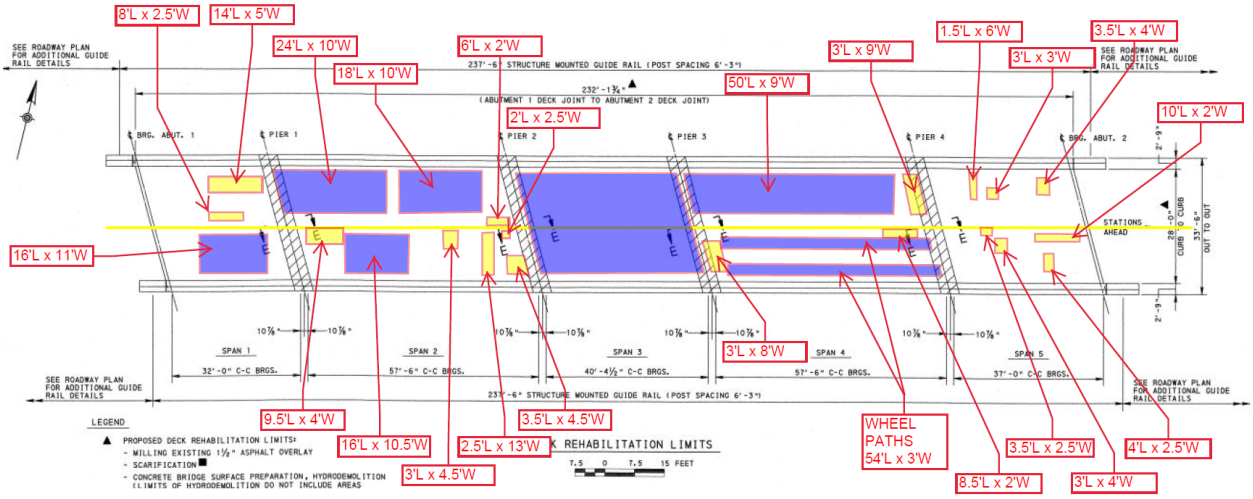

Figure 134 Chain Dragging Map of Bridge Deck No. 22383

6.5 Discussion

In the laboratory specimens, artificial defects are representative of real void/delamination defects. Shallow void/delamination: Defects under this category are situated close to the surface of the bridge decks. They are identified by the defect numbers D-F-1, D-F-2, D-F-3, and V-B-3. Such defects may affect the surface integrity and could be indicative of the beginning stages of degradation. Top steel void/delamination: These defects are located near the steel reinforcement within the concrete in bridge decks, marked as V-F-1 and V-F-2. This proximity to the reinforcement can be critical because it could affect the load-bearing capacity and durability of the reinforced concrete. Deep void/delamination: Listed as D-B-1, D-B-2, D-B-3, V-B-1, and V-B-2, these defects are positioned deeper within the bridge decks, posing significant challenges for detection. Deep voids or delamination can compromise the structural integrity of concrete from within, often going unnoticed

until significant damage has occurred. Vertical void/delamination: These are identified as V-F-4 and V-B-4. The vertical orientation of these defects can make them particularly difficult to detect in bridge decks using some non-destructive methods, which typically scan horizontally. Their presence can have varying implications for the structural bridge decks health, depending on their location and extent. The creation of these defects in a controlled laboratory setting allows for the systematic testing of non-destructive evaluation (NDE) techniques, ensuring they can accurately detect and size such defects in actual bridge decks.

Interpreting IRT data requires understanding how various conditions affect thermal signatures. External factors such as sunlight, wind, and humidity can significantly influence thermal readings. Therefore, the timing of the thermographic survey is critical, with some conditions best observed under specific environmental conditions (e.g., after sunset or during the early morning). IRT is particularly useful for identifying large-scale anomalies in concrete structures, such as shallow delamination or voids, but it may not be as effective for detecting smaller-scale deficiencies like fine cracks. Often, IRT needs to be used in conjunction with other non-destructive testing methods to provide a more comprehensive assessment of the concrete structure's condition.

Deficiencies such as corrosion, very thin delamination, and high moisture content can be found in the GPR data because they cause signal attenuation. Deficiencies such as larger debonding, air gaps, or embedded objects exhibit a noticeably different dielectric constant and tend to create areas with high amplitude reflections. Interpreting GPR data requires understanding how various conditions affect signal signatures. They mainly pertain to irregularly weak and strong reflections, respectively. Deficiencies such as corrosion at any depth, very thin delamination, and high moisture content at lower depths cause signal attenuation and exhibit weak reflections, whereas larger debonding, air gaps, voids, and embedded objects (including embedded utilities) exhibit a noticeably different dielectric constant, tend to create areas with high amplitude reflections, and are characteristic of strong reflections. Although moisture is not a permanent deficiency, it has the potential to create a response similar to both debonding and corrosion, depending on the nature of the moisture.

For conventional reinforced concrete decks, IRT technology detects delamination within the shallow subsurface of concrete decks, while GPR technology can detect beneath this shallow range into deeper depths. The strengths of IRT and GPR can be balanced by leaning on IRT to detect shallow sub-surface defects accurately and leaning on GPR for shallow to full-depth detection. High noise and the need for heavy filtering applications to shallow levels in GPR datasets can often reduce the

detectability of shallow findings.

The chain-dragging technique is efficient due to its simplicity and the minimal equipment required. It involves dragging a chain or striking the surface with a hammer and listening to the acoustic response. Solid concrete will produce a clear, ringing sound, while delaminated areas will create a hollow or dull sound. This method is most efficient in environments where ambient noise levels are low, as this allows the inspector to clearly hear the changes in sound. The method relies heavily on the skill and experience of the inspector to correctly interpret the acoustic signals. It is a quick method for scanning large areas and is cost-effective since it does not require sophisticated equipment. Chain dragging is quite effective at detecting shallow delamination, as the void created by delamination changes the sound produced when the chain is dragged over it. Like delamination, Voids also alter the acoustic signature of the concrete when subjected to the chain dragging technique. However, there are limitations to the technique. It is not effective for identifying deep or very small defects because the sound change may not be perceptible. The accuracy can be affected by background noise, making it less suitable for noisy environments. It requires accessible and relatively even surfaces for the chain or hammer to be used effectively. It is qualitative rather than quantitative, which means that while it can detect the presence of anomalies, it cannot easily measure their size or depth without additional investigation.

To compare all field data in one image an overview shot of all results for bridge deck No. 22383 is shown in Figure 135. As it is shown IRT test can detect delamination/voids below to steel that are detected by GPR (shown as black hatched areas) or sound testing. Thies areas are not considered in the subcontractor's report as results of IRT (shown as green hatched areas).

Overall, these results indicate that the IRT test can provide accurate information on the location of shallow and even top steel delamination defects.

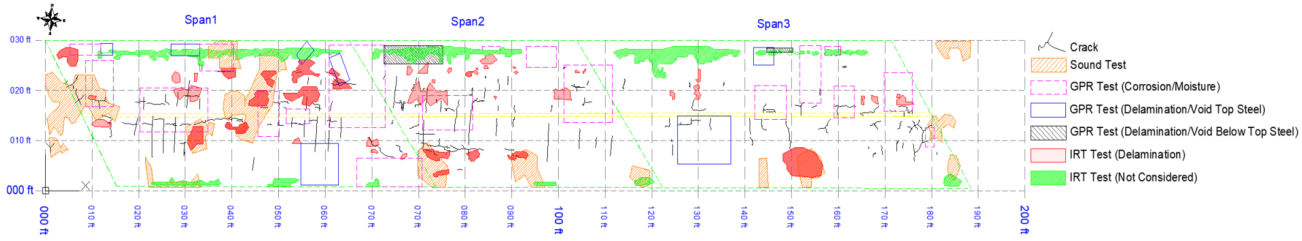

Figure 135 Overview Shot of All Results of Bridge Deck No. 22383

6.5.1 Comparison of Efficiency Among Different Techniques

Table 15 provides an overview of how different detection techniques perform in identifying

various structural defects within concrete, as evidenced by both field and laboratory results.

Table 15- Summary of the Comparison of Efficiency Among Different Techniques

Cases of Defects	Field Results				Laboratory Results			
	IRT	GPR	Chain Dragging	Crack Mapping	IRT	GPR	Sounding Test	Ultrasonic
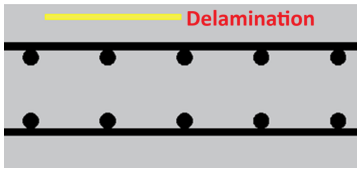 Shallow Delamination	☑	⊗	☑	⊗	☑	☑	☑	☑
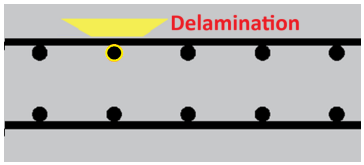 Top Steel Delamination Duo to Corrosion/Moisture	⊗	☑	☑	☑	☑	☑	☑	☑
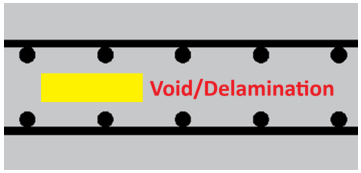 Deep Void/ Delamination	⊗	☑	⊗	⊗	⊗	☑	⊗	☑

It assesses the efficiency of six techniques: Infrared Thermography (IRT), Ground Penetrating Radar (GPR), Chain Dragging, Crack Mapping, Sounding Test, and Ultrasonic methods. Each technique is evaluated against four common types of defects including delamination, shallow delamination, top steel delamination due to corrosion/moisture, deep void/delamination.

7 Model Development

Image analysis techniques, leveraging the power of machine learning (ML) and computer vision, have become pivotal in enhancing the capabilities of NDT methods. By automatically analyzing images obtained from various NDT techniques, such as IRT, GPR, crack mapping, and chain-dragging, ultrasonic testing. These advanced algorithms can efficiently detect, classify, and quantify defects with acceptable accuracy. This automation not only significantly reduces the time and labor involved in manual inspections but also improves detection reliability by minimizing human error. The integration of image analysis into NDT processes enables early detection of flaws such as cracks, corrosion, delamination, or voids in concrete, ensuring the safety, integrity, and durability of bridges. In this report, we detail the development of a simple model utilizing image analysis techniques for the detection of defects in bridge decks, with a particular focus on identifying delamination and voids. By harnessing the capabilities of ML and computer vision, our model processes images derived from advanced NDT methods, enabling it to accurately detect, classify, and quantify various types of concrete flaws. This approach significantly enhances the speed of defect detection processes, offering a tool for ensuring the integrity and longevity of materials and structures under examination.

We employed the "Trainable Weka Segmentation" tool within the Fiji application to develop a model aimed at conducting image analysis. Fiji, or ImageJ, is an open-source platform that enhances ImageJ by bundling it with various plugins to facilitate scientific image analysis. One of these powerful plugins is the Trainable Weka Segmentation, which leverages ML algorithms from the Weka suite to perform the segmentation of images. The process involves training the model with examples of the areas of interest (such as defects) and the background or noise. Users manually select samples of these categories in the images, and the tool then uses this input to learn how to distinguish between the desired features and the irrelevant parts of the image. This learning process is based on various image characteristics, including texture, color, and shape. Once trained, the model can automatically segment new images, accurately identifying and isolating the features of interest from the background, thereby facilitating detailed image analysis tasks such as defect detection in materials. This approach is particularly beneficial for complex image analysis tasks where precise differentiation between features is crucial.

7.1 Trainable Weka Segmentation (TWS)

The Trainable Weka Segmentation is a Fiji plugin that combines a collection of ML algorithms

with a set of selected image features to produce pixel-based segmentations [5], [6]. Weka (Waikato Environment for Knowledge Analysis) can itself be called from the plugin. It contains a collection of visualization tools and algorithms for data analysis and predictive modeling, together with graphical user interfaces for easy access to this functionality. The classifier used in this model is Fast Random Forest (FRF). As described on their website, the advantages of Weka include:

- freely available under the GNU General Public License
- portability, since it is fully implemented in the Java programming language and thus runs on almost any modern computing platform.
- a comprehensive collection of data preprocessing and modeling techniques
- ease of use due to its graphical user interfaces.
- Weka supports several standard data mining tasks, more specifically, data preprocessing, clustering, classification, regression, visualization, and feature selection.

In this report bridge No. 22383 is selected for developing a model. In Figure 136 we see a visualization of the output from a trained model analyzing Infrared Thermography (IRT) data on bridge deck No. 22383. Red areas in the image indicate potential defects as identified by the model. The percentage of defect areas is 6.52%. The yellow rectangles are highlighting areas where the model may not be working correctly. The left one is not a defect. Also, the model has missed the defect that should have been identified for the right rectangle. The parameters used to determine what constitutes a defect might be too strict or too lenient, leading to incorrect classifications.

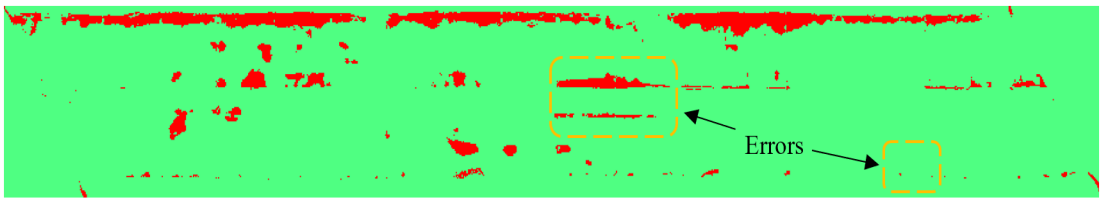

Figure 136 Output of the Model for the IRT (Daytime) Results of Bridge Deck No. 22383

The file of the trained model for classifying IRT image is available through the link of "IR_classifier.model". This model can be applied to additional IRT images for the purpose of diagnosing defects.

Figure 137 is the output of GPR cover thickness images of bridge deck No. 22383. The red areas on the green background represent regions where the cover thickness of a bridge deck is different from the norm, suggesting potential defects or areas of concern. The percentage of areas of concern is 4.74%.

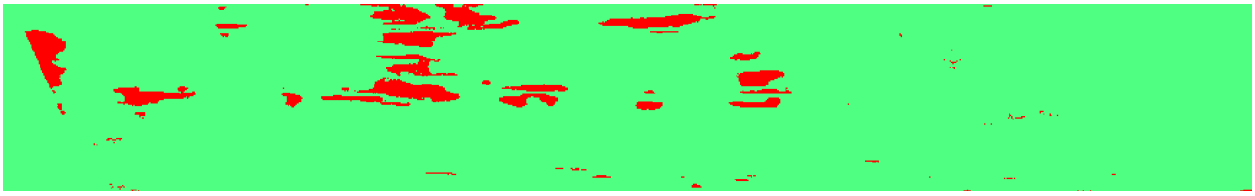

Figure 137 Output of the Model for the GPR_Cover_Thickness Results of Bridge Deck No. 22383

The file of trained model for classifying This type of GPR images available through the link of "GPR_classifier.model". This model also can be applied to additional GPR images to diagnose cover thickness.

The left image of Figure 138 presents a segment of asphalt overlay part before bridge deck No. 22383 where various cracks are discernible. These cracks manifest as irregular lines on the surface, creating a network of fractures within the asphalt. On the right, we have the processed image output, which employs the Weka segmentation algorithm to detect and delineate these cracks for clearer visualization. This enhanced image starkly contrasts the cracks against the intact surface by rendering the cracks in red against a uniform green background.

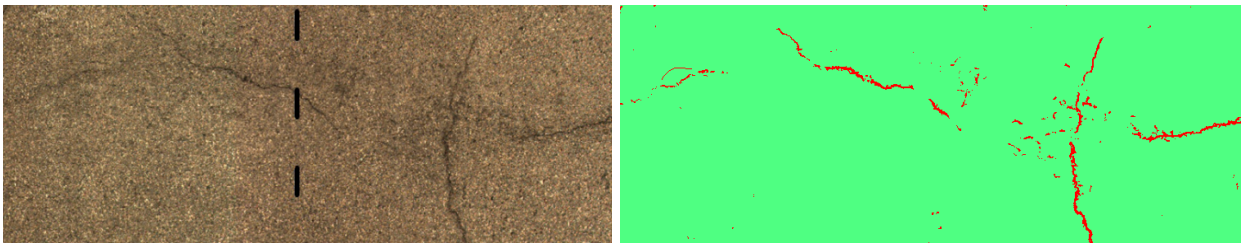

Figure 138 Detecting Cracks on Asphalt Overlay

In Figure 139 the raw image on the left depicts the surface of a concrete bridge deck characterized by regular grooves and a heterogeneous texture due to aggregates of various colors and sizes.

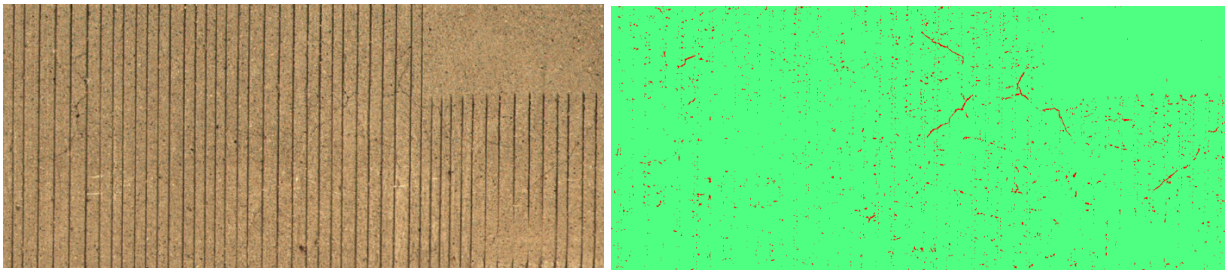

Figure 139 Detecting Cracks on Concrete Bridge Decks

Detecting cracks on such a surface, as evidenced by the processed image on the right, is considerably more challenging. This is due to the 'noise' introduced by these grooves and spots, which can be similar in appearance to actual cracks. The processed image illustrates this difficulty; while cracks are indeed highlighted in red, many other features -such as the linear grooves and darker

aggregate spots- are also picked up by the crack detection algorithm. These false positives, often referred to as 'noise,' complicate the analysis, requiring more sophisticated processing techniques or manual verification to ensure accurate crack detection. Effective segmentation in such contexts often depends on the ability of the algorithm to discriminate between genuine structural flaws and innocuous textural or color variations intrinsic to the concrete material.

To increase the model's efficiency and reliability in detecting defects such as cracks, delamination, and voids, enhancing its accuracy by eliminating noise that can interfere with the detection process is crucial. This noise includes extraneous features within the images, such as the grooves in bridge decks, rebars, shadows, and moisture, which can obscure or mimic the appearance of defects, leading to false positives or negatives. Addressing this challenge necessitates training in a more sophisticated model using advanced Artificial Intelligence (AI) techniques. This process requires a significant investment of time and a substantial increase in the quantity and variety of input data to ensure the model learns to distinguish between true defects and noise accurately. By doing so, the model can achieve higher precision in defect detection, thereby increasing the reliability of assessments and the safety of the evaluated structures.

8 Conclusion

1- IRT tests can provide accurate information on the location of shallow and even some top steel delamination defects. The results also indicate that sound tests cannot detect all the defects identified in the IRT tests. Therefore, applying active methods, such as heating the bridge deck surface while performing IRT tests, can significantly enhance the accuracy of IRT techniques in evaluating the condition of bridge decks. Active IRT methods involve artificially inducing a thermal contrast between the defective and non-defective areas, amplifying the thermal signatures denoting subsurface anomalies such as delamination defects, voids, or moisture entrapment. By doing so, active IRT mitigates the limitations posed by ambient temperature fluctuations and solar loading, which often mask or distort the thermal patterns associated with such defects. Consequently, the implementation of active methods improves the reliability of the IRT results, providing clearer data for the assessment of bridge deck integrity.

2- The location of the cracks on the bridge's surface does not nearly match the location of the defects identified in the IRT and sound tests.

3- Rebars and defects in the path direction cannot be detected by GPR.

4- GPR is an alternative to rebound hammering or chain dragging when a deck is covered.

5- In the field results, the defect locations identified by the Infrared Thermography (IRT) test differ from those detected by the Ground Penetrating Radar (GPR) test, indicating a variation in the sensitivity and diagnostic reach of the two methodologies. While IRT tends to highlight thermal inconsistencies on or near the surface, GPR can provide a more in-depth profile, revealing defects located further beneath the surface and possibly obscured from thermal detection.

6- A comprehensive exploration of the detection and classification of surface cracks by using the extraordinary capabilities of advanced deep learning models can help in determining the type and severity of subsurface defects. Crack patterns can indicate the type of subsurface defects. Using AI can help us in pattern recognition and finding defect types.

7- Comparing GPR images and surface crack mapping shows longitudinal cracks are in the same location as the corrosion/moisture area. It can help to find an advanced model to distinguish the corrosion and moisture area. In this matter AI, particularly through advanced machine learning and computer vision techniques, has revolutionized the field of pattern recognition,

enabling the efficient identification of bridge deck subsurface defects. By analyzing vast datasets of bridge imagery, AI algorithms can learn to recognize the subtle signs of various defect types, such as cracks, delamination, and corrosion, that might not be visible to the naked eye. This capability allows for more accurate and timely assessments of bridge health, facilitating early interventions that can prevent minor issues from escalating into major failures. AI's ability to quickly process and analyze images from regular inspections or continuous monitoring systems means that infrastructure managers can maintain safer, more reliable bridges with optimized maintenance schedules, reducing both risks and costs [7]

8- To boost the model's capability in accurately identifying defects like delamination, voids, and corrosion refining its precision by filtering out noise -such as grooves, rebars, shadows, and moisture in images- that can mask or imitate defects. This improvement demands the development of a more advanced model through extensive AI training, necessitating more time and a richer laboratory dataset to differentiate between actual defects and noise precisely, thus elevating the model's defect detection precision and the overall safety and reliability of structural assessments.

9 Appendix A - Crack Length of Bridges

Crack lengths on each span of bridge deck No. 22383 are as follows:

Table 16 Crack lengths of bridge Deck No. 22383- Span 1

Crack No.	Length (ft)	Crack No.	Length (ft)	Crack No.	Length (ft)	Crack No.	Length (ft)
C1	1.07	C21	1.52	C41	1.04	C61	1.20
C2	1.73	C22	1.13	C42	1.39	C62	0.85
C3	4.27	C23	0.59	C43	0.04	C63	2.46
C4	1.55	C24	0.45	C44	0.93	C64	1.82
C5	2.00	C25	0.09	C45	3.03	C65	1.82
C6	0.66	C26	1.54	C46	1.63	C66	2.15
C7	3.41	C27	1.89	C47	2.70	C67	5.12
C8	1.11	C28	4.02	C48	2.32	C68	2.09
C9	0.44	C29	7.01	C49	1.66	C69	1.21
C10	0.34	C30	2.30	C50	2.24	C70	0.88
C11	8.27	C31	7.91	C51	2.50	C71	2.78
C12	6.81	C32	1.52	C52	1.22	C72	4.20
C13	1.38	C33	6.89	C53	0.94	C73	2.08
C14	2.21	C34	2.57	C54	3.95	C74	1.40
C15	1.81	C35	3.34	C55	1.99	C75	0.02
C16	2.24	C36	3.46	C56	5.41	**Sum**	**184.11**
C17	8.17	C37	3.86	C57	2.58		
C18	2.58	C38	3.61	C58	5.38		
C19	0.88	C39	2.50	C59	2.07		
C20	1.77	C40	0.86	C60	1.28		

Table 17 Crack Lengths of Bridge No. 22383- Span 2

Crack No.	Length (ft)	Crack No.	Length (ft)	Crack No.	Length (ft)	Crack No.	Length (ft)
C75	1.38	C90	1.49	C105	2.54	C120	2.56
C76	2.04	C91	0.80	C106	1.50	C121	1.79
C77	1.60	C92	6.62	C107	2.20	C122	0.46
C78	7.57	C93	3.63	C108	0.51	C123	0.35
C79	9.15	C94	1.05	C109	5.48	C124	0.49
C80	2.29	C95	6.31	C110	1.67	C125	2.02
C81	6.09	C96	4.01	C111	2.32	C126	0.96
C82	1.14	C97	2.08	C112	0.89	C127	2.13
C83	0.30	C98	4.08	C113	1.52	C128	1.26
C84	2.15	C99	1.85	C114	1.60	C129	0.83
C85	1.36	C100	4.00	C115	0.91	C130	0.86
C86	0.52	C101	1.45	C116	2.77	C131	2.16
C87	0.29	C102	2.26	C117	3.36	C132	1.01
C88	0.86	C103	5.49	C118	0.78	**Sum**	**140.25**
C89	11.53	C104	0.96	C119	0.98		

Table 18 Crack Lengths of Bridge No. 22383- Span 3

Crack No.	Length (ft)	Crack No.	Length (ft)	Crack No.	Length (ft)	Crack No.	Length (ft)
C133	1.71	C148	3.83	C163	0.03	C178	2.52
C134	1.24	C149	1.67	C164	3.58	C179	1.89
C135	1.06	C150	2.97	C165	0.90	C180	4.18
C136	0.22	C151	0.58	C166	2.35	C181	1.16
C137	3.08	C152	5.54	C167	2.08	C182	0.89
C138	1.34	C153	1.95	C168	0.81	C183	2.76
C139	0.29	C154	1.41	C169	1.39	C184	1.79
C140	2.27	C155	4.76	C170	1.39	C185	0.42
C141	2.70	C156	1.04	C171	1.04	C186	2.00
C142	7.42	C157	2.65	C172	0.67	C187	1.48
C143	3.68	C158	2.84	C173	1.15	C188	2.25
C144	0.74	C159	2.97	C174	2.34	C189	0.01
C145	1.42	C160	3.25	C175	0.48	**Sum**	**115.47**
C146	1.14	C161	1.32	C176	0.79		
C147	2.04	C162	6.20	C177	1.78		

Crack lengths on each span of bridge deck No. 22266 are as follows:

Table 19 Crack Lengths of Bridge Deck No. 22266-Span 1

Crack No.	Length (ft)
C1	2.15
C2	5.62
C3	1.03
C4	3.44
C5	0.78
C6	1.96
C7	1.62
C8	1.03
C9	2.65
Sum	**20.28**

Table 20 Crack Lengths of Bridge Deck No. 22266-Span 2

Crack No.	Length (ft)	Crack No.	Length (ft)	Crack No.	Length (ft)	Crack No.	Length (ft)
C10	0.47	C18	3.25	C26	1.91	C34	1.87
C11	2.01	C19	1.85	C27	2.94	C35	5.45
C12	1.25	C20	0.67	C28	2.34	C36	2.27
C13	1.18	C21	1.06	C29	1.61	C37	0.53
C14	0.92	C22	1.6	C30	2.54	C38	0.79
C15	4.36	C23	6.55	C31	4.04	C39	0.66
C16	4.76	C24	2.59	C32	3.09	C40	0.66
C17	2.03	C25	2.73	C33	1.24	**Sum**	**69.22**

Crack lengths on each span of bridge deck No. 22387 are as follows:

Table 21 Crack Lengths of Bridge Deck No. 22387-Span 1

Crack No.	Length (ft)	Crack No.	Length (ft)	Crack No.	Length (ft)	Crack No.	Length (ft)
C1	1.29	C12	0.97	C23	4.65	C34	4.26
C2	1.05	C13	2.27	C24	0.58	C35	2.37
C3	1.53	C14	1.41	C25	1.99	C36	1.52
C4	2.94	C15	5.58	C26	1.73	C37	1.52
C5	1.46	C16	0.79	C27	12.48	C38	11.61
C6	3.67	C17	1.90	C28	2.19	C39	0.81
C7	1.63	C18	4.02	C29	1.58	C40	2.43
C8	2.74	C19	6.00	C30	3.59	C41	8.81
C9	2.15	C20	0.58	C31	0.41	**Sum**	**112.73**
C10	1.46	C21	1.83	C32	2.55		
C11	0.49	C22	1.47	C33	0.40		

Table 22 Crack Lengths of Bridge Deck No. 22387-Span 2

Crack No.	Length (ft)	Crack No.	Length (ft)	Crack No.	Length (ft)	Crack No.	Length (ft)
C42	2.50	C57	1.77	C72	1.53	C87	0.48
C43	0.37	C58	12.93	C73	0.46	C88	1.24
C44	2.13	C59	1.37	C74	4.60	C89	0.64
C45	0.73	C60	1.92	C75	0.78	C90	0.49
C46	0.55	C61	3.96	C76	0.44	C91	0.49
C47	3.78	C62	0.63	C77	2.15	C92	0.91
C48	0.43	C63	3.10	C78	0.94	C93	0.57
C49	1.15	C64	0.76	C79	4.41	C94	0.40
C50	2.37	C65	9.28	C80	0.92	C95	0.85
C51	1.42	C66	2.59	C81	3.60	C96	0.76
C52	5.21	C67	2.60	C82	2.52	C97	1.46
C53	1.42	C68	3.71	C83	1.65	C98	0.18
C54	0.33	C69	5.88	C84	0.76	C99	0.43
C55	0.90	C70	6.02	C85	0.71	**Sum**	**121.96**
C56	0.84	C71	6.82	C86	0.15		

Table 23 Crack Lengths of Bridge Deck No. 22387-Span 3

Crack No.	Length (ft)	Crack No.	Length (ft)	Crack No.	Length (ft)	Crack No.	Length (ft)
C100	0.53	C131	2.70	C162	0.68	C193	2.36
C101	2.74	C132	4.64	C163	0.76	C194	0.43
C102	1.18	C133	0.84	C164	11.49	C195	0.50
C103	0.76	C134	0.59	C165	1.10	C196	0.52
C104	1.15	C135	0.37	C166	2.21	C197	0.20
C105	0.22	C136	1.49	C167	3.74	C198	0.32
C106	1.55	C137	0.91	C168	3.72	C199	0.58
C107	1.36	C138	1.21	C169	2.94	C200	0.86
C108	2.24	C139	1.29	C170	7.13	C201	0.12
C109	0.60	C140	0.37	C171	3.58	C202	1.38
C110	2.97	C141	0.61	C172	2.70	C203	0.54
C111	4.05	C142	0.57	C173	9.14	C204	0.30
C112	0.23	C143	1.01	C174	0.71	C205	0.21
C113	0.28	C144	1.71	C175	1.70	C206	0.36
C114	0.46	C145	1.39	C176	2.16	C207	0.56
C115	1.65	C146	0.48	C177	1.65	C208	0.17
C116	10.31	C147	0.83	C178	0.59	C209	0.09
C117	2.46	C148	1.37	C179	0.56	C210	0.09
C118	1.42	C149	2.40	C180	8.73	C211	0.35
C119	1.70	C150	1.97	C181	0.51	C212	0.34
C120	1.81	C151	0.85	C182	2.88	C213	0.15
C121	10.07	C152	6.82	C183	4.03	C214	0.14
C122	8.76	C153	0.81	C184	1.70	C215	0.10
C123	3.84	C154	1.10	C185	9.32	C216	0.13
C124	5.58	C155	3.24	C186	0.54	C217	0.15
C125	2.66	C156	0.62	C187	8.43	C218	0.17
C126	2.80	C157	1.46	C188	0.34	C219	0.08
C127	2.22	C158	0.47	C189	3.32	C220	0.87
C128	1.32	C159	0.19	C190	6.99	**Sum**	**243.86**
C129	0.50	C160	1.55	C191	2.03		
C130	0.80	C161	3.40	C192	0.92		

Table 24 Crack Lengths of Bridge Deck No. 22387-Span 4

Crack No.	Length (ft)	Crack No.	Length (ft)	Crack No.	Length (ft)	Crack No.	Length (ft)
C221	0.98	C247	0.31	C273	1.91	C299	0.49
C222	1.62	C248	0.49	C274	1.27	C300	1.70
C223	1.55	C249	0.63	C275	2.64	C301	1.15
C224	2.05	C250	0.56	C276	0.98	C302	1.20
C225	1.11	C251	0.78	C277	1.60	C303	2.82
C226	0.70	C252	1.46	C278	0.89	C304	1.52
C227	1.14	C253	0.08	C279	2.10	C305	1.80
C228	0.62	C254	0.75	C280	0.82	C306	0.71
C229	1.44	C255	0.05	C281	2.02	C307	1.40
C230	1.36	C256	0.15	C282	0.42	C308	2.06
C231	3.15	C257	0.20	C283	0.68	C309	0.99
C232	2.37	C258	0.18	C284	1.85	C310	1.46
C233	1.61	C259	1.17	C285	1.36	C311	1.30
C234	2.87	C260	3.07	C286	1.97	C312	0.86
C235	1.89	C261	0.36	C287	1.58	C313	1.38
C236	0.62	C262	0.34	C288	1.75	C314	1.57
C237	3.13	C263	2.61	C289	1.44	C315	4.48
C238	0.18	C264	1.29	C290	1.36	C316	0.38
C239	0.21	C265	1.52	C291	0.76	C317	0.58
C240	0.35	C266	1.41	C292	0.65	C318	2.30
C241	0.41	C267	1.60	C293	1.99	C319	0.62
C242	0.49	C268	0.94	C294	1.32	C320	0.64
C243	3.07	C269	0.24	C295	0.33	**Sum**	**126.10**
C244	0.59	C270	1.30	C296	0.03		
C245	0.43	C271	0.80	C297	2.48		
C246	1.83	C272	0.57	C298	1.84		

Table 25 Crack Lengths on Bridge Deck No. 22387-Span 5

Crack No.	Length (ft)	Crack No.	Length (ft)	Crack No.	Length (ft)	Crack No.	Length (ft)
C321	0.19	C333	0.54	C344	0.97	C355	0.74
C322	0.15	C334	0.70	C345	1.12	C356	2.39
C323	0.48	C335	0.54	C346	2.32	C357	0.64
C324	0.96	C336	0.94	C347	0.28	C358	0.82
C325	0.53	C337	1.60	C348	0.65	C359	2.24
C326	0.46	C338	0.60	C349	0.63	C360	0.40
C327	0.69	C339	2.81	C350	2.08	C361	1.04
C328	1.11	C340	0.11	C351	0.70	C362	1.36
C330	0.20	C341	0.37	C352	0.77	**Sum**	**37.91**
C331	0.77	C342	0.20	C353	0.70		
C332	1.09	C343	1.21	C354	1.16		

10 Appendix B - Delamination Area in Bridges

Delamination area in bridge deck No. 22383 are as follows:

Table 26 Delamination Area in Bridge Deck No. 22383

Span	Delamination No.	Area (ft^2)	Span	Delamination No.	Area (ft^2)
Span No.1	D1	5.54	Span No.2	D24	2.24
	D2	10.11		D25	0.31
	D3	11.11		D26	0.14
	D4	1.24		D27	4.45
	D5	1.92		D28	0.18
	D6	3.81		D29	0.07
	D7	5.76		D30	0.18
	D8	12.32		D31	2.76
	D9	2.14		D32	0.38
	D10	6.47		D33	0.11
	D11	0.94		D34	0.54
	D12	11.46		D35	4.63
	D13	10.86		D36	7.72
	D14	3.14		D37	3.71
	D15	16.72		D38	0.31
	D16	3.01		D39	0.34
	D17	1.35		**Sum**	**52.56**
	D18	0.77	Span No.3	D40	1.45
	D19	4.67		D41	2.61
	D20	0.93		D42	1.69
	Sum	**114.25**		D43	0.95
Span No.2	D21	21.29		D44	1.10
	D22	1.62		D45	4.30
	D23	1.59		**Sum**	**12.10**

Delamination area in bridge deck No. 22387 are as follows:

Table 27 Delamination Area in Bridge Deck No. 22387

Span	Delamination No.	Area (ft^2)	Span	Delamination No.	Area (ft^2)	Span	Delamination No.	Area (ft^2)
Span No.1	D1	35.72	Span No.3	D36	13.30	Span No.5	D72	4.17
	D2	12.38		D37	3.01		**Sum**	**478.47**
	D3	18.70		D38	30.97		D73	2.40
	D4	61.49		D39	26.90		D74	1.65
	D5	2.89		D40	77.80		D75	1.30
	D6	31.44		D41	7.68		D76	16.79
	D7	7.09		D42	60.05		D77	7.12
	D8	16.41		D43	4.93		D78	2.95
	D9	32.04		D44	5.27		D79	4.98
	D10	8.03		D45	3.87		D80	5.11
	Sum	**226.18**		D46	3.94		D81	3.89
Span No.2	D11	4.03		D47	5.69		D82	7.90
	D12	4.66		D48	47.68		D83	3.04
	D13	35.12		D49	3.51		D84	4.91
	D14	3.46		D50	4.93		D85	2.75
	D15	5.53		D51	1.47		D86	0.84
	D16	8.82		D52	4.33		D87	6.58
	D17	12.39		D53	0.81		D88	5.22
	D18	7.19		D54	13.07		D89	0.96
	D19	1.60		**Sum**	**266.07**		D90	1.21
	D20	2.77	Span No.4	D55	13.39		D91	1.13
	D21	0.80		D56	2.22		D92	3.89
	D22	1.51		D57	4.33		D93	1.29
	D23	2.15		D58	7.60		D94	1.39
	D24	18.46		D59	3.75		D95	0.46
	D25	23.62		D60	11.69		D96	1.77
	D26	11.48		D61	100.09		D97	1.72
	D27	7.60		D62	16.26		D98	2.64
	D28	57.17		D63	38.42		D99	0.38
	D29	39.55		D64	7.50		D100	4.57
	D30	76.18		D65	8.45		D101	2.72
	D31	26.56		D66	7.30		D102	0.74
	Sum	**226.18**		D67	18.23		D103	2.96
Span No.3	D32	21.10		D68	64.84		**Sum**	**105.26**
	D33	2.91		D69	42.30			
	D34	8.81		D70	21.15			
	D35	13.53		D71	7.31			

Delamination area in bridge deck No. 22451 are as follows:

Table 28 Delamination Area in Bridge Deck No. 22451

Span	Delamination No.	Area (ft^2)	Span	Delamination No.	Area (ft^2)	Span	Delamination No.	Area (ft^2)
Span No.1	D1	1.08	Span No.1	D31	6.42	Span No.3	D59	0.56
	D2	3.11		D32	12.27		D60	0.03
	D3	2.67		D33	18.19		D61	0.50
	D4	5.84		D34	1.60		D62	0.33
	D5	0.68		D35	0.58		D63	0.13
	D6	2.02		D36	1.84		D64	0.63
	D7	5.41		D37	5.32		D65	0.01
	D8	0.97		D38	0.96		D66	0.78
	D9	5.06		D39	0.06		D67	0.90
	D10	1.93		D40	0.46		D68	0.74
	D11	5.17		D41	0.32		D69	0.43
	D12	29.34		D42	2.37		D70	3.39
	D13	14.98		D43	5.48		D71	4.81
	D14	1.42		D44	0.32		D72	13.18
	D15	1.95		D45	1.29		D73	10.75
	D16	0.64		**SUM**	**204.57**		D74	3.41
	D17	26.70	Span No.2	D46	1.59		D75	0.27
	D18	7.65		D47	0.31		D76	1.22
	D19	2.51		D48	0.25		D77	1.37
	D20	1.79		D49	0.14		D78	0.05
	D21	0.80		D50	2.30		D79	1.64
	D22	1.46		D51	0.89		D80	5.12
	D23	1.61		D52	0.71		D81	0.42
	D24	2.22		D53	7.27		D82	0.35
	D25	2.81		D54	1.50		D83	2.59
	D26	0.54		**SUM**	**14.97**		D84	11.57
	D27	2.61		D55	2.95		D85	6.40
	D28	1.20		D56	2.71		D86	6.52
	D29	5.97		D57	3.02		D87	13.27
	D30	6.92		D58	2.54		**SUM**	**102.60**

11 Appendix C - GPR Results of Laboratory Tests

11.1 Specimen No. 1

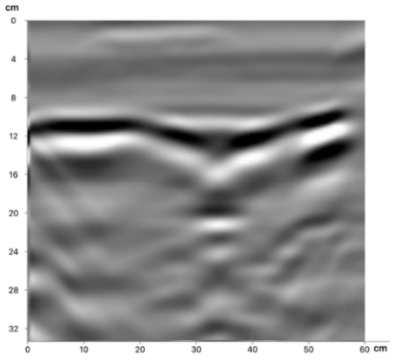

a. Line 1

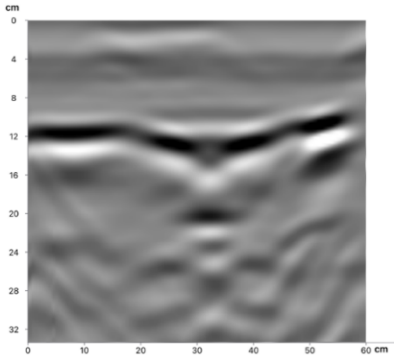

b. Line 2

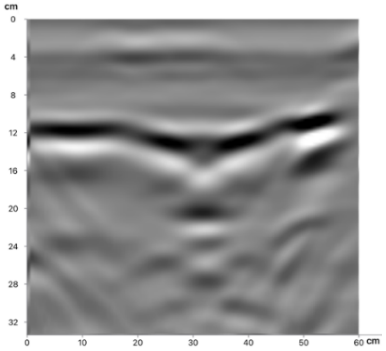

c. Line 3

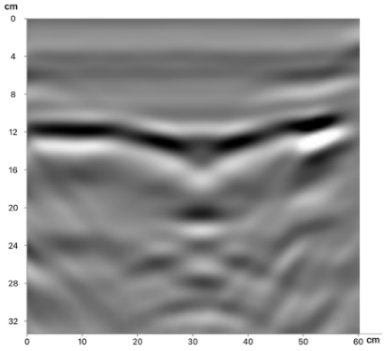

d. Line 4

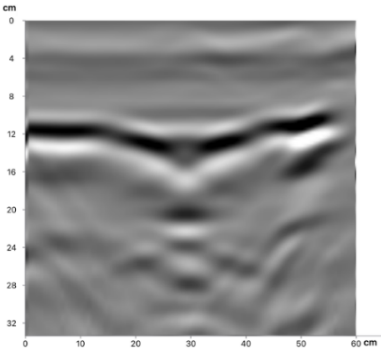

e. Line 5

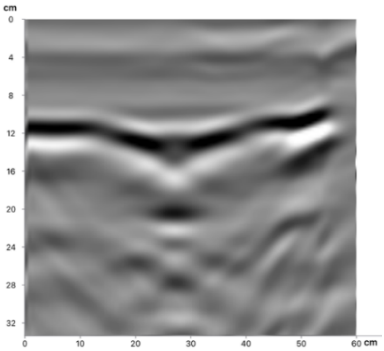

f. Line 6

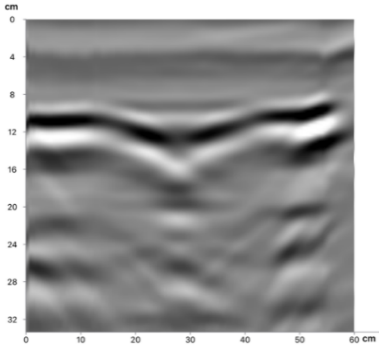

g. Line 7

Figure 140 B-Scan of Front Side Specimen No. 1 (X-Axis)

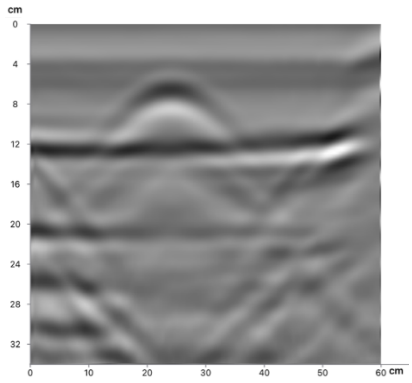

a. Line 1

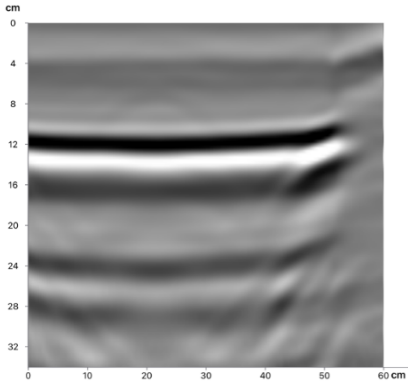

b. Line 2

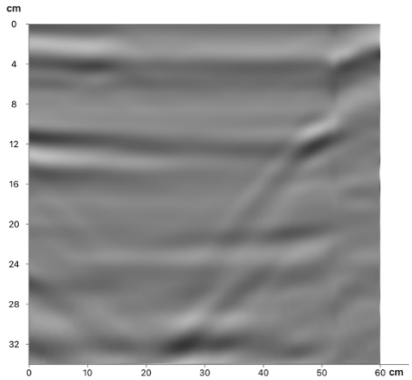

c. Line 3

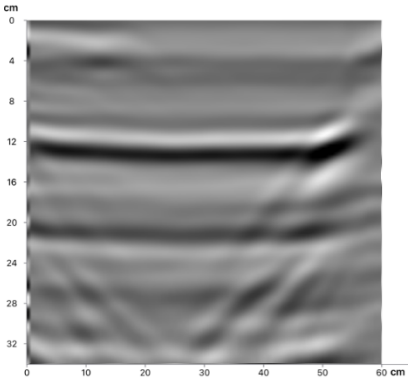

d. Line 4

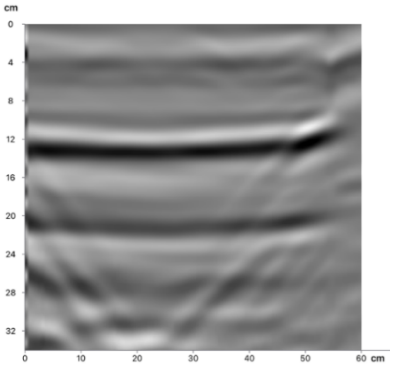

e. Line 5

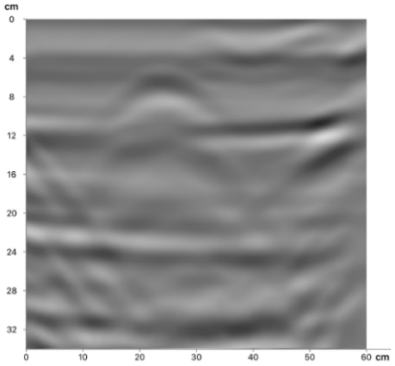

f. Line 6

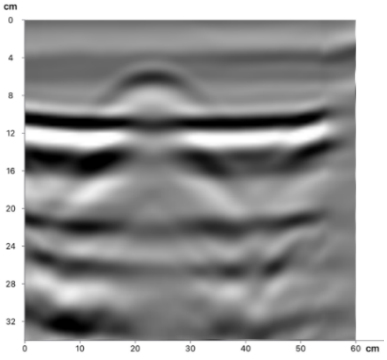

g. Line 7

Figure 141 B-Scan of Front Side Specimen No. 1 (Y-Axis)

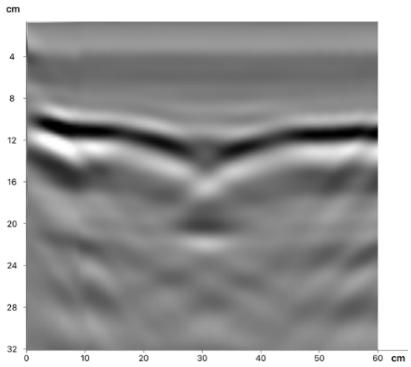

a. Line 1

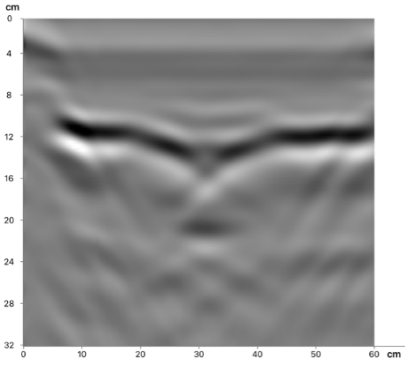

b. Line 2

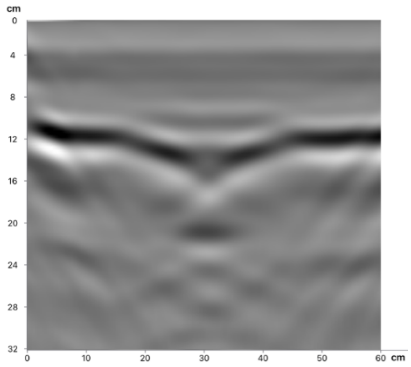

c. Line 3

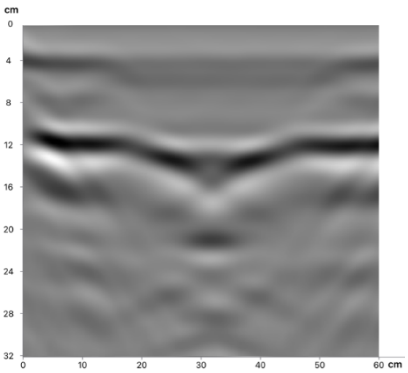

d. Line 4

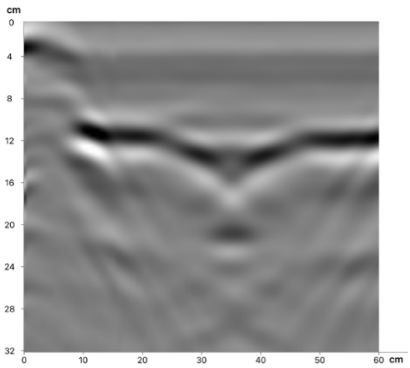

e. Line 5

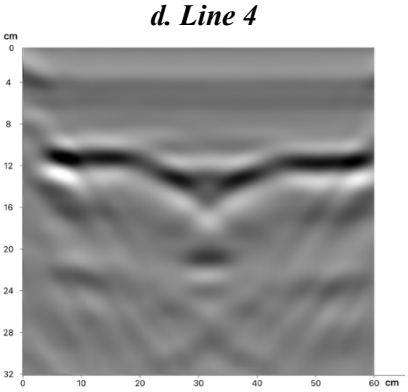

f. Line 6

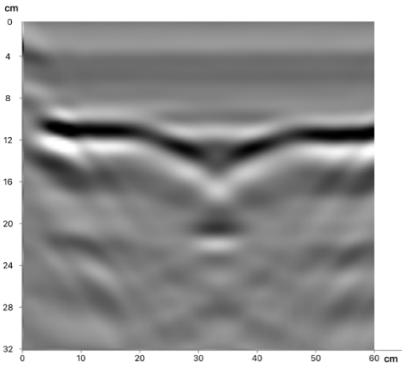

g. Line 7

Figure 142 B-Scan of Back Side Specimen No. 1 (X-Axis)

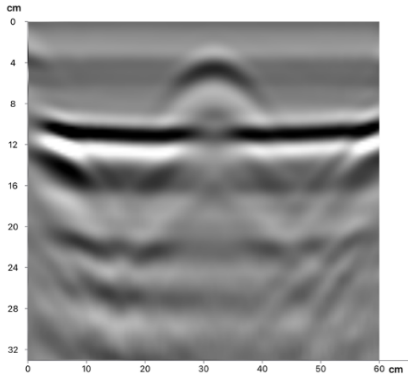

a. Line 1

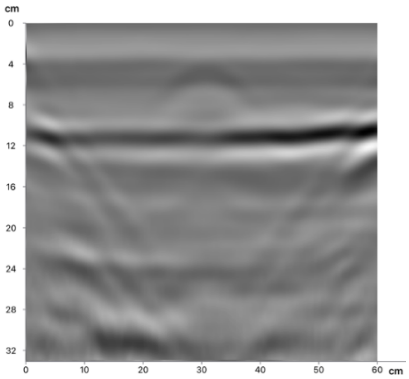

b. Line 2

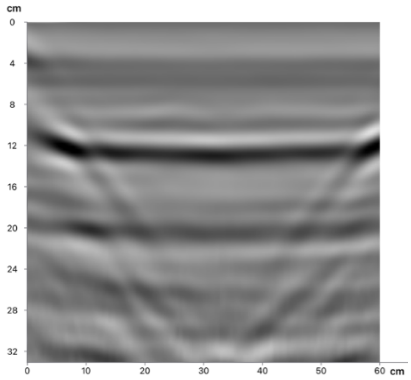

c. Line 3

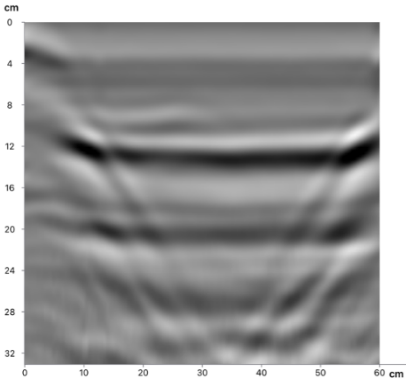

d. Line 4

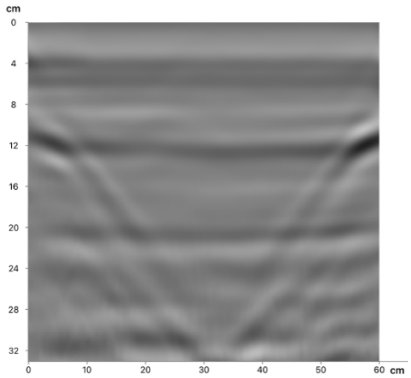

d. Line 5

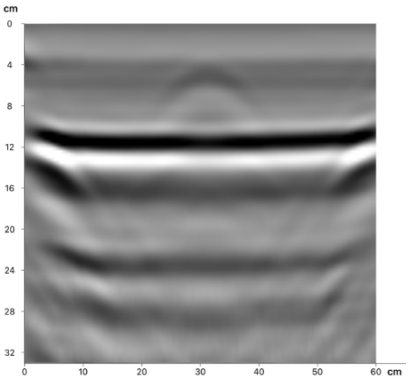

e. Line 6

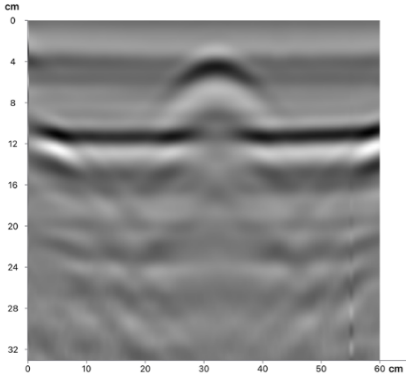

e. Line 7

Figure 143 B-Scan of Back Side Specimen No. 1 (Y-Axis)

11.2 Specimen No. 2

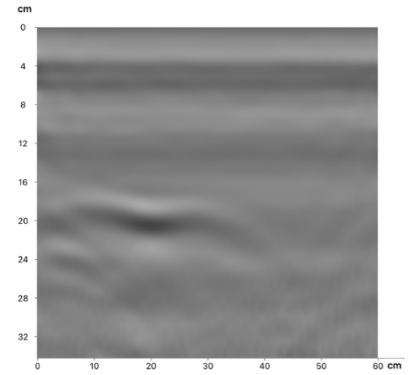

a. Line 1

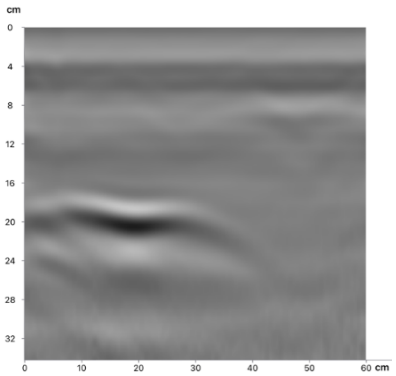

b. Line 2

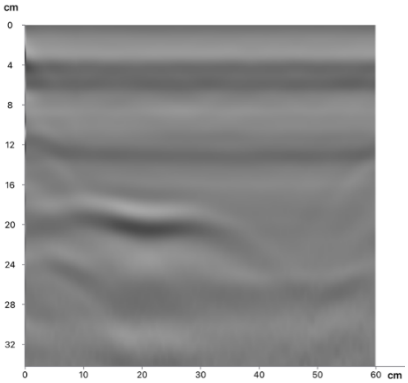

c. Line 3

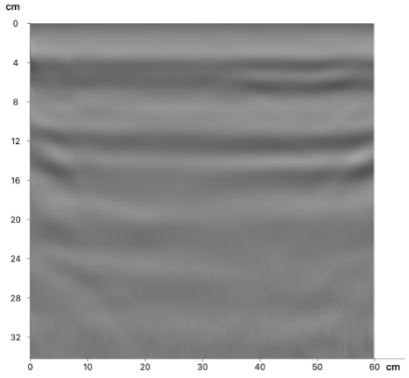

d. Line 4

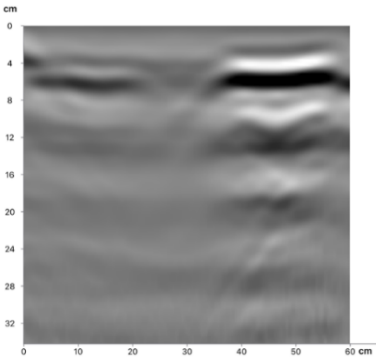

e. Line 5

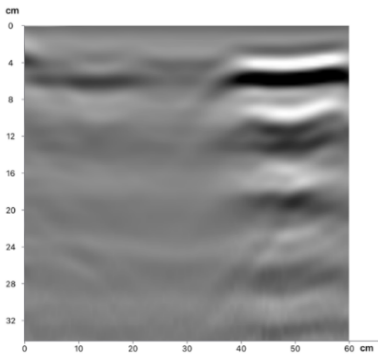

f. Line 6

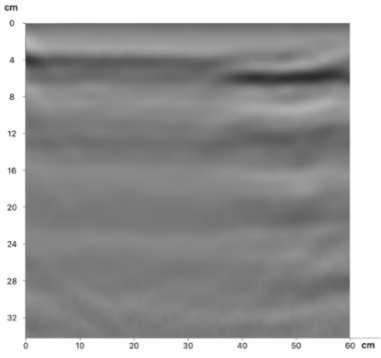

g. Line 7

Figure 144 B-Scan of Front Side Specimen No. 2 (X-Axis)

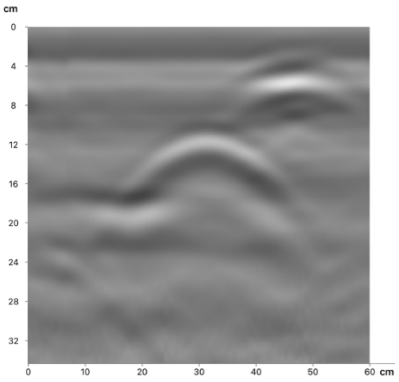

a. Line 1

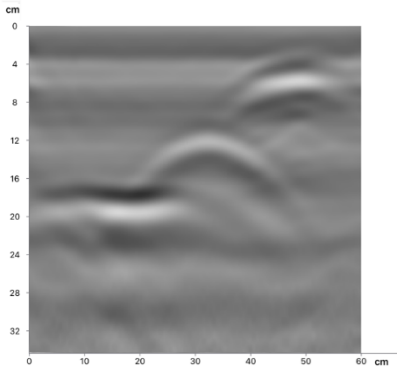

b. Line 2

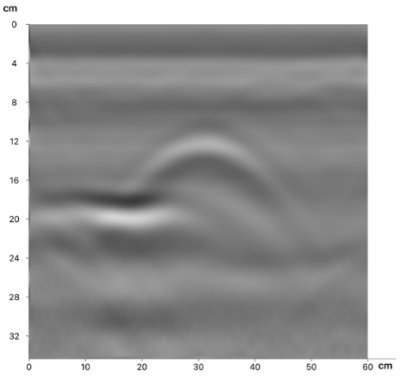

c. Line 3

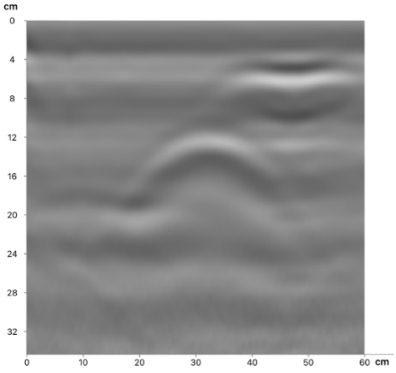

d. Line 4

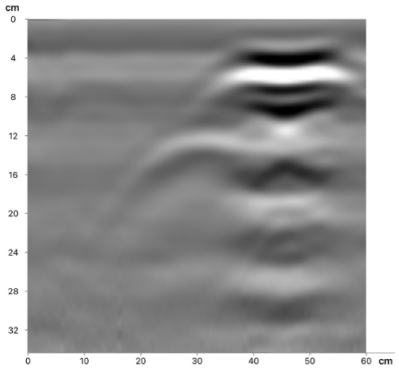

e. Line 5

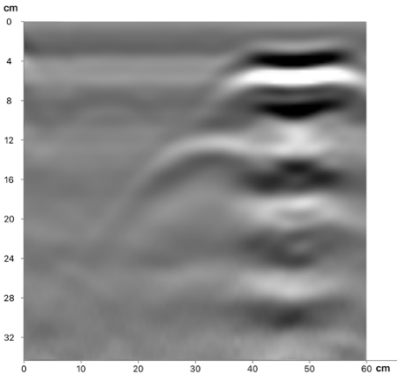

f. Line 6

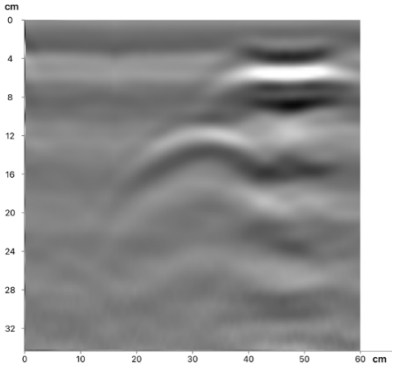

g. Line 7

Figure 145 B-Scan of Front Side Specimen No. 2 (Y-Axis)

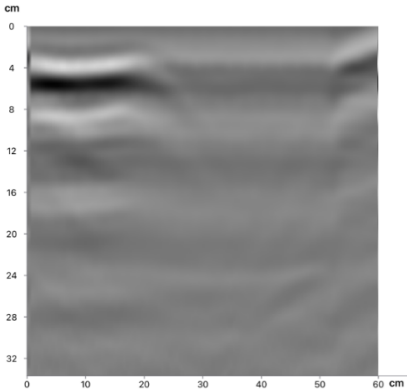

a. Line 1

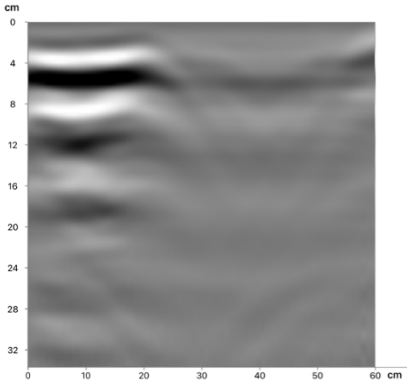

b. Line 2

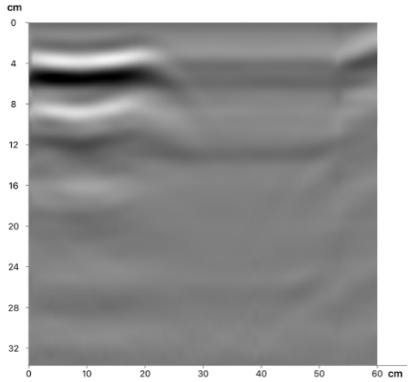

c. Line 3

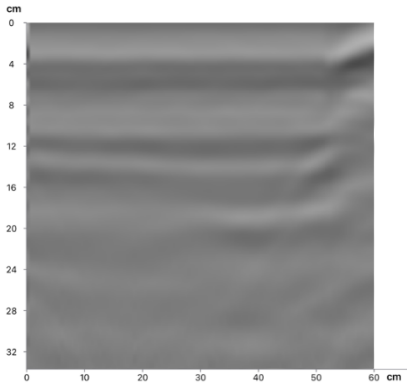

d. Line 4

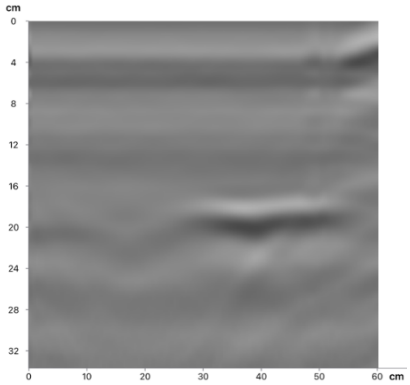

e. Line 5

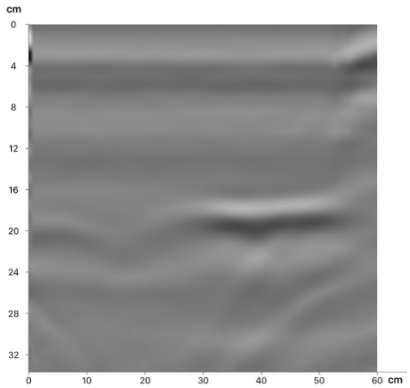

f. Line 6

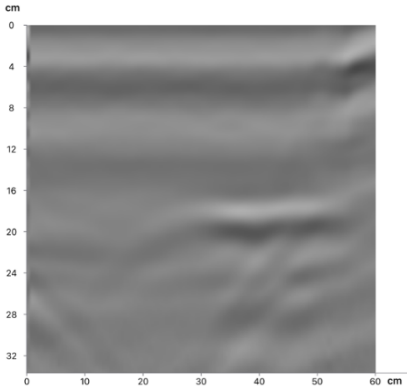

g. Line 7

Figure 146 B-Scan of Back Side Specimen No. 2 (X-Axis)

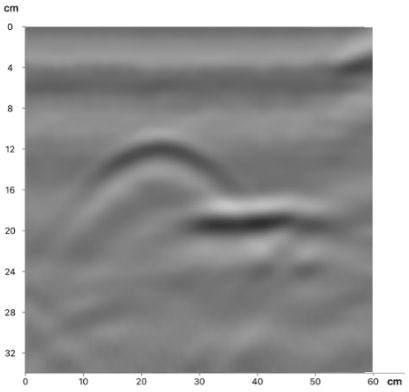

a. Line 1

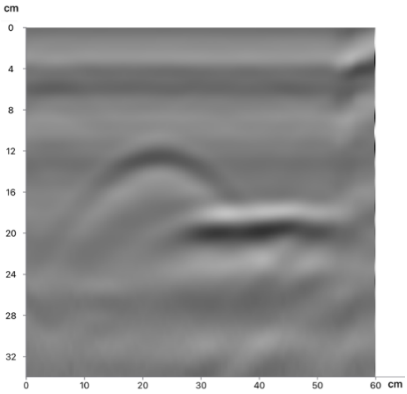

b. Line 2

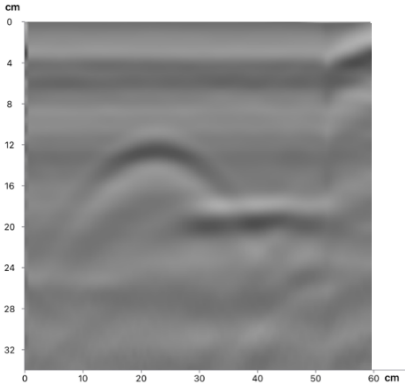

c. Line 3

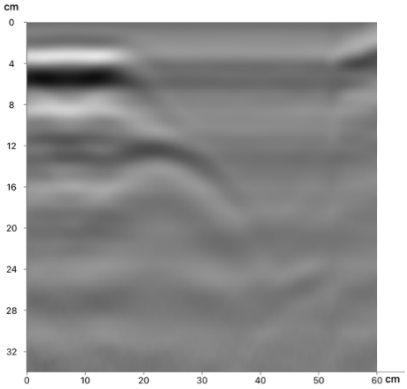

d. Line 4

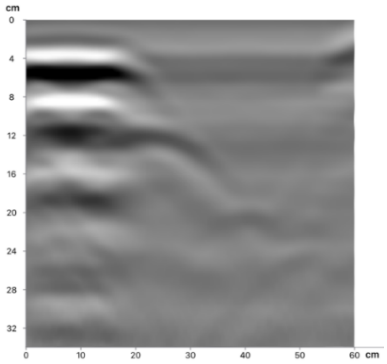

e. Line 5

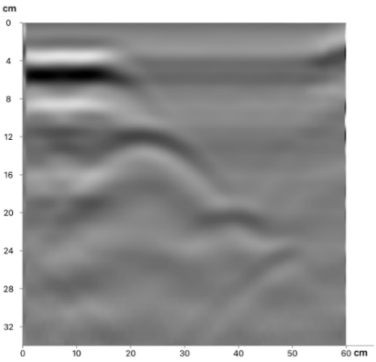

f. Line 6

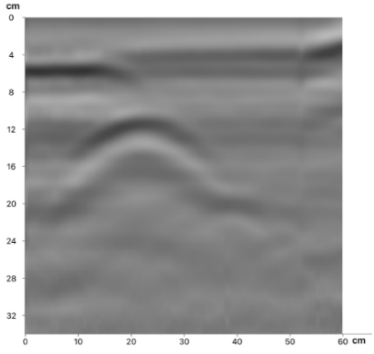

g. Line 7

Figure 147 B-Scan of Back Side Specimen No. 2 (Y-Axis)

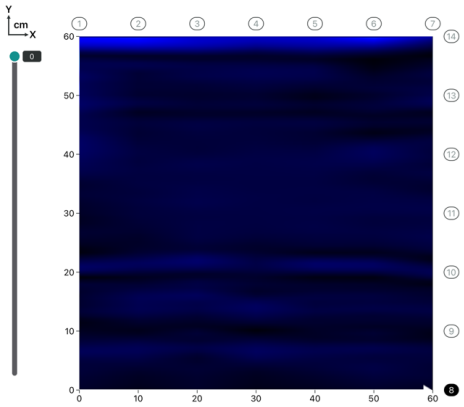

a. Depth: 0 cm

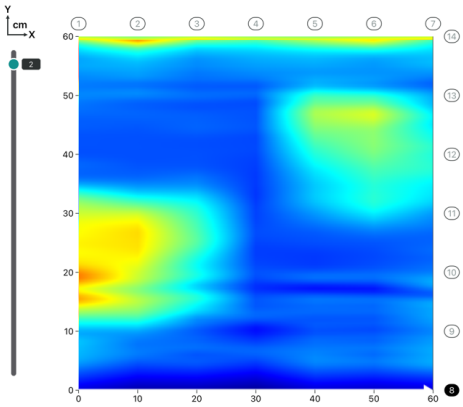

b. Depth: 2 cm

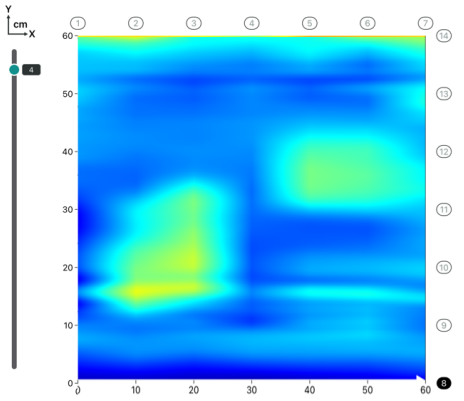

c. Depth: 4 cm

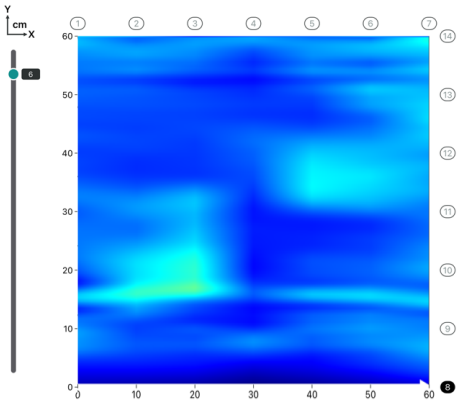

d. Depth: 6 cm

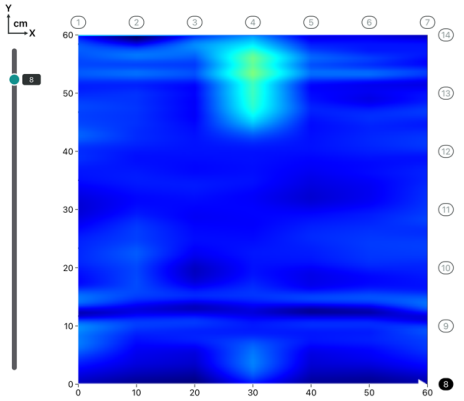

e. Depth: 8 cm

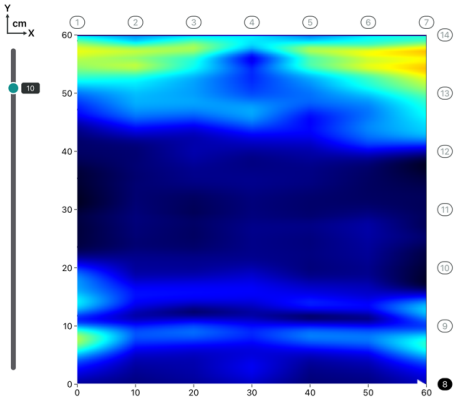

f. Depth: 10 cm

Figure 148 C-Scans of Front Side Specimen No. 1 (X-Axis)

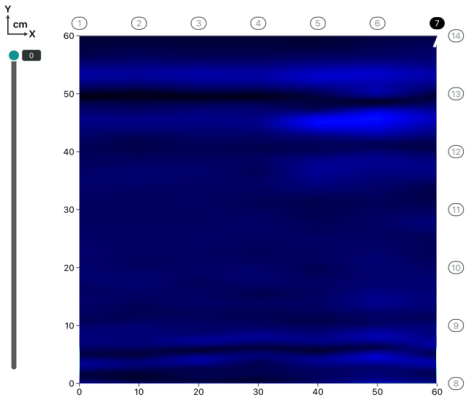

g. Depth: 0 cm

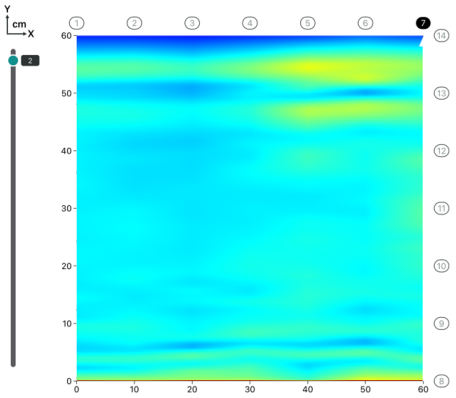

h. Depth: 2 cm

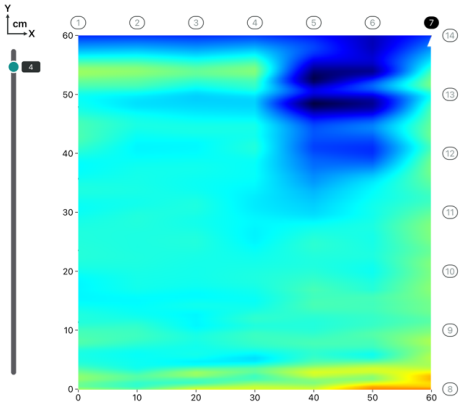

i. Depth: 4 cm

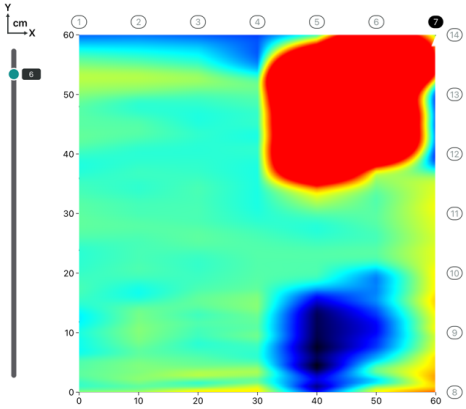

j. Depth: 6 cm

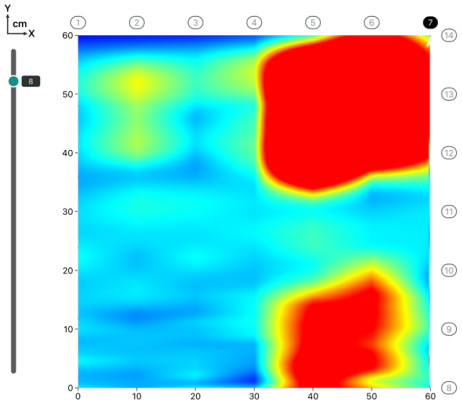

k. Depth: 8 cm

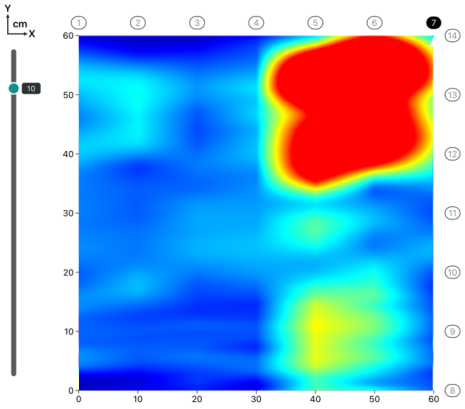

l. Depth: 10 cm

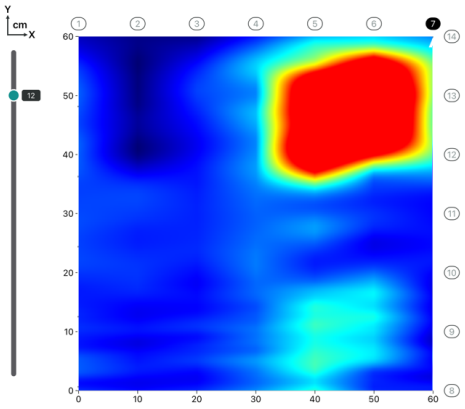

m. Depth: 12 cm

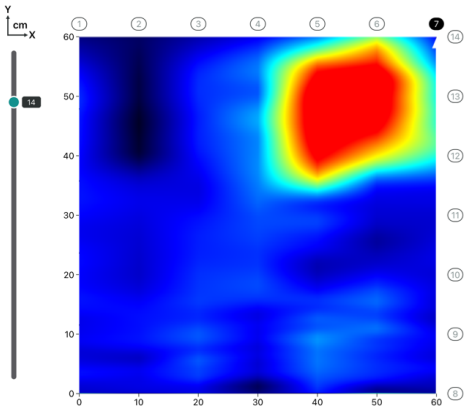

n. Depth: 14 cm

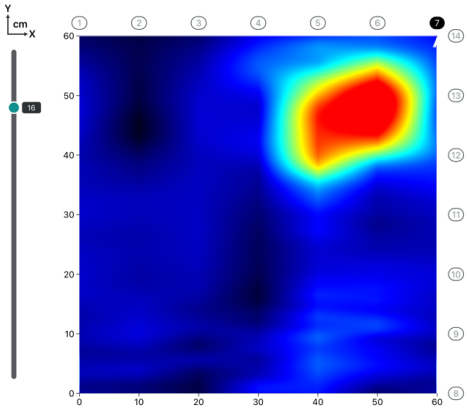

o. Depth: 16 cm

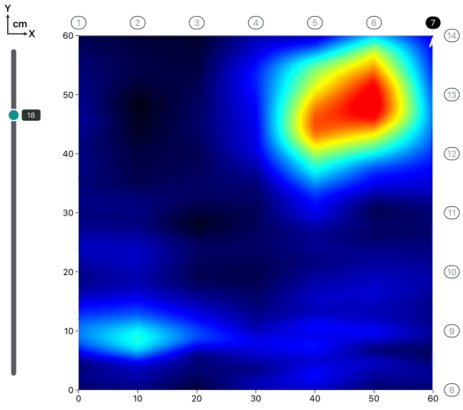

p. Depth: 18 cm

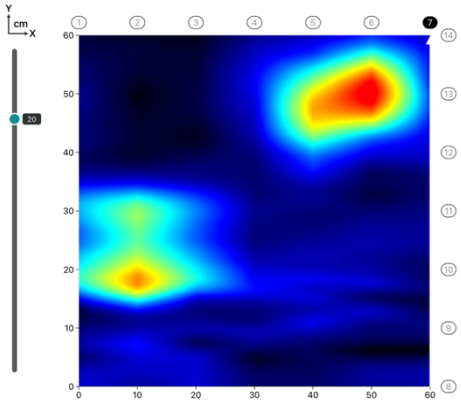

Depth: 20 cm

Figure 149 C-Scans of Front Side Specimen No. 2 (X-Axis)

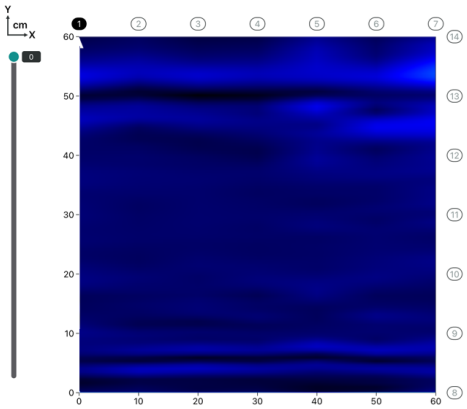

q. Depth: 0 cm

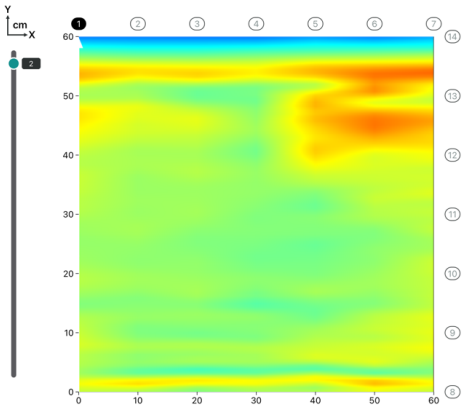

r. Depth: 2 cm

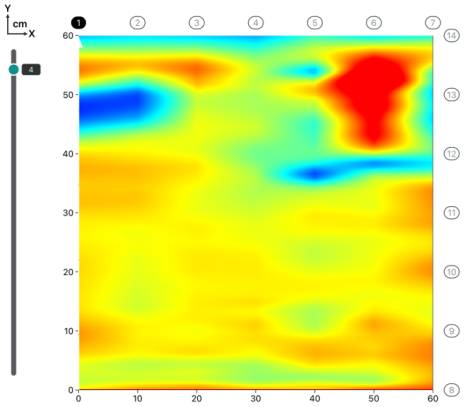

s. Depth: 4 cm

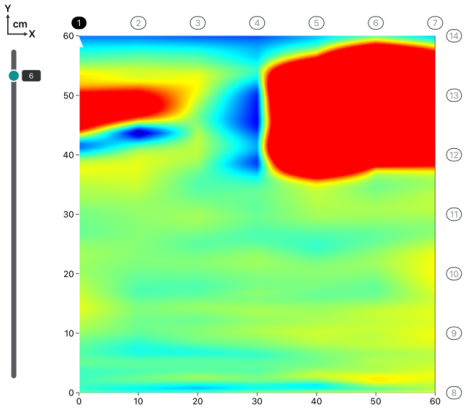

t. Depth: 6 cm

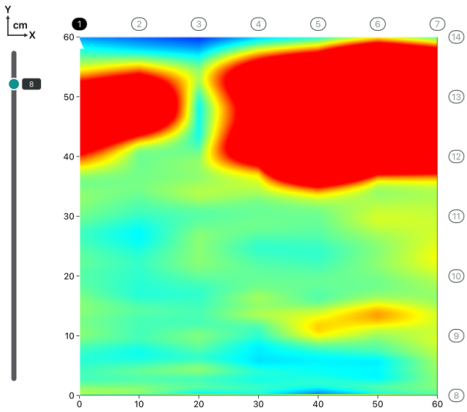

u. Depth: 8 cm

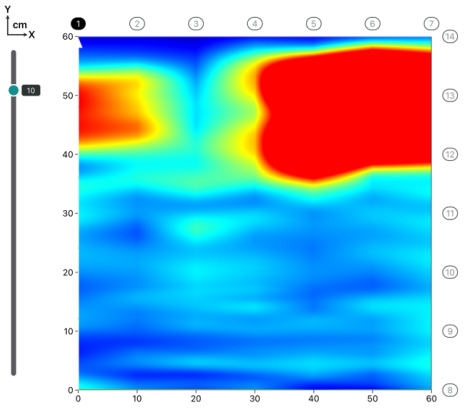

v. Depth: 10 cm

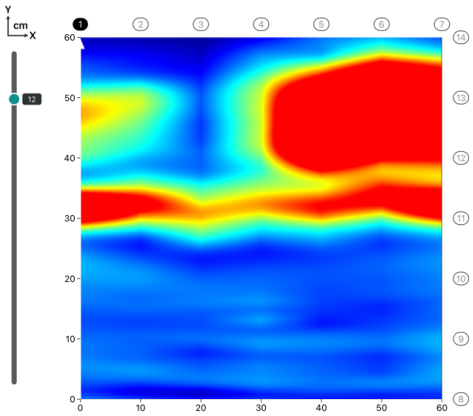

w. Depth: 12 cm

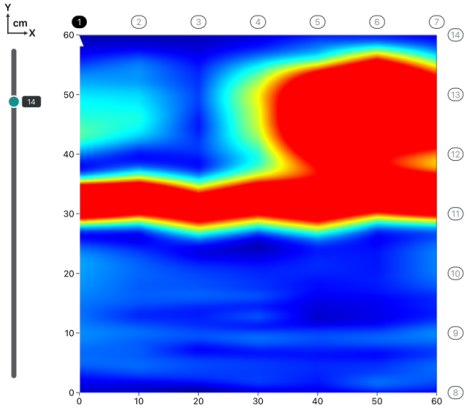

x. Depth: 14 cm

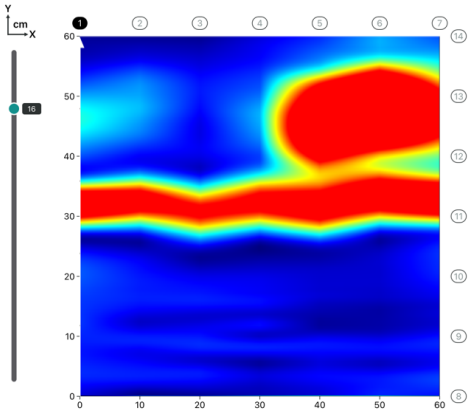

y. Depth: 16 cm

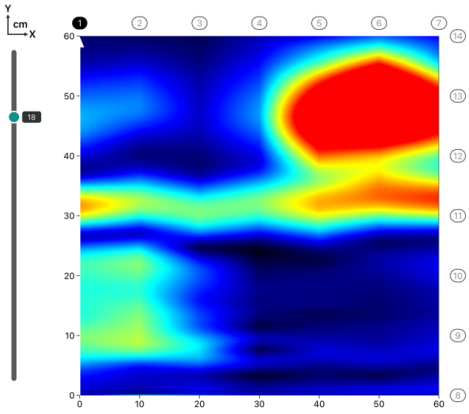

z. Depth: 18 cm

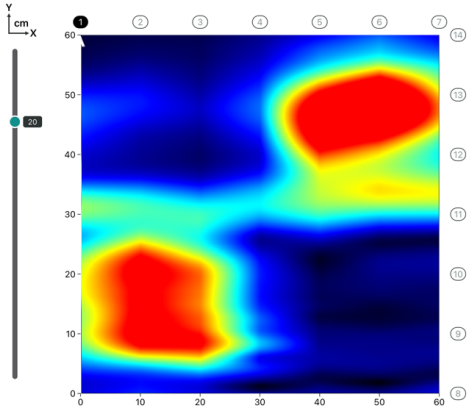

aa. Depth: 20 cm

Figure 150 C-Scans of Front Side Specimen No. 2 (Y-Axis)

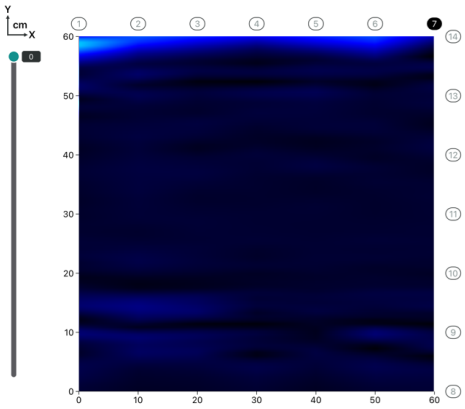

a. Depth: 0 cm

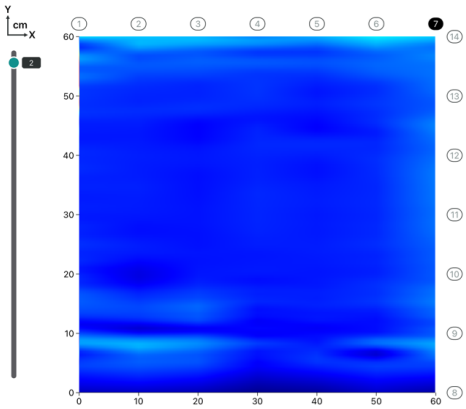

b. Depth: 2 cm

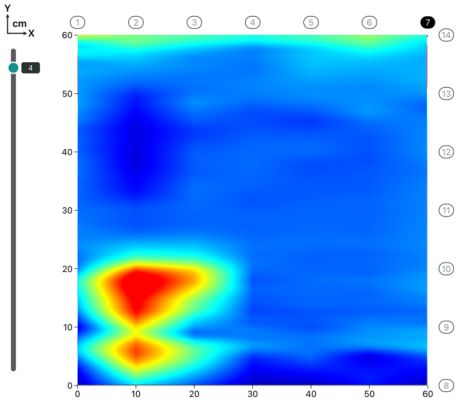

c. Depth: 4 cm

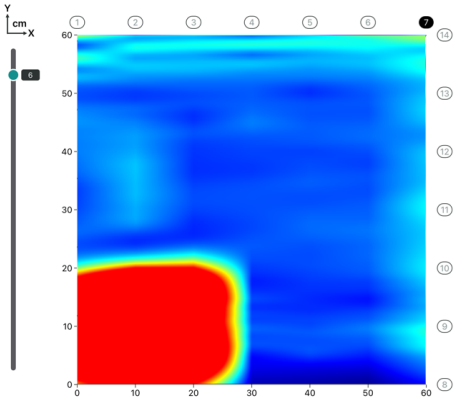

d. Depth: 6 cm

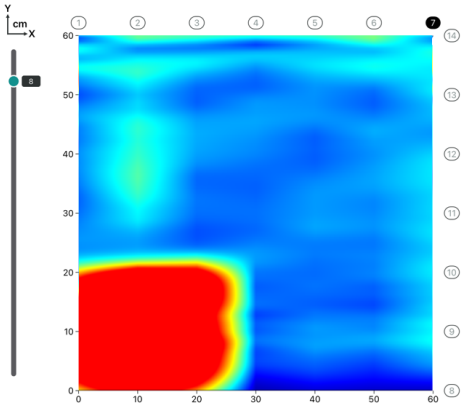

e. Depth: 8 cm

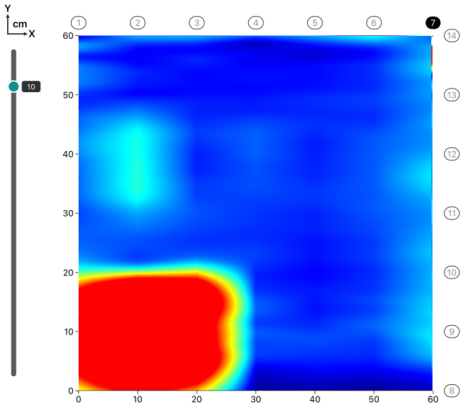

f. Depth: 10 cm

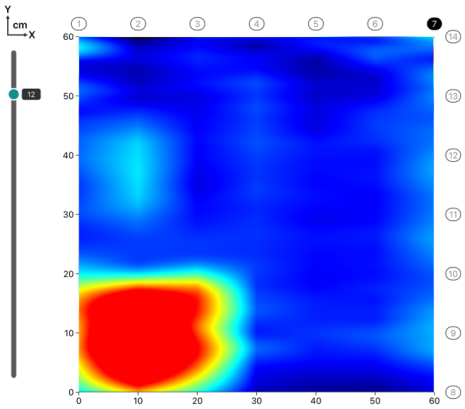

g. Depth: 12 cm

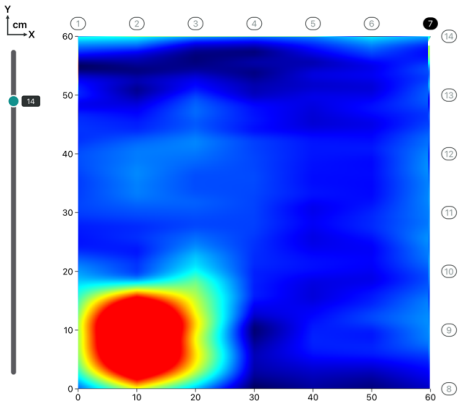

h. Depth: 14 cm

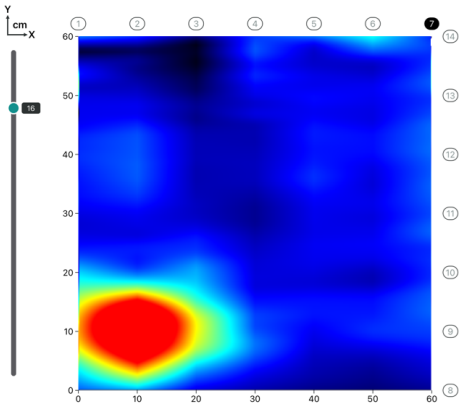

i. Depth: 16 cm

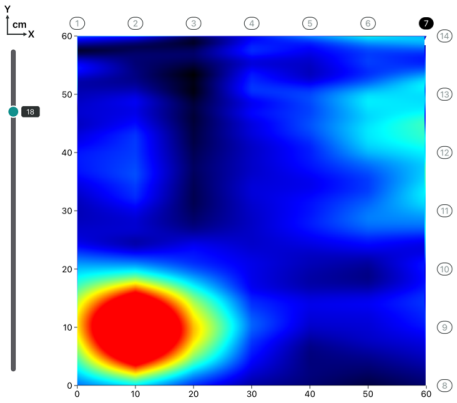

j. Depth: 18 cm

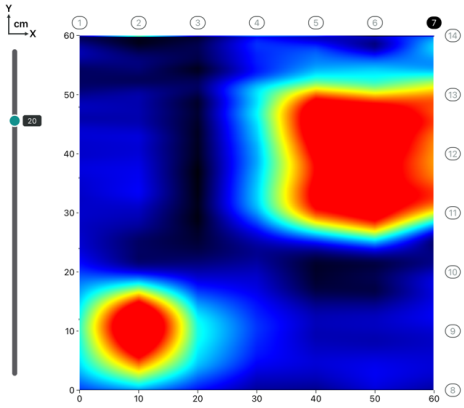

k. Depth: 22 cm

Figure 151 C-Scans of Back Side Specimen No. 2 (X-Axis)

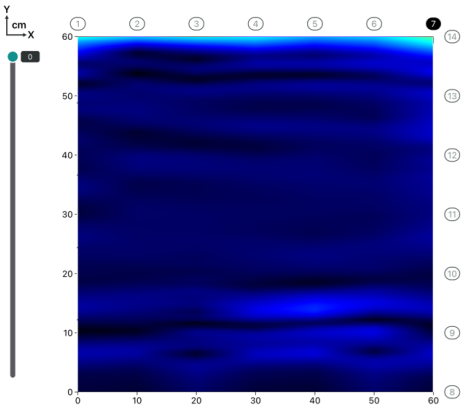

a. Depth: 0 cm

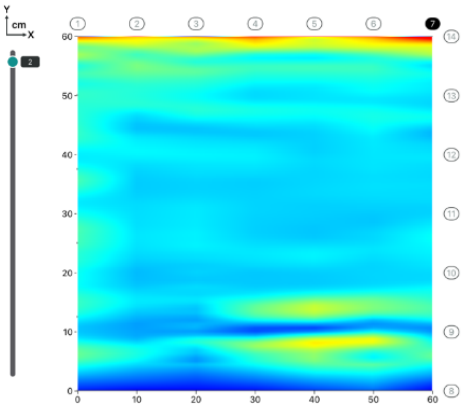

b. Depth: 2 cm

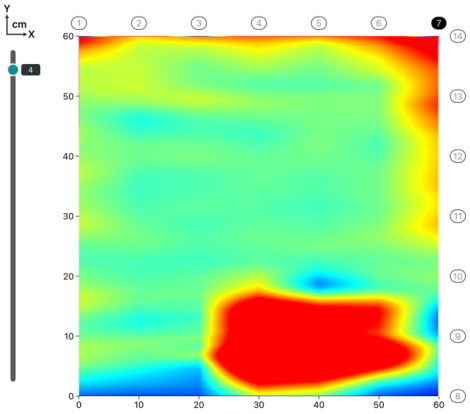

c. Depth: 4 cm

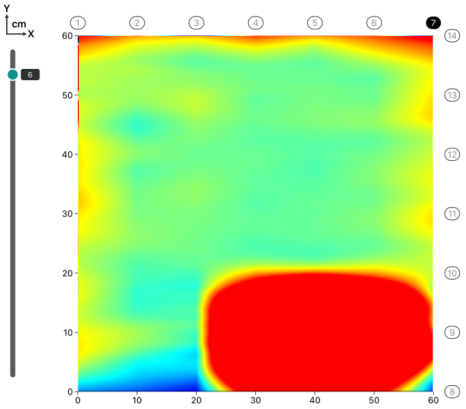

d. Depth: 6 cm

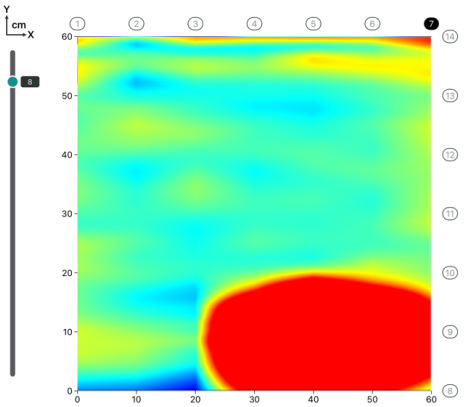

e. Depth: 8 cm

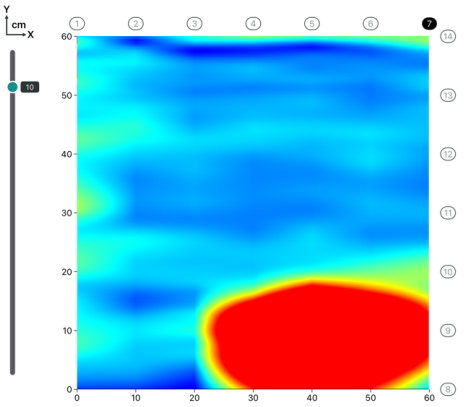

f. Depth: 10 cm

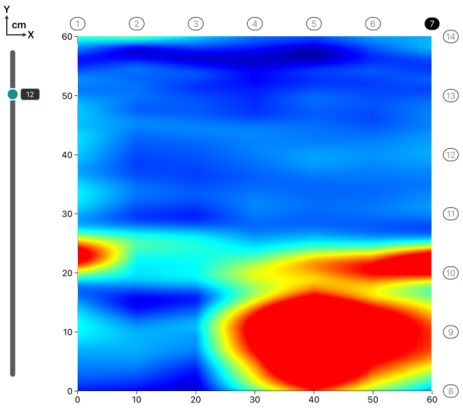

Depth: 12 cm

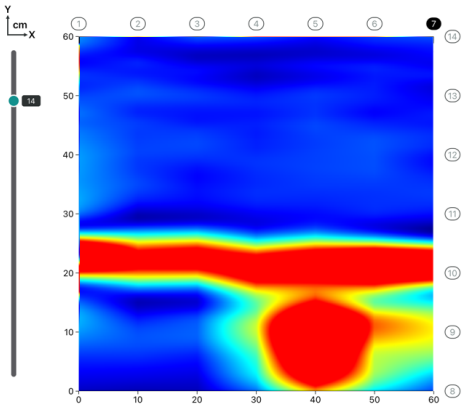

Depth: 14 cm

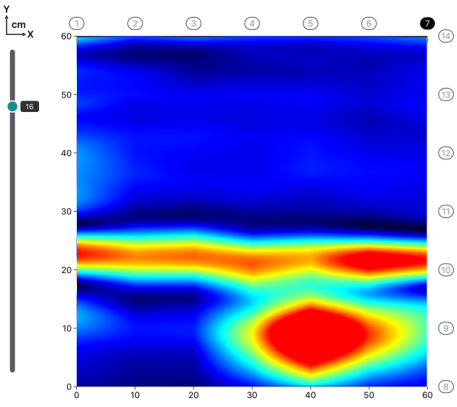

Depth: 16 cm

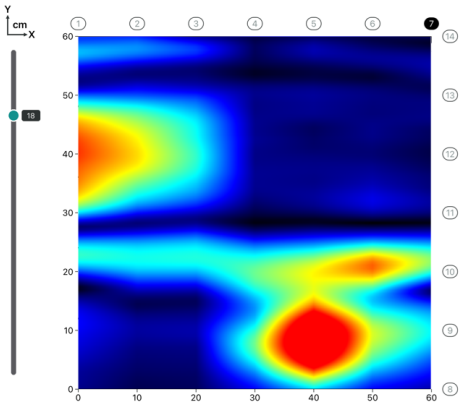

Depth: 18 cm

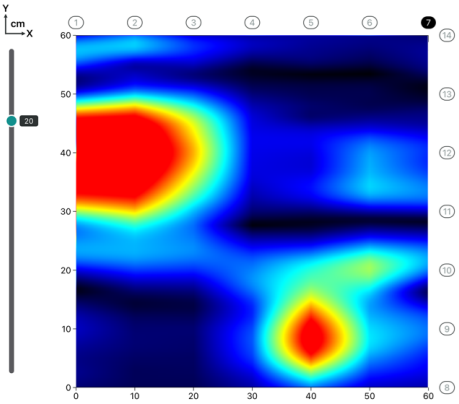

Depth: 20 cm

Figure 152 C-Scans of Back Side Specimen No. 2 (Y-Axis)

12 References

[1] "Nondestructive Testing to Identify Concrete Bridge Deck Deterioration," SHRP 2 Report S2-R06A-RR-1, TRANSPORTATION RESEARCH BOARD, ISBN: 978-0-309-12933-6, WASHINGTON, D.C., 2013.

[2] A. Omar and O. Moselhi, "Condition Monitoring of Reinforced Concrete Bridge Decks, Current Practices and Future Perspective," *Current Trends in Civil & Structural Engineering, ISSN: 2643-6876,* no. DOI: 10.33552/CTCSE.2022.08.000695, 2022.

[3] H. Wibowo and S. Sritharan, "Use of Ultra-High-Performance Concrete for Bridge Deck Overlays, IHRB Project TR-683, HPC research program," IOWA STATE UNIVERCITY, Institute for Transportation, https://www.researchgate.net/publication/323883743, 2018.

[4] W. Valencia-Saavedra, A. Aguirre-Guerrero and R. Mejía de Gutiérrez, "Assessment of the corrosion of steel embedded in an Alkali-Activated hybrid concrete exposed to chlorides," *molecules,* vol. 27(16), pp. 5296, https://doi.org/10.3390/molecules27165296, 2022.

[5] P. Schießl and C. Dauberschmidt, "Corrosion monitoring in concrete," in *Techniques for Corrosion Monitoring*, Woodhead Publishing Limited, ISBN 978-1-84569-187-5, https://doi.org/10.1533/9781845694050.3.388, 2008, pp. 388-424.

[6] N. Gucunski, S. Nazarian, H. Wiggenhauser and D. Kutrubes, "SHRP 2 R06-A, Nondestructive Testing to Identify Concrete Bridge Deck Deterioration," in *International SHRP 2–FEHRL Workshop*, Brussels, Belgium, 2010.

[7] B. A. Mazzeo, T. T. Truscott and W. S. Guthrie, "Signal processing of acoustic impact response for reinforced concrete testing using paintballs and airsoft pellets for excitation," *Newsletter of Signal Processing Society, Institute of Electrical and Electronics Engineers,* 2014.

[8] G. A. Washer, "Reliability of Bridge Inspection Technologies," in *Webinar of INSPIRE University Transportation Center*, 2022.

[9] B. Fernandes, H. Carré, J. C. Mindeguia, C. Perlot and C. La Borderie, "Spalling behaviour of concrete made with recycled concrete aggregates," *ELSEVIER,* vol. 344, no. https://doi.org/10.1016/j.conbuildmat.2022.128124, 2022.

[10] "https://www.dalinghausconstruction.com/".

[11] T. Omar, M. L. Nehdi and T. Zayed, "Integrated Condition Rating Model for Reinforced Concrete Bridge Decks," *Journal of Performance of Constructed Facilities,* no. DOI: 10.1061/(ASCE)CF.1943-5509.0001084, 2017.

[12] N. Lawrence Kyle , Subsidence Cracking of Concrete Over Steel Reinforcement Bar in Bridge Decks, Master Thesis, Blacksburg, Virginia: Virginia Polytechnic Institute and State Universit, 2001.

[13] J. Wiss, "Investigation of Bridge Decks," MONTANA DEPARTMENT OF TRANSPORTATION, Northbrook, Illinois, 2017.

[14] S. Gholizadeh, "A review of non-destructive testing methods of composite materials," 2016.

[15] T. Mahan, M. Stover, A. Arguelles and J. Menold, "CREATING A DESIGN FOR INSPECTABILITY FRAMEWORK: INVESTIGATING DFAMHEURISTICS FOR

INSPECTION TECHNOLOGIES," in *International Design Engineering Technical Conferences and Computers and Information in Engineering Conference*, 2020.

[16] C. Maierhofer, "Nondestructive Evaluation of Concrete Infrastructure with Ground Penetrating Radar," *Journal of Materials in Civil Engineering,* Vols. 15, https://doi.org/10.1061/(asce)0899-1561(2003)15:3(287)., p. 287–297, 2003.

[17] "Structure Inspection Manual, Part 5, NDT and PDE Testing," Wisconsin Department of Transportation, 2017.

[18] Z. Sbartaï, S. Laurens, S. Elachachi and C. Payan, "Concrete properties evaluation by statistical fusion of NDT techniques," *Construction and Building Materials,* vol. 37, no. https://doi.org/10.1016/j.conbuildmat.2012.09.064., p. 943–950, 2012.

[19] K. Amini, M. Jalalpour and N. Delatte, "Advancing concrete strength prediction using non-destructive testing Development and verification of a generalizable model," *Construction and Building Materials,* vol. 102, no. https://doi.org/10.1016/j.conbuildmat, p. 762–768, 2016.

[20] P. Sepehr , J. Zhu, C. Sim, K. Won, B. A. Mazzeo and . W. S. Guthri, "Multi-sensor data collection and fusion using autoencoders in condition evaluation of concrete bridge decks," *Infrastructure Preservation and Resilience,* vol. 2, no. https://doi.org/10.1186/s43065-021-00032-3, p. No. 18, 2021.

[21] K. Dinh, T. Zayed, M. Zayed, F. ASCE, . F. Romero and . A. Tarussov, "Method for Analyzing Time-Series GPR Data of Concrete Bridge Decks," *Bridge Engineering,* no. http://dx.doi.org/10.1061/(ASCE)BE.1943-5592.0000679, 2015.

[22] A. Tarussov, M. Vandry and A. De La Haza, "Condition assessment of concrete structures using a new analysis method: ground-penetrating radar computer-assisted visual interpretation," vol. 38, no. http://dx.doi.org/10.1016/j.conbui, p. 1246–1254, 2013.

[23] A. Zaki, H. Chai, D. Aggelis, and N. Alver, "Non-destructive evaluation for corrosion monitoring in concrete: A review and capability of acoustic emission technique," vol. 15, no. https://doi.org/10.3390/s150819069., p. 19069–19101, 2015.

[24] S. Kashif Ur Rehman, Z. Ibrahim, S. Ali Memon and M. Jameel, "Nondestructive test methods for concrete bridges: A review," *Construction and Building Materials,* vol. 107, no. https://doi.org/10.1016/j.conbuildmat.2015.12.011, pp. 58-86, 2016.

[25] L. Zanzi and D. Arosio, "Sensitivity and accuracy in rebar diameter measurements from dual-polarized GPR data," *Construction and Building Materials,* vol. 48, no. https://doi.org/10.1016/j.conbuildmat.2013.05.009, pp. 1293-1301, 2013.

[26] KONTUR, "Three Antena Arrays Sensor," https://www.kontur.tech/sensors, (Last accessed June, 2024).

[27] G. Washer, R. Fenwick, N. Bolleni and J. Harper, "Effects of environmental variables on infrared imaging of subsurface features of concrete bridges," *BRIDGE ENGINEERING,* vol. 2108, no. https://doi.org/10.3141/2108-12, pp. 107-114, 2009.

[28] "Bridge Deck Scanning Findings Report (Vol. 1 of 4), BRKEY 22387," NECXO West USA, Inc., 2023.

[29] C. Cheng, Z. Shang and Z. Shen, "Bridge deck delamination segmentation based on aerial thermography through regularized grayscale morphological reconstruction and gradient statistics," *Infrared Physics & Technology,* vol. 98, no. ISSN 1350-4495, pp. 240-249, 2019, https://doi.org/10.1016/j.infrared.2019.03.018.

[30] "ASTM C876-15, Standard Test Method for Corrosion Potentials of Uncoated Reinforcing Steel in Concrete," ASTM, 2022.

[31] https://www.pcte.com.au/.

[32] T. W. Robison and J. E. Tanner, "BRIDGE DECK EVALUATION USING NONDESTRUCTIVE TEST METHODS, FHWA-WY-10/07F," Department of Civil and Architectural Engineering, University of Wyoming , 2012.

[33] "Standard Practice for Measuring Delaminations in Concrete Bridge Decks by Sounding, ASTM D 4580-3," ASTM, 2018.

[34] A. P. Arguelles, "Influence of microstructural morphology on ultrasonic scattering in polycrystalline media- A Dessertion For the Degree of Doctor of Philosophy," The University of Nebraska-Lincoln, 2016.

[35] C. M. Kubea, A. P. Arguelles and J. A. Turner, "Ultrasonic backscatter from elongated grains using line focused ultrasound," *Ultrasonics,* vol. 82, no. https://doi.org/10.1016/j.ultras.2017.07.013, pp. 79-83, 2018.

[36] C. M. Kube, A. P. Arguelles and J. A. Turner, "On the acoustoelasticity of polycrystalline materials," *The Journal of the Acoustical Society of America,* vol. 138, no. https://doi.org/10.1121/1.4928720, 2015.

[37] T. Mahan, L. Katch, A. P. Argüelles and J. Menold, "Design for Inspectability: A Framework to Increase Inspectability of Additive Manufacturing Parts for Pulse-Echo Ultrasonic Inspection Methods," *Journal of Mechanical Design,* vol. 144, no. https://doi.org/10.1115/1.4053812, 2022.

[38] N. Huang, O. J. Cook, J. D. Warner, R. L. Smithson, C. M. Kube, A. P. Argüelles and A. M. Beese, "Effects of infiltration conditions on binder jet additively manufactured stainless steel infiltrated with bronze," *Additive Manufacturing,* Vols. Volume 59, Part A, no. https://doi.org/10.1016/j.addma.2022.103162, 2022.

[39] FHWA, "Bridge - Impact Echo (IE)," https://infotechnology.fhwa.dot.gov/impact-echo-ie/, (Last accessed June, 2024).

[40] "Advanced Condition Assessment of Bridge Decks, Prepared Proposal for Penn State University & Pennsylvania Department of Transportation," Infratek Solutions Inc., Princeton Junction, NJ 08550, 2022.

[41] 3D-RADAR, "DXG Antenna Array Series," http://3d-radar.com/wp-content/uploads/2018/05/DXG-Antenna-Array-Series.pdf, (Last accessed June, 2024).

[42] 3D-RADAR, "3D-RADAR EXAMINER SOFTWARE, Product Brochure," http://3d-radar.com/system/, (Last accessed June, 2024).

[43] www.flir.com/research, "Application Note, Mobile Infrared Scanning –A High-Tech, Accurate Alternative To Traditional Bridge Inspection Methods," https://www.w-nexco-usa.com/assets/documents/Nexco-West%20App%20Bridge%20Deck%20Assessment.pdf, (Last accessed June, 2024).

[44] NEXCO_West, "Desk Top Scaning System (DTSS)," https://www.w-nexco-usa.com/assets/documents/DTSS.pdf, (Last accessed June, 2024).

[45] V. H. Mac, Q. H. Tran, J. Huh, N. S. Doan, C. Kang and D. Han, "Detection of Delamination with Various Width-to-depth Ratios in Concrete Bridge Deck Using Passive IRT: Limits and Applicability," *Materials (Basel),* vol. 12(23): 3996, no. doi: 10.3390/ma12233996, 2019 Dec

2.

[46] S. Hiasa, R. Birgul, F. N. Catbasa and M. Matsumoto, "Experimental and numerical studies for suitable infrared thermography implementation on concrete bridge decks," *Measurement,* vol. 121, pp. 144-159, 2018.

[47] P. Cotiˇc, D. Kolariˇc, V. Bosiljkov and Bosiljk, "Determination of the applicability and limits of void and delamination detection in concrete structures using infrared thermography," *NDT E Int.,* vol. 74, p. 87–93, 2015.

[48] https://data.goerie.com/bridge/pennsylvania/lawrence/42073/.

[49] E. H. a. G. Hans, "RGPR — An open-source package to process and visualize GPR data," in *17th International Conference on Ground Penetrating Radar (GPR), doi: 10.1109/ICGPR.2018.8441658*, Switzerland, 18-21 June 2018.

[50] T. Q. H. J. D. N. K. C. H. D. Mac VH, "Detection of Delamination with Various Width-to-depth Ratios in Concrete Bridge Deck Using Passive IRT: Limits and Applicability," *Materials (Basel),* p. 12(23):3996. doi: 10.3390/ma12233996. PMID: 31810200; PMCID: PMC6926699., 2019.

[51] S. McGuigan, A. P. Arguelles, A.-F. Obaton, A. M. Donmez, J. Riviere and P. Shokouhi, "Resonant ultrasound spectroscopy for quality control of geometrically complex additively manufactured components," *Additive Manufacturing,* vol. 39, no. https://doi.org/10.1016/j.addma.2020.101808, 2021.

[52] "NFRARED THERMOGRAPHY (IRT) INSPECTION OF BRIDGE DECKS," http://penetradar.com, 2017.

Acknowledgments

The Penn State team would like to acknowledge the valuable guidance and thought-provoking comments from the study panel members, Shane Szalankiewicz and Keith Cornelius. Special thanks go to Hoda Azari, the NDE research program manager, and Blake Cox of the Turner-Fairbank Highway Research Center of FHWA for providing a laboratory test facility. The research team is also grateful to Heather Sorce for her comprehensive support and administrative assistance.